CASE STUDIES IN INTERFACIAL STABILITY AND SOLIDIFICATION

A Dissertation

Presented to the Faculty of the Graduate School

of Cornell University

in Partial Fulfillment of the Requirements for the Degree of

Doctor of Philosophy

by

Anthony L. Altieri

May 2014

CASE STUDIES IN INTERFACIAL STABILITY AND SOLIDIFICATION

Anthony L. Altieri, Ph.D.

Cornell University 2014

The stability of liquid-gas interfaces plays a key role in a wide range of processing operations, from the high-speed rapid solidification of liquid metals to the effective application of pesticides using the dispersal of liquid drops from a spray nozzle into an agricultural setting. Two case studies of interfacial stability are presented in this dissertation.

The first study concerns the formation of thin metallic ribbons by the planar-flow melt spinning (PFMS) process. Starting from the liquid state, PFMS rapidly solidifies to an amorphous metal with unique electromagnetic and mechanical properties, enabling materials with improved energy-conversion efficiencies and materials with high strength-to-weight ratios, among others.

In PFMS, metal is quenched against a rotating chill-wheel in two sequential steps. During the primary quench, liquid metal contacts the chill-wheel, against which it loses its sensible and latent heat and thereby solidifies. During the secondary quench, solid ribbon adheres to the wheel until it is detached mechanically or detaches naturally by a thermo-elastic stress relief mechanism. These quenching processes are examined experimentally and via analytical modeling.

The heat transferred to the wheel during the primary quench causes the wheel temperature to rise in the absence of internal cooling of the wheel. The wheel

temperature affects the properties of the ribbon as well as the ribbon adhesion during the secondary quench. Wheel heat-up is measured experimentally via thermocouples embedded in the wheel. Spatial and temporal temperature variations are observed. A semi-empirical, 2-dimensional conduction model is derived from the full conduction equations to identify the limits where the reduced-order model is valid. The reduced order model is tested against data. The model shows agreement with the data, capturing observed heat-up features.

Upon solidifying, the ribbon forms adhesive bonds with the substrate and begins to wrap around the wheel. Detachment occurs when these bonds are broken, either mechanically by a scraper or naturally through thermo-elastic stress relief, a process likened to Griffith crack-propagation. A ribbon cooling model is combined with the classic Griffith-Kendall model of peel-off of an elastic solid from a substrate, to predict the ribbon sticking distance. Under some conditions, there is no ribbon detachment. This event has been called catastrophic adhesion. The ribbon detachment model explains quantitatively accounts of detachment found in the prior literature.

Ribbon thickness variations or defects sometimes occur. These periodic variations are known to be caused by vibrations of a molten metal-air interface which allows air pockets to become entrained between the wheel and the metal, impeding solidification. However, it was not known how to avoid these defects. To this end, a model of a free interface, subject to various flow conditions and kinematic constraints, is posed and solved. Using linear stability theory, numerical approximations of eigenfrequencies are compared against experimental defect frequency. The model is the basis for strategies of defect mitigation.

The second study concerns spray atomization of one- and two-phase flows from agricultural spray nozzles. It has been found previously that single phase liquids sprayed from a nozzle are subject to instabilities and break up into droplets. The introduction of a second, immiscible phase also results in sheet breakup, but through a different mechanism. These sheet breakup mechanisms are summarized and documented photographically. Droplet size from single phase sprays are compared favorably with classical theory. Then, a novel model for two-phase sheet breakup is presented, also giving favorable agreement with experimentally observed droplet size.

BIOGRAPHICAL SKETCH

The author attended the University of Connecticut, where he majored in Chemical Engineering. He performed undergraduate research on diffusion in direct-alcohol fuel cells. He graduated in the Spring of 2007 with honors. In the Fall of 2007, he arrived at Cornell University, where he joined the spin-casting project under Paul Steen. In the Summer of 2012, he worked as an intern at Dow AgroSciences studying atomization of agricultural nozzle sprays.

This work is dedicated to my father.

ACKNOWLEDGEMENTS

I would like to thank my advisor, Paul Steen, whose guidance made this thesis possible. I would also like to thank my faculty members Abraham Stroock and Tim Healey for serving on my committee and providing suggestions and critique of my research. I am grateful to field committee memeber Eric Theisen for his willingness to discuss my research and provide his casting expertise. I thank friend and mentor Brenton Cox, whose advice eased my transition into graduate research. His insight helped shape most of the work presented in this thesis. Undergraduate aid in collecting data was invaluable. In particular, I'd like to thank Brian Carroll, Christopher Jakobson, Michael Alexander, Jack Pollack and Zach Cesaro for their enthusiasm and hard work which made managing the casting lab enjoyable.

TABLE OF CONTENTS

LIST OF TABLES

LIST OF FIGURES

CHAPTER 1

INTRODUCTION

1.1 Overview

Planar-flow melt spinning (PFMS) is a process for forming thin metallic sheets or ribbons. As shown schematically in Figure 1.1a., liquid metal is forced through a nozzle onto a cool, rotating wheel, which absorbs the super- and latent heat and causes solidification. A distinguishing feature of PFMS against other melt spinning processes is the close proximity of the nozzle to the rotating substrate. PFMS is known for its *high-throughput* and the *unique material properties* of its ribbons.

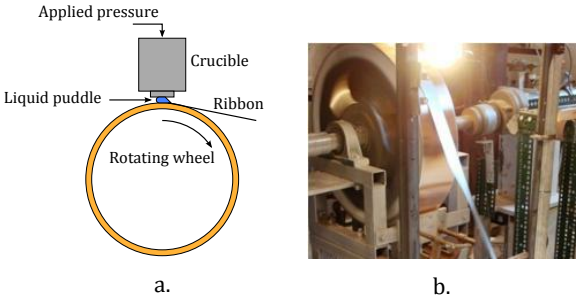

Figure 1.1: a. Planar-flow melt spinning is a process for forming thin metallic ribbons against a rotating chill-wheel; b.PFMS caster at Cornell University.

In a traditional casting process, raw material is melted and fed to the caster. The caster extracts heat from the metal and produces a solid component. To achieve final dimensions, the solid component is processed downstream of the caster by processes such as rolling to achieve its final dimensions, depicted in Figure 1.2. Traditional processes can be batch or *continuous*, but are typically *multi-stage*. An

example of a continuous, *multi-stage* casting process is the production of aluminum foil. Here, sheets of aluminum are passed through hot rollers post-solidification to achieve the desired thickness, usually 200 μm or less. The final rolling step is evident in the product which has a shiny and a dull side, owing to the fact that two thicknesses are rolled at the same time, producing a shiny surface on the side in contact with the roller, and a dull surface on the side in contact with the other piece of foil. [39]

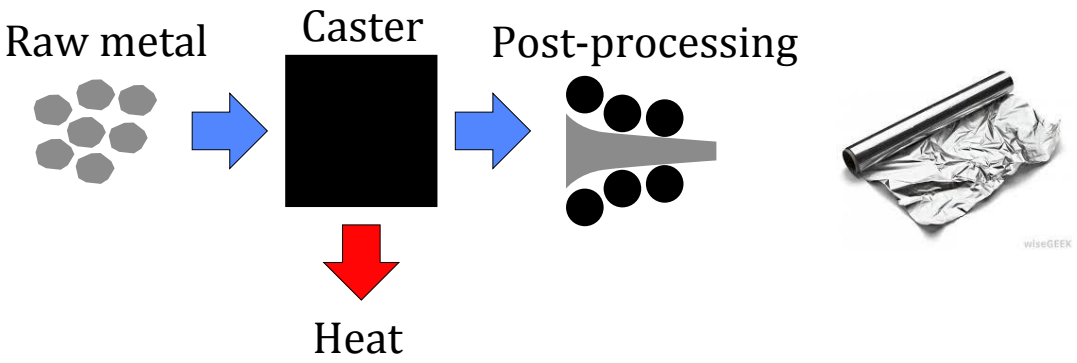

Figure 1.2: Traditional casting process requires post-processing steps to achieve product with desired dimensions.

In contrast to traditional casting, PFMS is a *single-stage* process for forming thin metallic components. In a single-stage process, final product is produced directly and post-processing steps are eliminated, shown in Figure 1.3. The dimensions of the product are specified by the process parameters, including nozzle width, applied over-pressure, nozzle-wheel spacing, wheel rotation rate. The elimination of post-processing reduces the energy cost of the process. A photograph of the PFMS caster at Cornell University is shown in Figure 1.1b., where the final product is seen departing from the wheel.

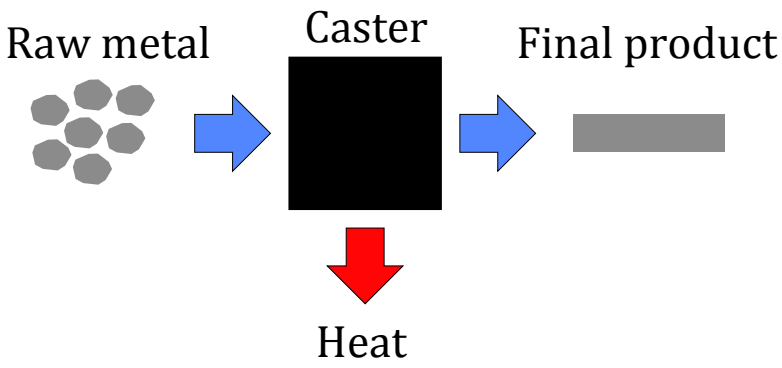

Figure 1.3: Single-stage casting process produces product with desired dimensions directly.

PFMS is capable of rapid solidification, yielding amorphous metals or metallic glasses. Metallic glasses are important in a variety of induction-based electromagnetic applications. Hasegawa (2000) [36] and Hasegawa and Azuma (2009) [37] discuss energy-conversion applications of these materials. One example is for use in electrical distibution transformers, where amorphous ribbon is wrapped into a solid core. The amorphous nature of the material greatly lowers the energy loss compared to traditional, crystalline metal cores [57].

There are a number of other applciations of thin amorphous metals. Herzer discusses applications to electro-acoustic surveillance devices[38]. Over the past decade, a variant of PFMS has been developed to continuously cast silicon substrates for solar-cells [35]. More recently, PFMS has enabled so-called 'nanosteels,' stainless steel foils with nanocrystalline structures that yield ultra-high strengths despite the thinness of a foil [7][6].

1.2 Puddle region

Although amorphous metallic glass can be solidified by PFMS, our working metal is typically an aluminum alloy which undergoes a phase-change on solidification. For this reason, henceforth, sketches of the puddle region show a sharp solidification front.

Solidification occurs between the crucible nozzle and the wheel surface. The distance between them, called the gap G, is sufficiently small that fluid inertia balances the capillary pressure, allowing a small liquid droplet called the puddle to form. The puddle region depicted in Figure 1.4. Typical parameters and definitions are found in Tables 1.1 and 1.2. Relevant dimensionless groups are given in Table 1.3.

Fluid enters the puddle with velocity u_{in} and density ρ_ℓ through the nozzle

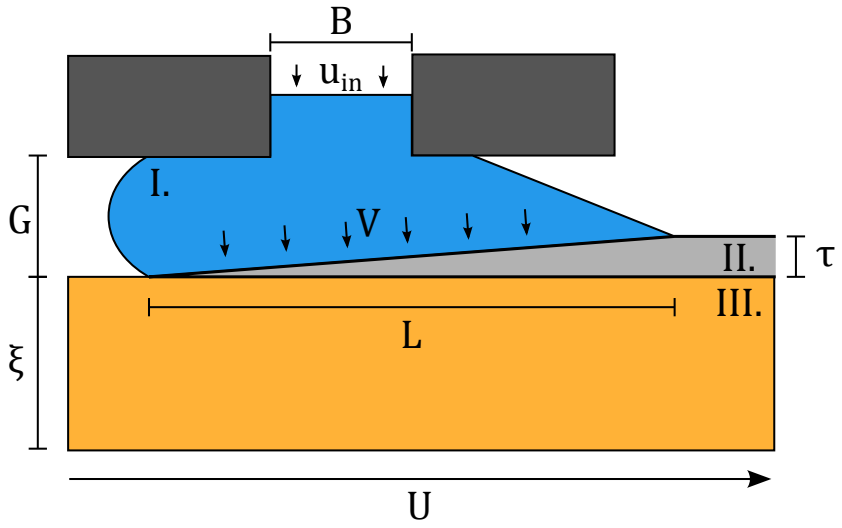

Figure 1.4: Typical parameters and definitions are found in Tables 1.1 and 1.2. Relevant dimensionless groups are given in Table 1.3.

with breadth B. At the bottom of the puddle, heat is extracted by the wheel

along a length L, causing ribbon to form. In the case of a crystalline metal, a sharply defined solidification interface between liquid and solid forms, and fluid can be thought of as moving into this interface with velocity V. The newly solidified ribbon with thickness τ and density ρ_s adheres to the wheel surface and translates away from the puddle with speed U. The puddle dynamics can be better understood by applying conservation of mass, energy and momentum. The liquid and solid ribbon will be treated as adjacent control volumes, denoted by numerals I. for the liquid and II. for the solid ribbon.

Process and product parameters		
Process parameters		
G	$0.5 - 1.3\ mm$	nozzle-wheel gap
U	$6 - 12\ m/s$	linear wheel speed
ΔP	$2500\ Pa$	applied gas crucible pressure
τ	$50 - 250\ \mu m$	ribbon thickness
W_r	$5\ cm$	ribbon width
L	$1 - 2\ cm$	puddle length
V	$0.1\ m/s$	solidification velocity
T_s	$987\ K$	crucible temperature
Nozzle geometry		
B	$1.6\ mm$	nozzle slot breadth
W	$5\ cm$	nozzle slot width
Melt and ribbon material properties: $Al - 7\%Si$		
ρ_ℓ	$2300\ kg/m^3$	liquid density
ρ_s	$2700\ kg/m^3$	solid density
$C_{p,\ell}$	$1080\ J/kg - K$	liquid heat capacity
$C_{p,s}$	$938\ J/kg - K$	solid heat capacity
μ	$1E-3\ Pa - s$	liquid viscosity
σ	$0.86\ N/m$	liquid surface tension (in air)
T_m	$887\ K$	melt temperature
ΔH_f	$3.87 \times 10^5\ J/kg$	latent heat of fusion
ΔH_s	$4.9 \times 10^5\ J/kg$	heat of solidification (latent + superheat)

Table 1.1: Typical values of process parameters and material properties

Wheel properties		
Wheel geometry		
R	30 cm	radius
C_w	1.91 m	circumference
ξ	1.27 cm	rim (wall) thickness
W_w	13.5 cm	width
Material properties		
ρ_w	8960 kg/m^3	density
$C_{p,w}$	385 $J/kg - K$	heat-capacity
k_w	200 $J/m^2 - K - s$	thermal conductivity†
α	5.8×10^{-5} m^2/s	thermal diffusivity
β	1.65×10^{-5} $1/K$	coefficient of linear expansion
E	1.28×10^5 Pa	elastic modulus
ν	0.3	Poisson ratio

Table 1.2: Wheel dimensions and material properties. † measured values.

Dimensionless Groups			
Geometry			
B/G		$1.5-3$	nozzle breadth-to-gap ratio
W/G		$25-100$	nozzle width-to-gap ratio
τ/G		$0.1-0.3$	thickness-to-gap ratio
L/G		$10-20$	puddle length-to-gap ratio
Dimensionless Numbers			
Re_U	$\rho GU/\mu$	10^4	wheel speed Reynolds number
$Re_{u_{in}}$	$\rho Gu_{in}/\mu$	10^3	inlet velocity Reynolds number
We_U	$\rho U^2 G/\sigma$	10^2	wheel speed Weber number
$We_{u_{in}}$	$\rho u_{in}^2 G/\sigma$	10^0	inlet veloccity Weber number
Ca_U	$\mu U/\sigma$	10^{-2}	wheel speed capillary
$Ca_{u_{in}}$	$\mu u_{in}/\sigma$	10^{-3}	inlet velocity capillary number
Fr_U	U^2/gG	10^4	wheel speed Froude number†
$Fr_{u_{in}}$	u_{in}^2/gG	10^4	wheel speed Froude number†
ε_s	τ/L	10^{-2}	solidification parameter
Ste	$C_{p,\ell}(T_s-T_m)/\Delta H_f$	10^{-1}	liquid Stefan number
Pe	$\rho_w \xi/\alpha$	10^2	substrate Peclet number

Table 1.3: Typical values of dimensionless groups. † $g = 9.8\ m/s$

1.3 Fluid dynamics

1.3.1 Conservation of mass

For a puddle at steady-state, conservation of mass can be expressed

$$\int_A \rho(\mathbf{V} \cdot \mathbf{n}) = 0. \tag{1.1}$$

A represents the area of the control surface, with one dimension extending into the page. ρ is the density and $\mathbf{V} \cdot \mathbf{n}$ is the component of the velocity normal to the control surface.

Applying 1.1 to I. c.f. Figure 1.4, it is found that

$$\rho_\ell B u_{in} = \rho_\ell L V$$

and similarly for II.

$$\rho_\ell L V = \rho_s \tau U.$$

The length of the solidification region is not L but actually $\sqrt{L^2 + \tau^2}$. However, since $(\tau/L) << 1$, it can be approximated as L. The mass balances can be combined

$$\rho_\ell B u_{in} = \rho_\ell L V = \rho_s \tau U. \tag{1.2}$$

Some authors will omit the densities in equation 1.2. For the case of aluminum, the error in doing this is about 15%. Note that V as it is defined above is a suction velocity: the velocity of the fluid as it enters the solidification front. A solidification velocity V_s defined on the ribbon side of the interface and directed into the mold could also be used. V and V_s are related by

$$\rho_\ell V = \rho_s V_s. \tag{1.3}$$

1.3.2 Conservation of momentum

The integral form of steady momentum conservation is

$$\int_A \rho \mathbf{V}(\mathbf{V} \cdot \mathbf{n}) = \sum \mathbf{F} \tag{1.4}$$

$$\tag{1.5}$$

where $\mathbf{F}$ are the forces acting on the system. We will let

$$\sum \mathbf{F} = \mathbf{F_g} + \mathbf{F_s}$$

where $\mathbf{F_g}$ are body forces and $\mathbf{F_s}$ are forces applied by the bounding surfaces. $\mathbf{F_s}$ includes pressure forces, solid surface forces and surface tension forces at the free-interfaces. All forces are vector quantities, having a vertical y-component and a horizontal x-component. The only body force considered is gravity (subscript g) which will act soley in the y-direction. Applying equation 1.5 to control volume I. yields

$$0 = F_{s,x} \tag{1.6}$$

$$\rho_\ell W \left[u_{in}^2 B - V^2 L\right] = F_{g,y} + F_{s,y}. \tag{1.7}$$

The x-equation simply states that the forces acting on the surfaces balance. Estimating $F_{g,y}$ as $\rho_\ell g W G L \sim 10^{-2}\ N$, it is found that body forces are about 10% of the inertial terms on the left-hand-side, which are $O(10^{-1}\ N)$.

Applying equation 1.5 to control volume II. yields

$$F_{s,x} = -\rho_s W U^2 \tau \tag{1.8}$$

$$F_{g,y} + F_{s,y} = \rho_\ell W V^2 L \tag{1.9}$$

The y-equation simply states what the normal force applied by the substrate must be to counteract the forces of the incoming fluid. The x-equation however yields an estimate for the lateral force applied by the wheel to the ribbon. This force is a lower bound of the adhesion force of the ribbon to the wheel, which will be considered in detail in Chapter 2. Normalizing $F_{s,x}$ by W and calling this value the adhesion energy γ, the adhesion energy can be estimated to be $\gamma \approx 30\ N/m$. This value is consistent with the $\gamma \approx 60\ N/m$ determined in Chapter 2 by other means.

1.3.3 Fluid dynamics literature

The solidification region in PFMS is shown schematically in Figure 1.4. Molten metal, initially held in a heated crucible, is forced through a nozzle with breadth B ($10^{-3}\ m$) by applied gas pressure into the solidification zone. The fluid, with density ρ_ℓ, exits the nozzle with speed u_{in} ($1\ m/s$). Variable definitions and typical values are summarized in Table 1.1. A liquid puddle forms between the nozzle and the wheel and is held in place by surface tension σ. The narrow distance between the nozzle and chill-wheel, called the gap G ($10^{-3}\ m$), distinguishes PFMS from chill-block melt spinning.

The small gap size and relatively high surface tension of metals allow the cap-

illary pressure σ/G to balance the fluid inertia $\rho_\ell u_{in}^2$. Viewing the puddle in the direction of the wheel axis from the cast direction reveals two puddle-air interfaces, depicted in Figure 1.1: a highly curved mensicus upstream of the fluid inlet called the upstream mensicus (USM) and a long, nearly linear mensicus downstream of the inlet called the downstream mensicus (DSM). The puddle length L (10^{-2} m) is defined as the distance in the cast direction between these mensici along the wheel surface. Along this length, a solidification front forms and grows with speed V_s (10^{-1} m/s). Upon solidification, ribbon with thickness τ (10^{-4} m) and density ρ_s adheres to the wheel and is translated out of the puddle with wheel speed U (10 m/s).

Assuming that the puddle achieves steady-state, the simple mass balance given by Equation 1.2 relates the velocities and lengths in the puddle,

$$\rho_\ell B u_{in} = \rho_\ell L V = \rho_s \tau U. \tag{1.10}$$

This simply states that the mass entering the puddle = mass solidified = mass exiting the puddle. Of these quantities, B is set by the nozzle geometry, U is controlled by the operator, and τ is measured post-cast. It is possible to estimate L photograpically, but this requires high resolution images and image analysis, the difficulties of which have been discussed by Cox (2011) [21]. All other quantities in equation 1.10 must be inferred from the mass balance.

Dimensional analysis of the fluid flow in the puddle elucidates the relevent physics. Two sets of dimensionless numbers, summarized in Table 1.3, can be constructed depending on the velocity chosen, u_{in} or U. The inlet velocity u_{in} is a characteristic fluid velocity in the puddle, but must be inferred from Equation 1.10. Alternatively, the wheel speed U is set by the operator and has been used as the characterstic

velocity in much of the spin casting literature, but may not be representative of the actual fluid velocity in the puddle. Only those which use u_{in} are discussed here.

Capillary and inertial pressures balance, shown by the Weber number $We_{uin} \equiv \rho_\ell u_{in}^2 G/\sigma \sim 10^0$. Viscous contributions are small relative to inertia and capillarity, shown by the Reynolds number $Re_{uin} \equiv \rho_\ell u_{in} G/\mu \sim 10^3$ and the capillary number $Ca_{uin} \equiv \mu u_{in}/\sigma \sim 10^{-3}$. Gravitational effects are also small, shown by the Froude number $Fr_{uin} = u_{in}^2/Gg \sim 10^2$ and Bond number $Bo = \rho_\ell G^2 g/\sigma \sim 10^{-2}$. Thus, the relevant forces in ascending order of magnitude are

$$\text{viscous} < \text{gravitational} < \text{capillary} \sim \text{inertial}.$$

A review of the fluid mechanics literature pertanent to spin casting is given by Steen and Karcher (1997) [69] and Karcher and Steen (2001)[43][44]. These authors show that solidification in PFMS is a *feed limited* process, limited by how quickly material can be fed to the solidification region. Another important finding in the literature is that, to first order, the fluid-flow and heat-transfer *decouple*. The decoupling is characterized by a solidification parameter $\epsilon_s \equiv \tau/L << 1$, the slope of the solidification front. In the limit of $\epsilon_s \to 0$, the direction of momentum transfer is perpendicular to the direction of heat-transfer, decoupling the equations of heat and momentum transfer [15]. A similar result was found numerically for chill-block casting by Takeshita and Shingu (1983), who also found that the solidification was dominated by momentum, rather than heat-transfer. Varying the puddle-wheel contact heat-transfer coefficient in their simulation, they found no effect on the ribbon thickness in the range of realistic heat-transfer coefficients [74].

Flow in the puddle region is characterized by high Reynolds number, as inertia dominates viscous effects. Accordingly, a number of authors have modeled flow in

the puddle by applying a Bernoulli-type balance along streamlines in the puddle, assuming the flow is inviscid and irrotational. Huang (1981) combined a Bernoulli-type balance with a mass balance in the downstream region to derive a relationship between the pressure at the inlet and the ribbon thickness [40]. Using a combined mass and Bernoulli balance, Carpenter and Steen (1997) related ribbon thickness to over-pressure (scaled by capillary pressure) and nozzle breadth [15]. Ibaraki (1996) extended the Bernoulli balance approach to include engineering loss coefficients [41].

Despite the success of the Bernoulli balance models of the puddle, vortices are thought to be present in the liquid. Using a model for vorticty in the puddle, Reed, et al. (2001) found a streamline beginning at the inlet and decaying into a solidification boundary layer at the wheel, which separated the puddle into regions of flow recirculation [65]. Using a volume-of-fluids numerical approach, Bussmann, et al. (2002) predicted the presence of up- and downstream recirculation regions [10]. Similar results were numerically found by Bichi, et al. (2008) and Liu, et al. (2009) [3][54]. In Figure 1.4, direction of fluid flow indicated by arrows is vertical at the inlet and nearly vertical at the solidification front. The presence of vortices or circulation regions in the puddle dictates that fluid parcels do not travel along a monotonic streamline across the puddle. The presence of a recirculation region is thought to play a role in the vibration physics of the puddle, discussed in the next section.

1.3.4 Periodic feature formation

Localized thickness variations in the ribbon, most often referred to as ribbon 'defects', are observed over many length scales. These variations are caused by fluid flow, heat-transfer, and interfacial motions of the puddle mensici. Whether these defects affect the quality of the product depends on the application, but, in any case, precise understanding and control of them is desired. As defect implies an undesired or quality-lowering phenomena, we use the additional terms 'feature' or 'thickness variation' to refer to them.

Praisner, et al. (1995) discuss a number of ribbon features in PFMS. In particular, they observed 'streaks' or 'dimples' in the product, as well as two distinct periodic features [62]. These *periodic* features have been discussed elsewhere in the literature. Both defects are visible to the eye on the wheel-side and on the air-side of the ribbon. A lower frequency defect called crosswave (CW) was observed to appear with 1 cm spacing and a frequency of 1 kHz by Byrne, et al (2006). Using dimensional analysis, it was found that the frequency of this defect was proportional to the characterstic capillary frequency, $f_c \equiv (\sigma/\rho_\ell G^3)^{1/2}$, suggesting that the defect is related to capillary vibrations of the puddle [12].

The two periodic defects are caused by *unsteady* fluid motion. Unlike the steady momentum balances of Section 1.3.2, time-dependent vibrations of the upstream meniscus (USM) cause variations in the final product. It is believed that vibrations of the upstream mensicus allow air bubbles to become entrained betweeen the puddle and the wheel. The air pockets act as an insulator, reducing the rate of heat-transfer from the puddle to the wheel, locally reducing the ribbon thickness. Thus, the shape of the solidified metal on the wheel side is caused by the physical

presence of air pockets, and the shape on the air-side is caused by reduced solidification rates due to the heat-transfer interruption caused by air entrainment. The heat-transfer to the wheel was intentionally altered by Bryne, et al. (2006), who used a high-powered laser to create local hot points on the wheel, causing dimples in the ribbon product. They also painted boron-nitride in patterns on the wheel to act as a heat-transfer interruption, and were able to create desired corresponding patterns on the ribbon [13].

A second periodic feature, called herringbone (HB), was discussed by Cox and Steen (2013). This defect, while similar in appearance to CW, appeared with 1 mm spacing and a corresponding frequency of 10 kHz. Using dimensional analysis, it was found that HB shares the capillary frequency scaling of the CW, but also depends on a wheel-speed Weber number We_U, defined in Table 1.3. CW was found to be independent of the We_U. Furthermore, Cox and Steen found that the geometry of the puddle is different for the formation of CW and HB. A necessary condition for the formation of HB is that the USM *must* pin at the nozzle inlet slot. If the USM depinned, CW was observed. They conclude that the flow of metal from the nozzle is directly down into the solidification region during HB, but that flow separation in the depinned case allows a 'buffer' region of fluid to form which damps out the Weber number physics involved in HB formation [20]. Meniscus vibrations subject to various contact line and flow conditions are the subject of Chapter 4.

It should be noted that periodic casting features need not be related to surface tension. In the thickness data presented by Theisen, et al. (2010), thickness variations on the order of $0.1 - 1$ m are apparent in each wheel revolution. This feature

is called the out-of-roundness feature and is caused by eccentricities in the casting wheel due to machining imperfections. Since the position of the nozzle relative to the wheel center is fixed, out-of-roundess of the wheel causes periodic changes in the gap height, which directly influences the fluid flow in the puddle [76].

1.4 Heat transfer

Conservation of energy

Refering again to Figure 1.4, the integral form of steady energy conservation is

$$\int_A \rho e(\mathbf{V} \cdot \mathbf{n}) = Q, \tag{1.11}$$

$$e \equiv \rho C_p T + gz + V^2/2 \tag{1.12}$$

where ρ and C_p are the density and heat capacity of liquid (ℓ) or solid (s), g is gravitational acceleration, z is the height relative to a reference point, $V = [V_s]$ is the speed and T is the temperature. Here it is assumed that the internal energy of the system can be represented by $\rho C_p T$, relative to a zero-temperature.

Applying 1.12 to control volume I., recalling W is the nozzle slot width,

$$Q_1 = \rho_\ell C_{p,\ell} W(Bu_{in}T_h - LVT_m) + E_{mech,1} - \sum Q_{loss} \tag{1.13}$$

$$E_{mech,1} = \rho_\ell W \left\{ Bu_{in} \left(u_{in}^2/2 + gG \right) - LV \left(V^2/2 + g\tau \right) \right\}. \tag{1.14}$$

$E_{mech,1}$ contains potential and kinetic energy terms. Q_{loss} represents any heat lost from the puddle to the surrounding air by convection or radiation. Both $E_{mech,1}$ and $\sum Q_{loss}$ have been estimated to be at least 10^3 smaller than the sensible heat term in Q_1, so these will be neglected. From the mass balance, $Bu_{in} = LV$, so

these can be rewritten

$$Q_1 = \rho_\ell C_{p,\ell} W B u_{in} (T_h - T_m) \tag{1.15}$$

Equation 1.12 can be applied to control volume II., however, an additional term must be included to account for the heat generated at the solidification interface, ΔH_f

$$Q_2 = Q_1 + \rho_\ell C_{p,\ell} W B u_{in} \Delta H_f + E_{mech,2} - \sum Q_{loss} \tag{1.16}$$

$$E_{mech,2} = \rho_\ell W B u_{in} \left\{ \left(V^2/2 + g\tau \right) - \left(U^2/2 \right) \right\}. \tag{1.17}$$

As before, $E_{mech,2}$ and Q_{loss} are small. Letting $Q_f \equiv \rho_\ell C_{p,\ell} W B u_{in} \Delta H_f$,

$$Q_2 = Q_1 + Q_f \tag{1.18}$$

Entering in typical values, given in Tables 1.1 and 1.2, the approximate values of Q_i are

$$Q_1 = 1.4 \times 10^4 \ J \qquad Q_f = 5.2 \times 10^4 \ J \qquad Q_2 = 6.6 \times 10^4 \ J.$$

Treating Q_2 as the total, the heat associated with solidification represents about 79% of the total, while the superheat Q_1 is about 21%. In Chapter 3, the heat-up of the wheel substrate is considered. A segment of the wheel given by control volume III. in Figure 1.4 is a solid body, experiencing heating from the puddle above. The CV moves with constant speed U. Unlike the puddle, which constantly has mass/energy added and removed, the segment of wheel will experience the puddle multiple times. Since the wheel isn't actively cooled, it accumulates energy, requiring an *unsteady* energy balance. The integral in equation 1.12 will integrate to zero, since the velocity is constant, but now an unsteady term is added

$$\frac{d}{dt} \int_\Omega (\rho_w e) = Q. \tag{1.19}$$

Since kinetic and potential energy aren't changing in time, this simplifies to

$$\rho_w C_{p,w} \frac{dT_w}{dt} = Q_2 - \sum Q_{loss} \tag{1.20}$$

where T_w is the time-dependent wheel temperature, and Q_2 given in Equation 1.16. Note that the only heat source given here is from the puddle Q_2. As the control volume leaves the puddle, the ribbon may still adhere to it, transfering more heat to the wheel. The heat from this secondary quench (the term used in Chapter 2) Q_{sq}, is estimated to be

$$Q_{sq} = \rho_s C_{p,s} W_r \tau U (T_m - T_d) \approx 1.4 \times 10^4 \ J/s$$

where W_r is the ribbon width, T_m is the melt temperature of the ribbon and T_d is the temperature after solidification at which the ribbon breaks wheel contact. If $Q_2 + Q_{sq}$ represents the total heat input to the wheel (per revolution), Q_{sq} represents about 18% of the heat and Q_2 is 82%. Each revolution, the wheel temperature will have risen, and a new heat input is added. This approach is used in Chapter 3.

1.4.1 Heat transfer literature

Liquid metal exits the crucible at a superheat temperature T_s. The cooling of liquid metal and ribbon can be viewed as two distinct quenching processes: a primary and a secondary quench. During the primary quench, super- and latent heat are transferred to the wheel, causing solidification into thin ribbon. This occurs principally in the puddle region of extent L. The achieved quench rates have been observed to be as high as 10^7 K/s, corresponding to ribbon growth rates of 10 cm/s. After solidification, ribbon-wheel contact is maintained until contact is broken via mechanical means or until contact breaks naturally, in a process called

natural detachment. After solidification, during the secondary quench, the ribbon continues to transfer thermal energy to the wheel after solidification, causing it to cool and tend to contract. The adhesion during this secondary quench was first studied by Liebermann (1984) [51] and is the subject of Chapter 2.

In the absence of internal cooling, the temperature within the wheel increases during a cast. As the wheel temperature rises, the wheel tends to expand outward. As this happens, the nozzle-wheel gap size decreases and restricts the fluid flow into the puddle region, reducing the ribbon thickness. This, in-turn, reduces the amount of thermal energy going into the wheel. Though the fluid dynamics and heat-transfer of ribbon formation uncouple to first order, there is a feedback coupling due to this wheel deformation. Theisen, et al. (2010) discuss this process in depth and provide a simple deformation model which captures the effect [76]. The nature of the wheel heat-up process is discussed in Chapter 3.

A number of authors have noted that there is imperfect contact between the solidifying metal and the wheel during solidification, due to incomplete liquid wetting and air-entrainment between the puddle and wheel. Much of the literature has focused on quantifying this imperfect contact by fitting a puddle-wheel heat-transfer coefficient as a function of casting parameters. An in-depth literature review is given in Chapter 3.

1.5 PFMS at Cornell University

The PFMS casting apparatus is located in Olin Hall, room 101. Metal is placed in a graphite crucible, Figure 1.5. The crucible is sealed on the top and bottom by two graphite caps. At the top of the crucible is a cap which has two gas tubes and a ceramic stopper rod, Figure 1.5. The bottom cap includes a nozzle, Figure 1.6. The nozzle has a fitted ceramic insert (white piece) through which metal flows. The insert has a rectangular slot with breadth B and width W_r. During a cast, argon is passed through the gas tubes in the top cap to evacuate air from the crucible (to minimize oxidation) and to create pressure in the crucible, which will force liquid metal through the nozzle. Flow of metal is controlled by a stopper at the end of a rod, which is removed at the start of a cast.

The crucible is suspended above the wheel inside of insulated copper coils, Figure 1.7. An electrical current is passed through the coils by a Lepel induction heater, which causes the metal in the crucible to heat by radio-frequency resistance heating. The wheel is rotated by an electrical motor. A side view of the wheel and motor is shown in Figure 1.8.

Prior to the cast, a known amount of solid metal (typically $Al - 7\%Si$) is placed inside of the crucible. The crucible is sealed and inserted inside the copper induction coils above the wheel. The distance between the nozzle and the wheel, called the gap G, is set. The wheel is then polished with sandpaper to prepare its surface for casting. The metal is heated by the induction heater to a temperature above its melting point. For $Al - 7\%Si$, a temperature of 714 $^{\circ}C$ is used, giving a superheat that is about 100 $^{\circ}C$ above its melt temperature. The wheel rotation rate is set and a base-pressure is applied in the crucible using argon. The stopper

Figure 1.5: Assembled graphite crucible, with gas tubes and ceramic stopper rod.

rod is pulled, allowing liquid metal to exit the crucible through the nozzle insert. To compensate for the loss of static head pressure as the liquid drains, the argon pressure is ramped.

Post-solidification, ribbon collects on the floor in front of the casting wheel. Ribbon is spooled and typically cut into 15 *cm* segments. Thickness of each segment is

Figure 1.6: Nozzle cap seals the bottom of the crucible. During a cast, liquid metal flows through a ceramic insert (white piece) which fits in the nozzle. Insert shown here after a cast with frozen metal shards.

determined by the segment mass, length, and width. The wheel speed is measured by a tachometer during a cast. The wheel is *not* actively cooled, and its temperature at two radial positions within the wheel is measured by embedded K-type thermocouples. As the wheel heats, it expands, reducing the gap. Deviations from the gap set-point are measured by a capacitance gauge.

High-speed video is captures images for many casts. Two cameras are used: a Kodak EktaPro and a Redlake MotionXtra HG-100K system. Prior to 2008, the Kodak camera was focused on the puddle for determining puddle length or to examine mensicus behavior. In 2008 the Redlake camera was introduced, capable of

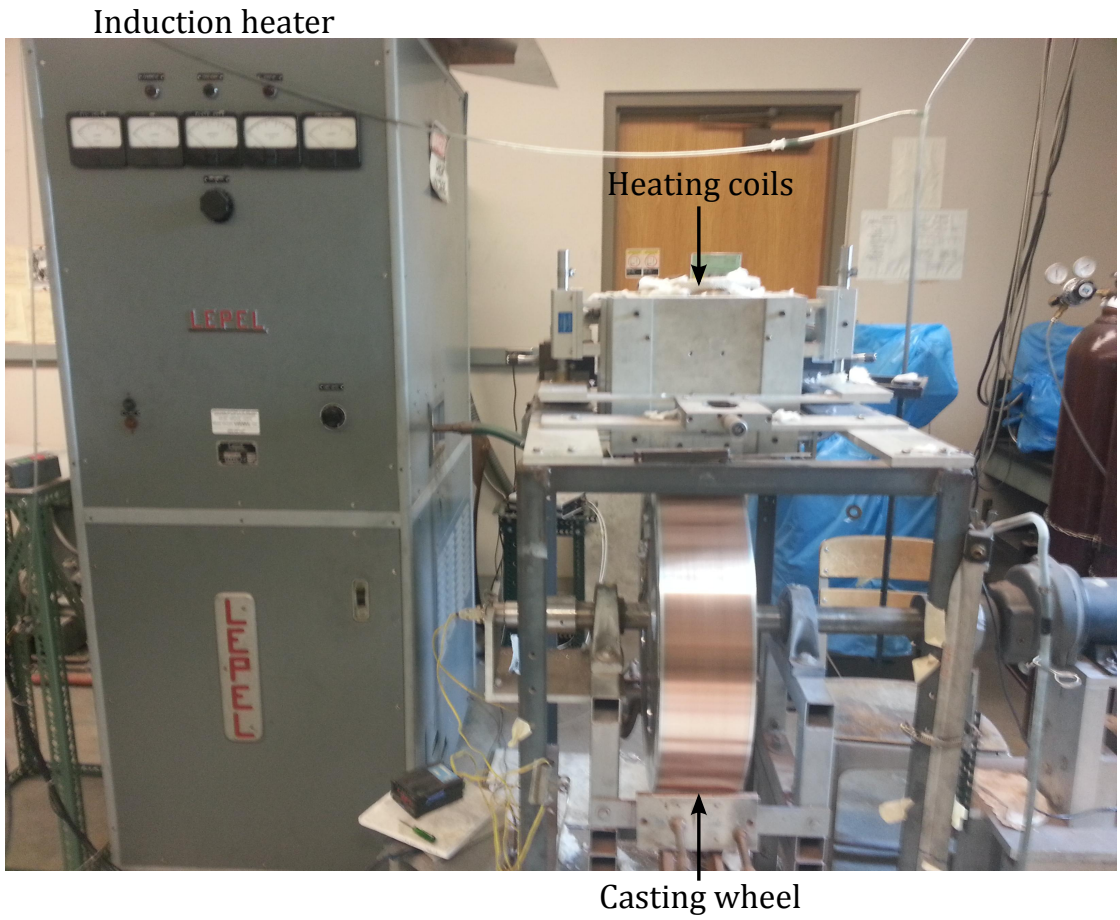

Figure 1.7: Copper wheel supported by steel super-structure (right front). Metal is held in a crucible inside of heating coils, suspended above the wheel (right middle). Heat is supplied by a Lepel induction heater (left).

frame-rates up to $100,000$ fps, for capturing puddle videos. The Kodak camera was later used to capture images of the ribbon as it broke contact with wheel. These images are used to study the ribbon sticking distance.

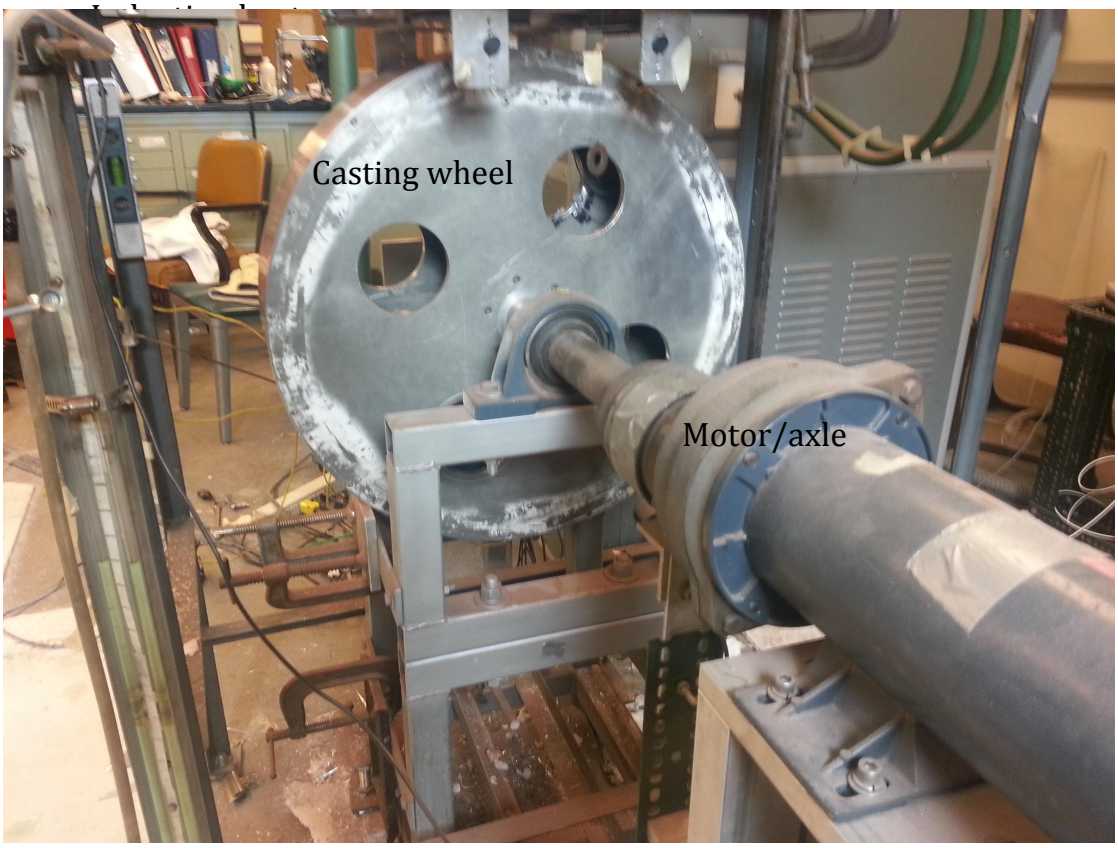

Figure 1.8: Side-view of the wheel, rotated by an electrical motor.

1.6 Objectives

As ribbon solidifies, it forms adhesive bonds with the wheel. The ribbon wraps around the wheel until contact is broken either by external means (i.e. a scraper) or naturally through a thermo-elastic cooling process. The focus of Chapter 2 is the adhesion of the ribbon as it solidifies on the wheel and the subsequent process of ribbon detachment from the wheel. This work builds on experimental/theoretical studies of ribbon adhesion by Liebermann [51] and Maringer [56]. Combining a ribbon cooling model with the classic Kendall model of elastic film 'peel-off' from a substrate [47], an equation for ribbon sticking distance is derived. This enables prediction of an event called catastrophic adhesion, in which the ribbon wraps fully around the wheel. This quantitative treatment puts a firm basis under on Liebermann's qualitative discussion [51].

The focus of Chapter 3 is the study of heat-transfer in the wheel. Various conduction models are derived from the full 3D conduction problem. A semi-empirical equation which takes ribbon dimensions/properties as an input and outputs temperature profiles in the wheel is derived. The result is an extension of classical conduction models, but for systems with spatial- and time-dependent boundary conditions. Several heuristic guidelines are obtained to explain various features of the wheel temperature data.

In Chapter 4 the motions of the upstream meniscus as they relate to periodic ribbon features are considered. The effect of contact line constraints are examined, as well as the effect of flow near the interface. The motions of the USM are related to experimental observations, guided by work presented by Byrne, et al. (2006) [12] and Cox and Steen (2013) [20].

Several auxiliary studies are discussed and lab updates performed since the Spring of 2008 are recorded in Chapter 5. Future work is discussed in Chapter 6

Worked performed during an internship at Dow AgroSciences in Summer 2012 is discussed in Chapter 7. Spray atomization by agricultural nozzles is examined. Liquid sheets sprayed into air are subject to hydrodynamic instabilities, resulting in their breakup into droplets. Previous work noted that single-phase sprays atomize differently than oil-in-water emulsion sprays. In this chapter, a review of liquid sheet stability is presented. Then, a new model for emulsion sheet breakup is presented and compared with data. Though not related to PFMS, the physics and stability analysis presented in this section is closely related to the meniscus vibration analysis presented in Chapter 4.

The appendix summarizes the PFMS cast data since Spring of 2008. Refer to the Cox thesis (2011) [21] for earlier cast data.

CHAPTER 2

ADHESION UPON SOLIDIFICATION AND DETACHMENT IN THE PLANAR-FLOW MELT SPINNING OF METALS.*

Abstract

In planar-flow melt spinning, liquid metal is rapidly solidified, against a heat-sink wheel, into thin ribbons which adhere to the substrate wheel. In the absence of a blade to mechanically scrape the ribbon off the wheel, it may wrap fully around and re-enter the solidification region, called 'catastrophic' adhesion. Otherwise, detachment occurs part way around the wheel, called 'natural' detachment. Natural detachment occurs through a release of thermo-elastic stress after sufficient cooling of the ribbon, according to prior studies. This note extends prior work by invoking a crack propagation view of natural detachment which, when combined with a simple model of the thermoelastic stress build-up and ribbon cooling, yields an adhesion/detachment criterion characterized by an interfacial adhesion/fracture energy γ. For aluminum-silicon alloys frozen against a copper substrate, we report $\gamma \approx 60 N/m$. The criterion can be used to predict detachment once a heat transfer coefficient is known. We obtain this parameter from natural detachment experiments and then use it to predict catastrophic adhesion in a semi-empirical way. Our note puts a quantitative foundation underneath qualitative discussions in the literature. Alternatively, it demonstrates how the interfacial strength of adhesion, a property only of the pair of adhering materials, might be measured based on sticking distance experiments. Adhesion upon solidification and subsequent detachment can be important to controlling fabrication in a wide range of material

*Manuscript accepted for publication by Metallurgical and Materials Transactions B, coauthor PH Steen.

casting processes. On the other hand, the science of adhesion upon solidification and detachment are poorly understood. This note may benefit both application and science.

Main

Adhesion upon solidification and subsequent detachment can be important to controlling fabrication in a wide range of material casting processes. On the other hand, the science of adhesion upon solidification and detachment are poorly understood. This note may benefit both application and science.

In planar-flow melt spinning (PFMS), liquid metal contacts a rotating wheel and rapidly solidifies into thin ribbons or sheets [59], Figure 2.1a. During solidification, the metal forms adhesive 'bonds' with the wheel. This adhesion can hold the ribbon attached until it re-enters the solidification zone a full revolution later, a case which Liebermann called 'catastrophic adhesion' since it may cause diminished product integrity, equipment damage, and casting failure [51]. Alternatively, the ribbon may part from the wheel prior to a full revolution by being mechanically removed or by naturally detaching. The subject of this work is the natural detachment event and catastrophic adhesion. Figure 2.1b. is a photograph of the PFMS apparatus used in this study. Here ribbon is seen to detach near $1/4$ of a revolution.

PFMS can achieve sufficiently rapid quench rates ($10^4 - 10^7\ K/s$) to yield amorphous metals with remarkable electromagnetic and mechanical properties, impor-

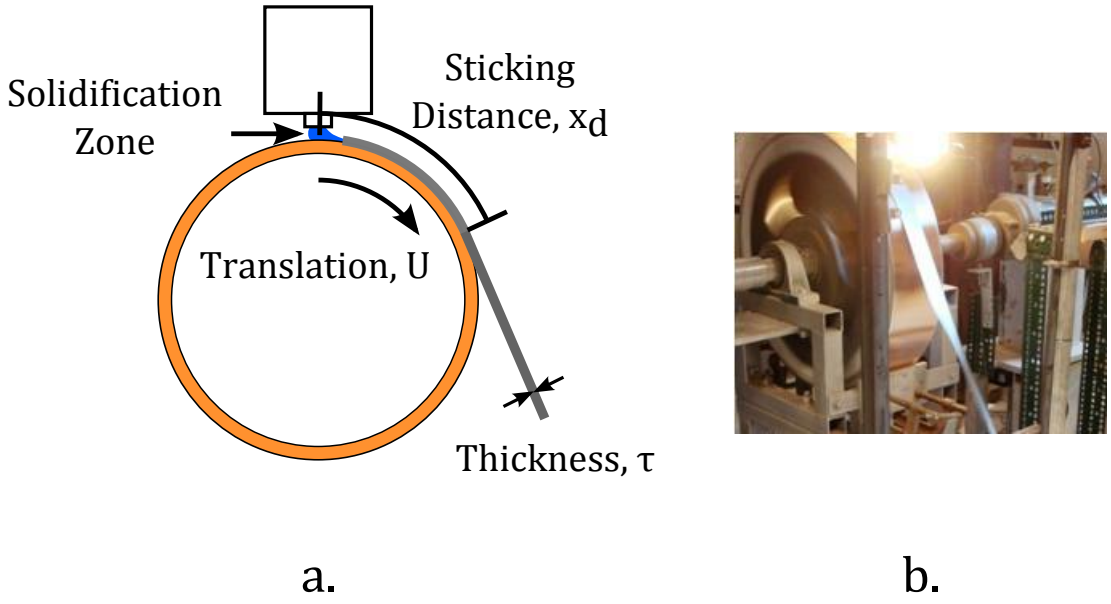

Figure 2.1: a. Schematic of PFMS showing sticking distance x_d. Molten metal (blue) is forced from a crucible into contact with the rotating wheel surface where a solidification zone forms and a solid ribbon (gray) freezes. The ribbon of thickness τ detaches at a distance x_d from the nozzle, measured along the wheel surface. b. PFMS apparatus used in this study. Ribbon detaches within 1/4 of a wheel revolution.

tant to applications achieving improved energy efficiency [37] or high strength-to-weight ratio materials [7][6], for example. A peak of interest in PFMS occurred in the 1980s. Interest has renewed recently as applications have broadened [50].

During the conversion of molten metal to final product, the metal transfers thermal energy to the wheel in two, sequential quenching processes. During the primary quench, of short duration (10^{-3} s), the wheel absorbs latent heat and solid ribbon is formed. During the secondary quench, sensible heat of the solid ribbon is transferred to the wheel until ribbon-wheel contact is broken. The duration of the secondary quench (10^{-2} s) can influence the material properties of the product. For example, the brittleness of an iron alloy was found to increase as the secondary quench time decreased. Those ribbons which were mechanically removed earlier showed increased brittleness which was thought to be due to iron cluster formation, attributed to a shorter secondary quench (ie. remaining longer at higher temperatures) [66].

Maringer reported the detachment mechanism to be thermo-elastic cooling of the ribbon during the secondary quench [56]. As the ribbon cools from the melting temperature T_m, it would like to contract but is frustrated by adhesion to the substrate, creating stress on the adhesive bonds formed earlier. Once the stress is sufficiently large, the bonds are broken and the ribbon breaks contact. Natural detachment occurs when the ribbon reaches a critical cooling $T_m - T_d$, corresponding to a critical stress σ. The magnitude of these thermo-elastic stresses was estimated by Maringer to be

$$\sigma = E\beta(T_m - T_d), \tag{2.1}$$

Properties and Parameters

Symbol	Typical Value	Description
Al-Si Ribbon		
ρ	2700	solid density, kg/m^3
ρ_ℓ	2300	liquid density, kg/m^3
C_p	938	heat capacity, $J/kg-K$
τ	1.5×10^{-4}	thickness † , m
T_m	887 (614)	melt temperature, K ($^\circ C$)
β	6.9×10^{-7}	coefficient of volumetric expansion, $1/K$
E	6.9×10^{8}	elastic modulus, Pa
Δh	4.9×10^{5}	heat of solidification, J/kg
Cu-Be Wheel		
k	200	thermal conductivity † , $J/m-K-s$
U	10	linear speed † , m/s
C_w	2	circumference † , m
T_s	298(25) – 782(509)	surface temperature, K ($^\circ C$)
$T_{s,0}$	298 (25)	initial surface temperature, K ($^\circ C$)
n	5 – 50	duration of cast † , revolutions
Detachment		
T_d	782 (509)	detachment temperature † , K ($^\circ C$)
H	1500	heat-transfer coefficient, J/m^2-K-s
γ	62	ribbon-wheel adhesion energy, N/m
σ	10^9	critical detachment stress, Pa

† measured values.

Table 2.1: Variable definition and typical values for Al-Si cast onto Cu-Be wheel. When alloy properties of ribbon and wheel were unknown, properties were taken for pure Al and Cu, respectively. Δh includes latent heat and 100 K superheat.

where symbols and typical values are given in Table 1. The estimated detachment stress for the Al-Si alloys cast in this study is on the order of 2.1×10^8 Pa. Note that for an alloy, there is not a single melting temperature. 7% Al-Si has liquidus and solidus temperatures of 887 $K(614^\circ)$ and 850 $K(577^\circ)$, respectively. The difference between these is 6.4%, as it close to its eutectic point (12.2%). The liquidus temperature will be used as the 'melt' temperature, T_m.

Maringer goes on to discuss the casting parameters that influence ribbon adhesion in melt-drag spin casting, a closely related process: substrate surface temperature, surface chemistry, surface geometry, velocity, and surface maintenance, and melt superheat, chemistry, and ambient air conditions [56]. Maringer's observations were of amorphous ribbon while our observations are of crystalline ribbon formation. The difference in phase change behavior occurs during the primary quench which, for purposes of detachment predictions, can be ignored.

The sticking distance, x_d, is the distance from the solidification zone to the point of detachment, Figure 1. In the absence of mechanical removal, detachment is considered natural if sticking distance is less than the circumference of the wheel, $x_d < C_w$. Liebermann, in a study of chill-block melt spinning, observed that for catastrophic adhesion, the rate of increase of sticking distance was initially slow followed by a sudden rise [51]. Our purpose is to provide a mathematical underpinning for Liebermann's observations and to relate our experimental observations.

A model for ribbon cooling during the secondary quench provides the underpinning. Consider a segment of ribbon with thickness τ, width W, density ρ, and heat capacity C_p in contact with a wheel translating at speed U and surface temperature T_s, Figure 2.2. Ribbon-to-wheel heat transfer is governed by a heat-transfer coefficient H. The initial ribbon temperature is taken to be the melting temperature T_m. Ribbon cooling is assumed to follow a Newtonian-type model

$$\rho C_p \tau \frac{dT}{dt} = H\,(T_s - T) \tag{2.2}$$

$$T(t=0) = T_m \tag{2.3}$$

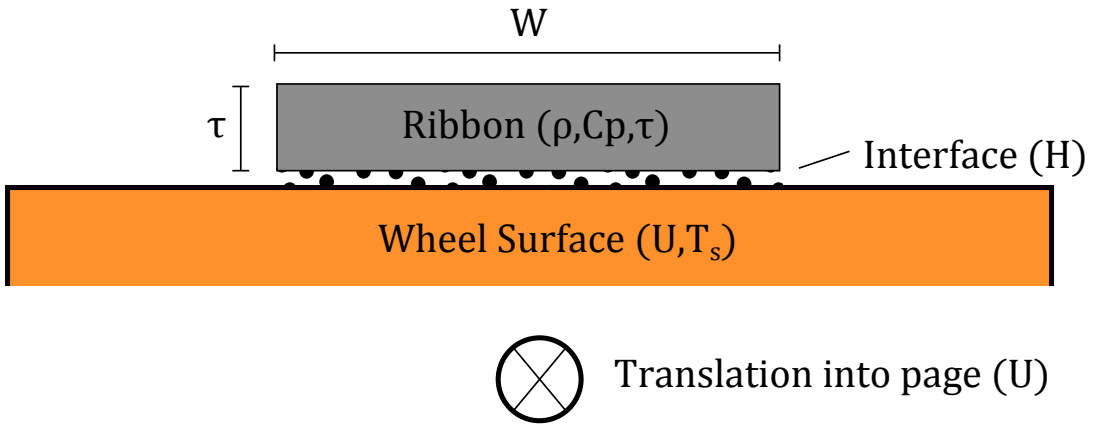

Figure 2.2: Control volume with width W, thickness τ, translating with speed U in contact with a substrate with surface temperature T_s. Heat transfer governed by heat-transfer coefficient H.

where ribbon temperature T is a function of time t only. Moreover, material properties are assumed independent of temperature, and it is furthermore assumed that uniform contact is maintained during the entire cooling process. Cremer's experiments indicate that the ribbon, as it cools, tends to have temperature variations from center to its edges, so that the latter may be a significant idealization [22]. Solving equation 2.3 yields

$$\left(\frac{T - T_s}{T_m - T_s}\right) = \exp\left[\frac{H}{\rho C_p \tau} t\right], \tag{2.4}$$

which is given by Incropera and DeWitt [49]. Now it is assumed that once the ribbon temperature cools to T_d, the ribbon detaches, having travelled a distance $x_d = Ut_d$ from the solidifcation zone. Eliminating t_d, equation 2.4 can be rearranged for the sticking distance, x_d. Expressed non-dimensionally as a sticking fraction, Θ_d is

$$\Theta_d \equiv \frac{x_d}{C_w} = A\frac{\tau}{G} \tag{2.5}$$

where the proportionality A depends on other parameters,

$$A \equiv \frac{\rho C_p U G}{H C_w} \ln\left[\frac{T_m - T_s}{T_d - T_s}\right] \tag{2.6}$$

Here, ρ, C_p and C_w are known, while U, G are set and τ is measured during a cast. G and C_w have been introduced to make equation 2.5 dimensionless such that $0 \leq \Theta_d \leq 1$ and $0 \leq \tau/G \leq 1$. Since x_d can vary from detachment immediately upon solidifcation to catastrophic adhesion, Θ_d varies over the full interval. In contrast, $\tau/G \sim 10^{-1}$, typically varying relatively little. The three parameters with greatest uncertainty are T_d, T_s, and H.

Temperature T_d can be estimated by noting that, at detachment, the thermo-elastic stress in the ribbon just equals the peel-off stress needed to break interfacial bonds. The peel-off of the elastic solid is viewed as a fracture energy propagation event in the spirit of Griffith [32]. We use Kendall's model of Griffith propagation to predict the stress needed to break adhesion from a smooth substrate [47]. Persson and Tosatti have extended this model to peel-off from rough substrates [61]. Kendall's model has terms related to elastic, potential and surface energies. The potential term vanishes when the angle of peel-off is zero. Since our ribbon parts from the wheel tangentially, only the elastic and surface energy contributions remain,

$$\frac{\sigma^2 \tau}{2E} = \gamma. \tag{2.7}$$

Eliminating stress σ using equation 2.1 yields an expression for the $T_m - T_d$ and thereby T_d,

$$T_m - T_d = \left(\frac{2\gamma}{E\beta^2 \tau} \right)^{1/2} \tag{2.8}$$

The 'adhesive energy' γ, more properly called fracture energy [47], is a new unknown. Relative to T_d, it is expected to vary weakly with the other parameters. Our strategy is to infer γ from a measurement of T_d and use that value in the model below. By calorimetric measurement (collecting the ribbon in oil and observing the temperature rise), $T_d \sim 782\ K$ ($509°C$) for our typical operating conditions. In this

calculation, it was assumed that ribbon heat loss to the air were negligible, justified by the Biot number $Bi \sim 10^{-5}$, where $Bi \equiv H_{air}\tau/k_{rib}$, $H_{air} \sim 25\ J/m^2 - K - s$ is a typical solid-to-gas heat-transfer coefficient, τ and k_{rib} are the ribbon thickness and thermal conductivity, respectively (see Incropera and DeWitt [49]). To estimate γ, a typical $\tau = 10^{-4}\ m$ and $T_d = 782\ K\ (509°C)$ can be input into equation 2.8, yielding a value of $\gamma \sim 60\ N/m$. Adhesive energy γ has been evaluated for crack propagation speeds up to cm/s in another context by Kendall [47]. Extrapolating that crack propagation speed dependence up to 10 m/s gives values consistent with our inferred value of $\gamma \sim 60\ N/m$. Treating this value as typical, T_d can be estimated as a function of τ by equation 2.8, which will be used in the determination of H using equation 2.5, discussed later.

Before proceeding to estimate T_s, H and to show the utility of equation 2.8, we pause to clarify the approximations involved in the main result equation 2.8. Equation 2.1 assumes that stress builds up as it cools during the secondary quench due to a frustration of the ribbon from undergoing volumetric contraction. That is, the lower ribbon-wheel interface is constrained and cannot deform (i.e. zero-strain). The assumption that contraction is uniformly frustrated − that stress builds up uniformly − is supported by the thinness of the ribbon and the absence of any curl or natural curvature of the ribbon. Equation 2.7 comes from an energy approach which is cleanest when comparing energy differences between two well-characterized states. We compare the state at detachment to a state downstream, once the ribbon has left the wheel, and to the state upstream when the ribbon is just below the melting temperature (beginning of secondary quench). This justifies equating stresses in 2.1 and 2.7. Using the downstream state requires evaluation of the potential energy term in Kendall's energy balance [47]. We observe that, in

all of our experiments, the ribbon was observed to detach tangentially to the wheel and follow a straight trajectory, showing no signs of curling or post-detachment deformation, which justifies neglecting the potential energy since it is proportional to the square of the angle of detachment. Our rationalization of the assumptions leading to equation 2.8 would benefit from more precise observation and a solid mechanics analysis but these are beyond the scope of this note.

Wheel surface temperature T_s increases with time during a cast in the absence of internal cooling, the case for our PFMS machine. Within the wheel, the temperature typically increases by $40-80°C$ for a typical $5-10$ s cast, as measured by embedded thermocouples. T_s could be estimated by extrapolating these in-wheel temperature measurements to the wheel surface using a conduction model. However, for the purposes of this paper, a simpler model will suffice. The temperature at the surface increases per revolution by an amount estimated from a moving point heat-source conduction model on a 3-dimensional slab by Liebermann [51]. For n revolutions,

$$T_s - T_{s,0} = n\frac{\rho\tau WU\Delta h}{2\pi C_w k}. \tag{2.9}$$

The heat-transfer coefficient, H, is found by fitting equations 2.5 - 2.9 with data in the following way. Sticking distance is measured via high-speed image analysis (50 fps). Thickness τ and width W are measured. All other parameters in equations 2.5, 2.6, 2.8, and 2.9 are material properties or set process parameters. Using average ribbon dimensions, average T_d and T_s are calculated using equations 2.8 and 2.9. Then, using equation 2.5 for sticking distance as a function of τ, a one-parameter fit for H is performed. A typical result is illustrated in Figure 3. This fit is done for each of 24 casts, *all exhibiting natural detachment within a quarter of a revolution – none exhibited catastrophic adhesion.* The average H yields an

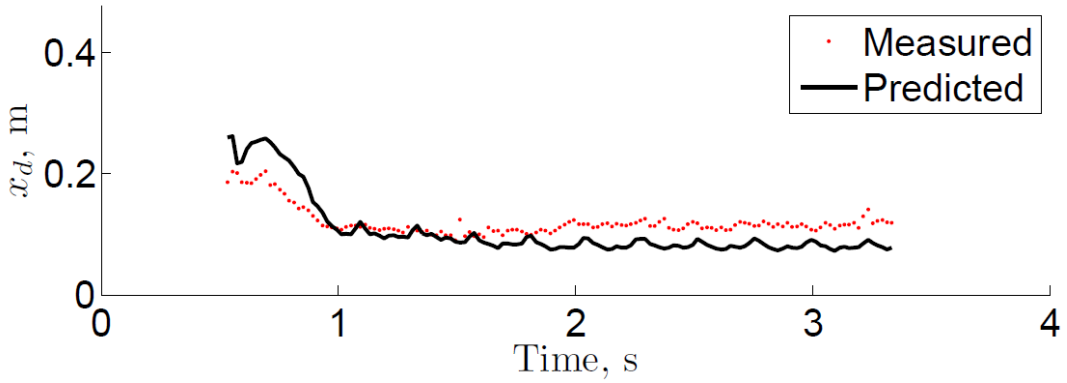

Figure 2.3: Measured and predicted x_d against time, illustrating a fit to a single heat-transfer coefficient to yield $H_1 = 1775\ W/m^2 - K$.

estimate of $H = 1500 \pm 30\%\ W/m^2 - K$. In contrast to the numerous reports of heat-transfer coefficient for the primary quench, we know of no prior reports for a typical H for the secondary quench.

The catastrophic adhesion event was attributed by Liebermann to the increase of wheel surface temperature, T_s. Equations 2.5 and 2.6 substantiate this claim quantitatively. Parameters in these equations are known to be nearly constant except for the parameters T_d, T_s and H which are uncertain. For H to cause a sudden change in x_d, it must decrease by at least an order of magnitude. However, this is unlikely since 1) single-parameter fits yielded H values within $\pm$ 30% of 1500 $W/m^2 - K$, and 2) a sudden decrease in H represents a sudden disruption to the ribbon-wheel heat transfer which would likely also affect the primary quench, yielding suddenly thinner ribbon. This has not been observed. As an example, suppose that the sticking fraction $\Theta_d = 0.18$ for the typical conditions listed in Table 1. Suppose that, during a cast, H decreases by 30% to 1050 $W/m^2 - K$. If all other parameter values remain the same, then $x_d/C_w = 0.25$. Although greater than the original value, this change has not caused a transition to catastrophic sticking.

Changes in T_d and T_s, according to equations 2.5 and 2.6 with all other parameters held at their typical values, affects sticking distance as shown in Figure 2.4. There is a sensitive dependence of x_d on T_d; changes of less than $100°C$ can result in catastrophic adhesion. In our estimate for T_d in equation 2.8, all quantities are material properties except for τ and γ. Since τ is measured and typically remains relatively constant, changes in T_d most likely correspond to changes in γ. On the other hand, the magnitude of γ is a function of the ribbon affinity for the wheel, which might be expected to vary little within a cast. Further investigation is needed to more fully understand whether γ or T_d is more nearly constant during a cast and how changes in substrate surface chemistry and temperature might affect ribbon-wheel affinity. However, based on current evidence, we speculate that T_d is not decreasing within a cast in a way which would cause the transition to catastrophic adhesion.

Temperature T_s is shown in Figure 2.4 to initially have a small effect on x_d; it can increase by several hundred degrees and with x_d increasing only by 10%. However, as T_s approaches T_d, x_d rapidly rises toward infinity since the denominator in the log term in equation 2.6 becomes small. This is consistent with catastrophic sticking. Estimating T_s with equation 2.9 and predicting x_d with equations 2.5 and 2.6, it is found that the transition to catastrophic sticking should occur after 20 revolutions for typical casting conditions, consistent with observation.

We first summarize and then discuss the trends observed by Liebermann. Liebermann observed that *the transition to catastrophic adhesion occurred earlier in the cast* when 1) materials with higher wetting tendencies on the substrate were cast,

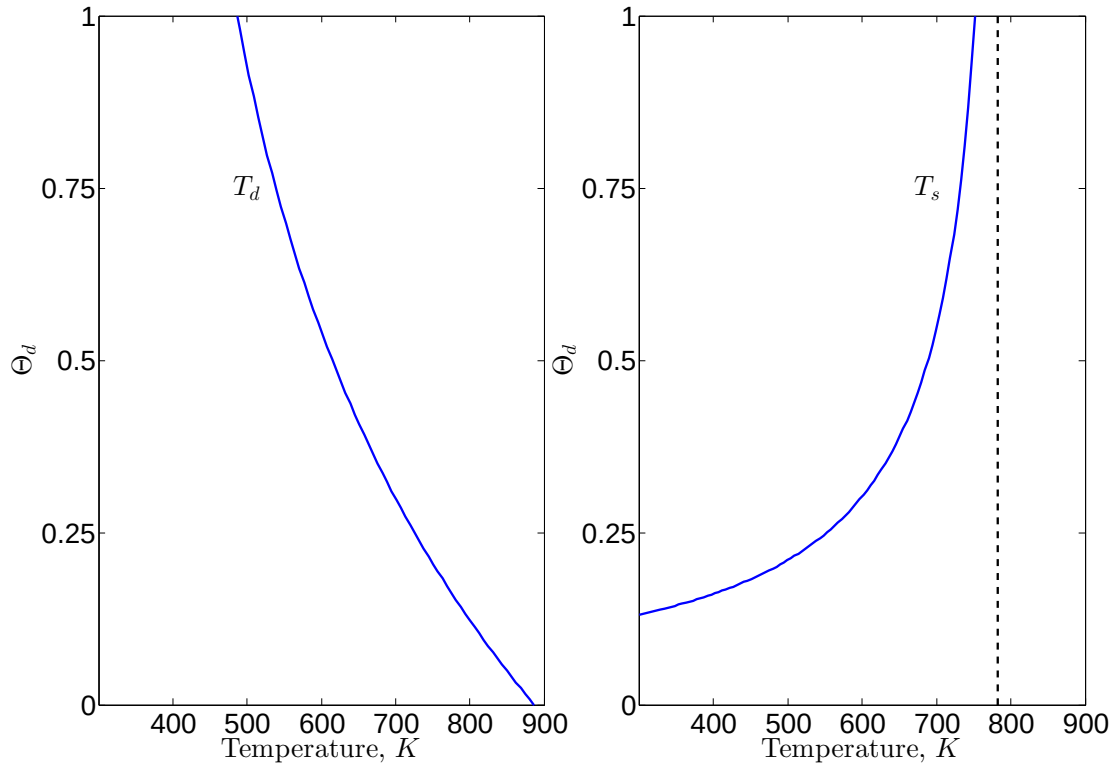

Figure 2.4: Sticking distance Θ_d against a. T_d and b. T_s, according to equation (4), (5) with parameters from Table 1. a. Sticking distance increases sharply with decreasing T_d. b. The typical value $T_d = 782\ K$ for $Al-Si$ casts (dashed). Sticking increase with T_s is gradual for several hundred K, but then sharply trends upward as $T_s \to T_d$.

2) ribbon-wheel affinity was increased, 3) ribbon width was increased, 4) a smaller circumference wheel was used, and 5) substrate velocity was increased. These observations can be explained by our cooling model, equations 2.5 and 2.6.

Observation 1) and 2) are both statements on the affinity for the cast material to the wheel, reflected in the model by γ. The model shows that a two-fold increase in γ yields catastrophic adhesion 10 revolutions earlier, shown in Figure 2.5a). Observation 3) is a statement on the heat input and subsequent temperature rise of the wheel. Wider ribbon results in a greater T_s in equation 2.9, reducing the number of revolutions required for the surface to reach a temperature which yields catastrophic adhesion, shown in Figure 2.5b) for $W = 5\ cm$ and $6\ cm$ ribbon.

Observations 4) and 5) are readily explained using equations 2.5 and 2.6. As seen in equation 2.5, x_d is unaffected by wheel circumference since C_w appears on both sides of the equation. The sticking distance for a fixed set of casting parameters is a constant value, regardless of C_w. Whether this distance is less than or greater than the wheel circumference determines whether the detachment is natural or the adhesion is catastrophic. This dependence is captured by putting $x_d/C_w = 1$ in equation 2.5. Increasing wheel speed also increases sticking distance. A certain cooling is required for detachment, and by increasing the wheel speed, x_d needs to be greater to achieve the requisite cooling. For both smaller C_w and larger U, fewer revolutions are required to transition to catastrophic adhesion, Figure 2.6.

We now add our experimental observations. By its nature, *catastrophic sticking is to be avoided*, so we only have only seven unintentional events to report. Furthermore, even with high-speed video, it is difficult to capture $x_d(t)$ when it

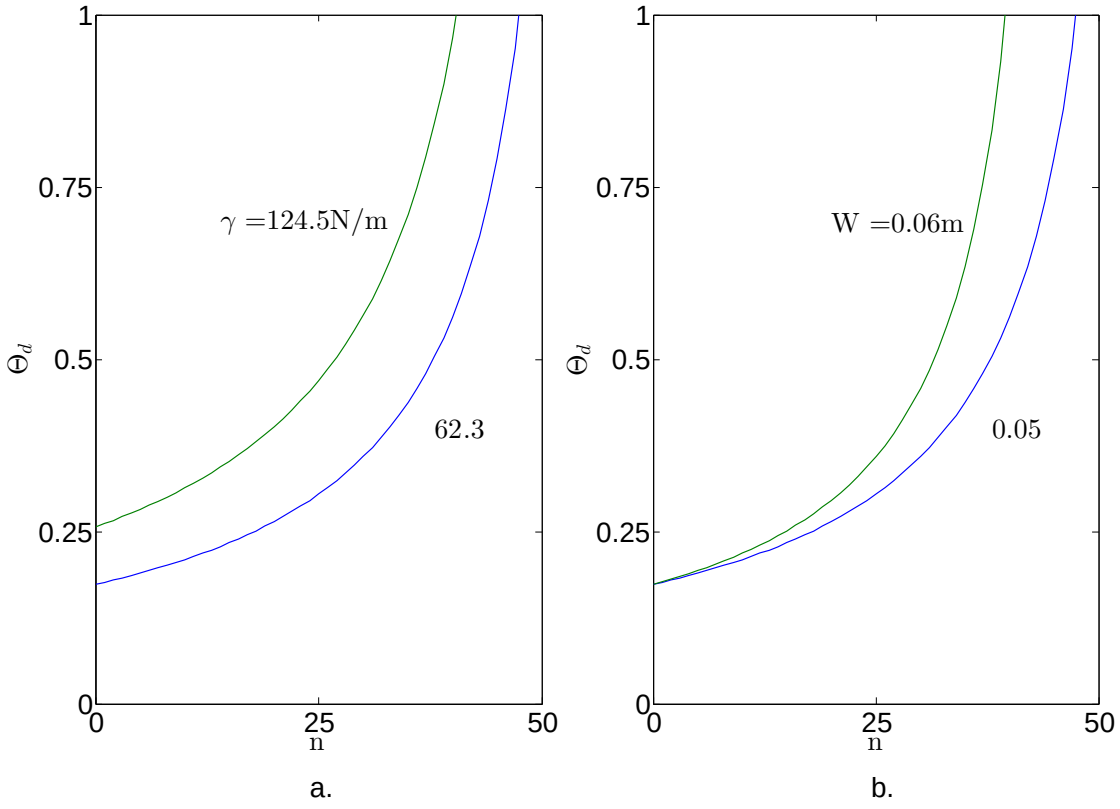

Figure 2.5: Sticking distance Θ_d against number of revolutions n as influenced by a. ribbon-wheel affinity γ, and b. by width W, according to equations (4), (5), and (7). Increasing ribbon-wheel affinity γ lowers T_d, requiring additional time for ribbon to cool sufficiently to detach (increasing Θ_d). Increasing ribbon width W increases the heat-loading to the wheel, causing T_s to rise faster, causing catastrophic adhesion earlier in cast.

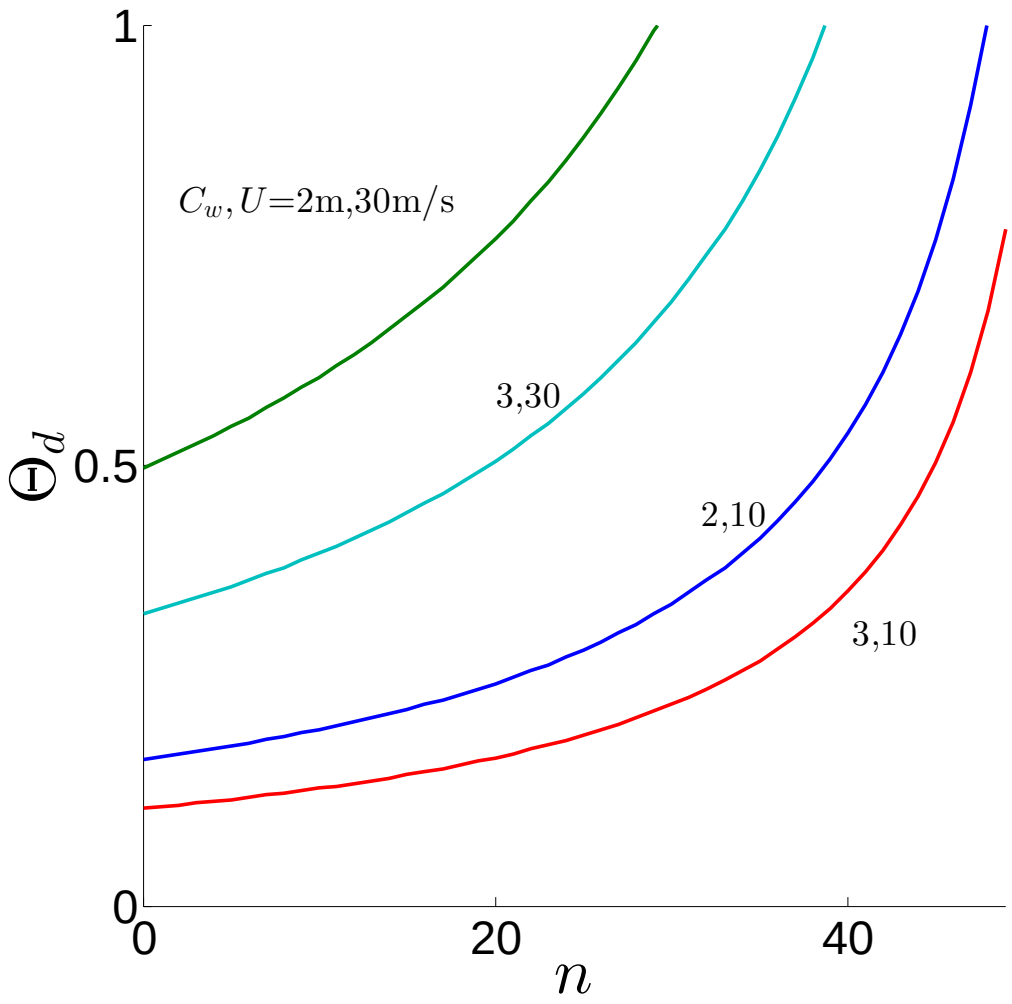

Figure 2.6: Sticking distance Θ_d against revolutions n as influenced by wheel circumference C_w and wheel speed U. Decreasing wheel circumference or increasing wheel speed causes the sticking distance to be closer to the solidification region. Catastrophic sticking occurs after fewer revolutions.

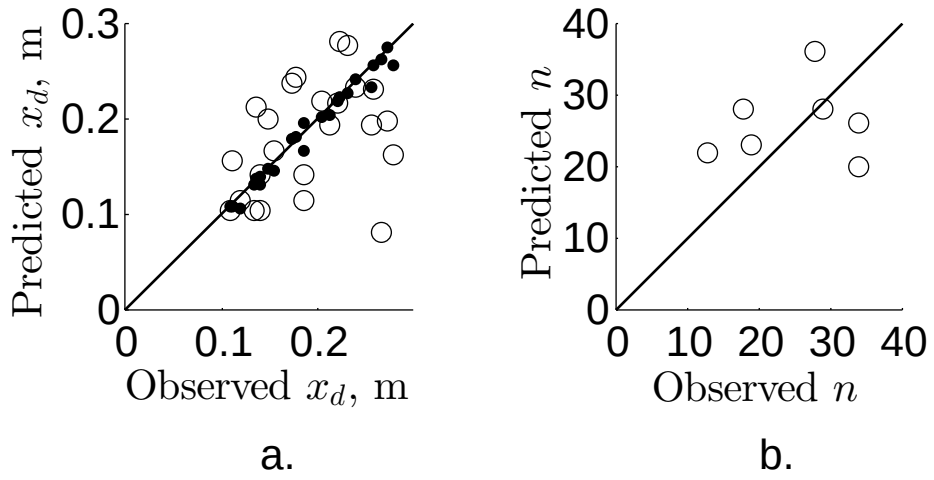

Figure 2.7: a. Cast-average sticking distance x_d, predicted against observed, b. number of revolutions for transition to catastrophic sticking n, predicted versus observed.

increases rapidly toward C_w since a wheel with $C_w = 2\ m$ requires a large field of view, much of which is obstructed by our casting machine's framework. For these reasons, we first empirically determine H for casts that remain in the field of view, $\Theta_d < 0.5$, and for which x_d varies slowly in time. These are natural detachment events. We then use an average H, from these experiments, to predict catastrophic adhesion. As the metric for catastrophic adhesion, we will use the number of wheel revolutions passed when catastrophic adhesion happens.

As described above and illustrated in Figure 3, $H_i, i = 1, ...24$, are obtained by best-fit to x_d using hundreds of images taken throughout a single cast, for each of twenty-four casts that exhibits natural detachment. Arithmetic means of observed x_d and τ are computed. Then, using the average τ, an average T_d and T_s were calculated from equations 2.8 and 2.9, respectively. Other known parameters

in equation 2.6 are input and a least squares best-fit to determine H_i is performed. These H_i are used to predict x_d, shown as solid dots in a parity plot of predicted versus observed x_d, Figure 7(a). Dots do not fall precisely on the line, giving a sense of the goodness of our best-fit. We then average to obtain an ensemble-averaged $H = \frac{1}{24}\sum_{i=1}^{24} H_i = 1500\ W/m^2 - K$. Figure 7(a), open circles, shows the same observed x_d against a predicted x_d now obtained using the averaged H. The scatter here represents the scatter of the H_i values around mean H. Having 'trained' the model, we can finally predict catastrophic sticking.

For an uncooled wheel, catastrophic adhesion will always occur if the initial charge of metal is large enough. However, by its very nature as a sudden up-turn in surface temperature T_s, catastrophic adhesion is most challenging to predict. Any errors in the inputs to equation 2.5 accumulate with every revolution. The observations against predictions for seven catastrophic adhesion events are shown as open circles in Figure 2.7b). Some correlation is apparent but there is also considerable scatter. Because there is both under- and over-prediction of observation, contributing errors are apparently non-systematic. Among the variety of effects that may contribute, the surface roughness of the wheel was not well controlled. In fact, it was purposefully altered in several of the casts, likely changing the adhesion strength and T_d. In any case, further study would be required to discern the effects that contribute most to the scatter.

The predictions shown in Figure 2.7b) are semi-empirical in that the measured ribbon thickness τ is put into equation 2.5 and 2.8 to predict x_d. This is not necessary in view of the decoupling to first order of heat transfer from fluid flow in PFMS [15]. Ribbon thickness has been predicted based on imposed pressure

difference and gap variation by a variety of authors [40] [76] and these predictions could have been incorporated into the prediction of sticking distance. However, that would have invited a discussion of the errors involved in that prediction which would have detracted from the main message of this paper. The focus here is on heat-transfer and related aspects of sticking. Hence, for clarity in presentation, we use semi-empirical prediction.

In summary:

1. Ribbon detaches naturally from wheel by thermo-elastic stress build-up upon cooling to a temperature T_d.
2. Detachment temperature T_d can alternatively be characterized by an adhesive/fracture energy γ, inferred to be $\gamma \approx 60 N/m$ for AlSi against CuBe.
3. Transition from natural to catastrophic adhesion is caused by substrate temperature rise. Equation 2.6 shows that, as $T_s \rightarrow T_d$, the pole is initially shielded by the logarithm but eventually dominates.
4. Ribbon cooling and substrate heatup model predicts sticking distance and transition to catastrophic adhesion, making quantitative the trends described by [51].

Adhesion upon solidification involves contacting mechanics and heat transfer while natural detachment involves cooling, stress relaxation in an event that can be likened to crack propagation. Both are complicated events. In this note we have sketched what parameters these events depend on by introducing a model that includes parting mechanics. The model will need further testing and likely refinement.

Acknowledgements

The authors thank Brian Carroll and Brenton Cox for their work in capturing/analysing high-speed video and in interpretting the data. We thank Thomas Ober and Cormac Byrne for starting this project. We also thank Chris Jakobson and Michael Davis for their experimental contributions to this project and also Eric Theisen (Metglas) and Professor C.Y. Hui (Cornell University) for useful discussions. Experiments were supported by NSF Grant No. CMMI-0423791 and CMMI-0726813. We thank ALCOA for supplying materials for these experients.

CHAPTER 3

SUBSTRATE HEATING IN THE PLANAR-FLOW MELT SPINNING OF METALS. *

Abstract

Planar-flow spin casting is a rapid solidification process used in the manufacture of thin, metallic ribbons. Liquid metal is solidified against a cool, rotating wheel which absorbs the super- and latent heat of the metal. In the absence of internal cooling, the wheel temperature rises. It has been observed experimentally that the temperature rise differs at different radial positions within the wheel. A conduction model is presented which predicts the temperature as a function of position in the wheel and time in the cast. Simplifications to the full conduction model are also presented, with heuristic guidelines to when they are valid. Finally the model is applied semi-empircally using ribbon dimensions and casting parameters from an experiment to predict temperature and compare to experimental temperatures.

3.1 Introduction

Planar-flow melt spinning (PFMS) is a single-stage, continuous process for the cooling and solidification of liquid metal into thin, metallic ribbons [59]. Liquid metal is forced from a heated crucible through a nozzle onto a rotating, metallic wheel substrate which acts as a heat sink, absorbing super- and latent heat of the metal (figure 3.1a). PFMS is distinguished from other spin casting processes by

*Submitted to ASME Journal of Thermal Science and Engineering Applications, coauthor PH Steen, Oct. 2013

the close proximity of the nozzle to the moving substrate, a gap into which liquid metal is forced. Within the gap, a molten metal puddle forms, held in place by surface tension acting at its liquid-air interface. The metal is solidified and spun off as product in the shape of a thin sheet, foil or ribbon at rates of meters per second. The heat sink substrate may or may not be actively cooled. In our study, there is no active cooling. For our goal of disentangling the various contributions to substrate heat-up, the transient temperature rise within the wheel during processing is an advantage.

PFMS received initial attention during the late 1970s and 1980s as a favored

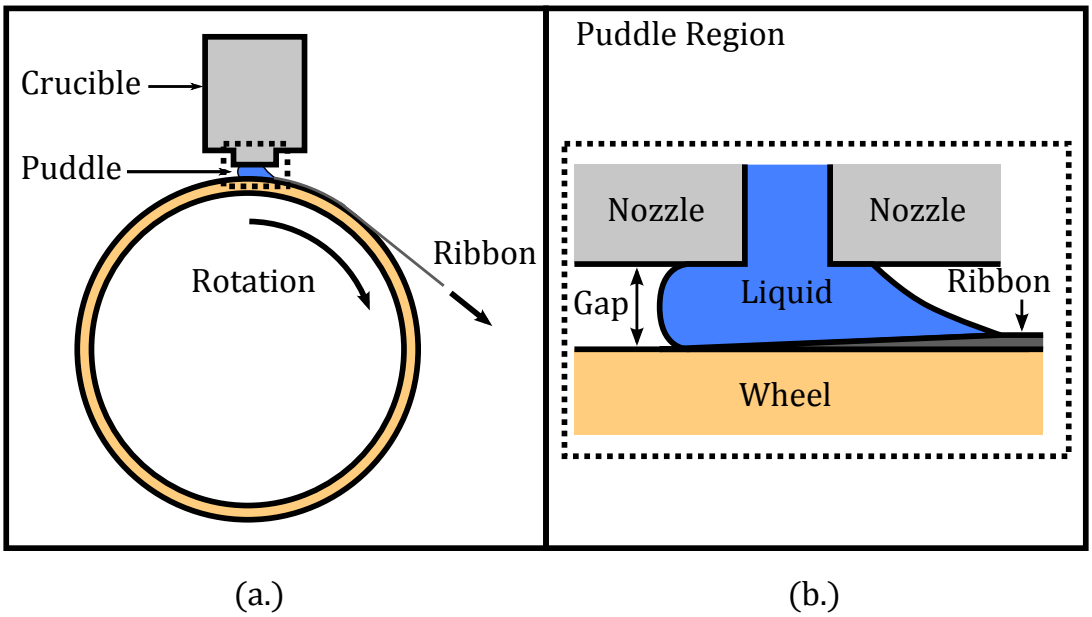

Figure 3.1: Schematic of PFMS process and puddle region.

technique to continuously cast metallic glasses [59]. Renewed interest worldwide has come from the growing importance of metallic glasses in a variety of induction-based electromagnetic applications. Hasegawa (2004) and Hasegawa and Azuma (2009) discuss energy-conversion applications of these materials [36][37]. Li, et al. report pilot scale (3-ton crucible) industrial implementation of PFMS to make

metallic glasses [50]. Herzer discusses applications to electro-acoustic surveillance devices[38]. Over the past decade, a variant of PFMS has been developed to continuously cast silicon substrates for solar-cells [35]. More recently, PFMS has enabled so-called 'nanosteels,' stainless steel foils with nanocrystalline structures that yield ultra-high strengths despite the thinness of a foil [7][6]. In summary, a variety of alloys and applications already have benefited from the rapid solidification and high productivity of PFMS. PFMS is a re-emerging fabrication technique.

In these applications, the thermal history experienced by the product during PFMS processing determines its final nanostructure and its ultimate material properties. And the thermal history experienced by the product is largely determined by the thermal history of the substrate. This fact motivates our study and sets its scope.

Commercializations using PFMS notwithstanding, the process has seen limited implementation largely because its difficulty to control. Our goal is to place the process on a firm scientific basis. To that end, a major challenge is to account for the mechanical coupling between substrate expansion and final ribbon thickness, as outlined next.

In PFMS, cooling rates can be very high, up to 10^8 Kelvin per second under ideal conditions [46], sufficient to yield amorphous and nearly amorphous (nanocrystalline) structures for many alloy systems. Wheels used in melt-spinning may have an internal cooling system or may be uncooled. In the absence of internal cooling, heat is continually transferred to the wheel during a cast causing its temperature to rise. As the temperature of the wheel rises, it tends to expand outward, reducing the size of the gap, discussed by Theisen, et al. [76]. PFMS is a feed-limited pro-

cess which means that the thickness is determined by the delivery of molten metal to the solidification front. The resistance to metal flow depends on the gap size, which has been shown to greatly influences the final ribbon thickness [76]. As the gap decreases, the ribbon thickness is reduced. As ribbon thickness decreases, the amount of heat transferred to the wheel decreases, completing a feedback coupling between the heat-transfer and fluid dynamics of the process. Whether or not the wheel is actively cooled, a better understanding of the wheel heating is essential to fuller understanding of the overall process. In contrast to fluid flow, there are relatively few studies of substrate heating. For the un-cooled wheel, thermal effects are accentuated, easing the challenge of observation.

The specific goals of this study are to:

1. identify conditions for which conduction within the wheel may be accurately accounted for by reduced-order dimensional models: one- or two-dimensional;
2. derive a reduced order model which adequately captures the time trace of the temperature measurements, available from within the wheel;
3. predict the time trace of wheel surface temperature, which is difficult to directly measure.

A number of authors have studied heat-transfer in various melt-spinning processes. Most commonly, authors have applied various heat-transfer models of the puddle and substrate to examine the rate of melt/ribbon cooling and estimate puddle-wheel heat-transfer coefficients (HTC). Carpenter and Steen (1990) use a local heat-balance and, in the limit of an infinite puddle, derive a criterion for determining the minimum HTC in PFMS which they estimate to be $3 \times 10^4\ W/m^2 - K$ for

aluminum cast on a copper wheel [14]. Takeshita and Shingu (1983) consider consider heat-transfer in crystal growth on a stationary substrate. Using equations of conduction and crystal growth kinetics they estimate the HTC to be on the order of $10^5\ W/m^2-K$ [73]. In a later publication (1986), they apply a simplified version of this model to chill-block melt-spinning and report HTC $\sim 10^5-10^6\ W/m^2-K$[75].

Wang and Matthys (1991) use a numerical volume integral scheme to model heat-transfer in the melt and substrate as a function of material properties and melt superheat. Assuming a HTC of $10^6\ W/m^2-K$, they estimate $10^6-10^7\ K/s$ cooling rates in their simulation. They also predict a substrate surface temperature increase by several hundred Kelvin for various materials cast on a copper wheel [82], a result consistent with our findings. Byrne et al. (2007) used a focussed laser to alter the local cooling rate of the ribbon and create localized thickness depressions on the product. The laser could be alternatively focussed on the melt puddle or diverted to the wheel. They inferred cooling rates by looking at the ribbon microstructure and compared to typical cooling rates of $10^4\ K/s$, which they derived from a control volume approximation [11]. A similar substrate temperature rise was reported by Liu, et al. (2009), who present a 2-dimensional numerical model of fluid flow and heat-transfer at the cast onset [54]. Kukura and Steen use a 1-dimensional finite difference scheme to model conduction into the wheel (perpendicular to the cast direction) in PFMS. They estimate $H \sim 10^5\ W/m^2-K$ by fitting the model to embedded thermocouple data from within the wheel. Of particular interest is the good quality fit to the data early in the cast which diminishes as the cast procedes [48]. Our analysis will show that this is caused by contributions of axial conduction of heat toward the edges of the wheel, neglected in the 1-dimensional model. Li and Thomas use a numerical model of heat-transfer

and solidification in melt-spinning to estimate flux rates and ribbon thickness as a function of time. By comparing to their data for an internally cooled wheel, they estimate $H \sim 10^3 - 10^4\ W/m^2 - K$, the lowest literature values reported.

Several papers by Tkatch and others examine heat-transfer of melt spun FeNiPB alloys. Tkatch, et al. (1997) used a Newtonian type cooling model to compare with data from thermocouples which protrude through the wheel to the surface. They found cooling rates on the order of $10^6\ K/s$ and $H \sim 10^4 - 10^5\ W/m^2 - K$. They found rapid increases of the wheel surface temperature as high as 1400 K which subsequently rapidly decayed[77]. Tkatch, et al. (2002) looked experimentally at the effect of wheel speed, gas ejection pressure, and melt temperature on cooling rates. They report cooling rates of $10^4 - 10^6\ K/s$, which were found to increase with wheel speed and ejection pressure, but decrease as superheat grows. They also report improved ribbon-wheel contact with increasing gas pressure, giving rise to increased cooling rates and ribbon thickness [79]. Tkatch, et al. (2009) also photographically examine the structure of FeNiPB glasses. They found evidence of air pockets on the wheel-side of the ribbon on the order of 1 μm for 30 μm ribbon. The density of these air pockets decreased with wheel speed, but their dimensions were constant. Cooling rates of $10^6\ K/s$ and $H \sim 10^5\ W/m^2 - K$ were estimated from temperature versus time plots [78].

Finally, in a recent publication by Karpe, et al. (2011), a numerical heat-transfer model was used to estimate temperature profiles for *internally cooled* wheels. Although their purpose was to derive design criteria for internal wheel cooling systems, they report wheel temperature profiles that resemble those presented below [45].

3.2 Experiment overview and data collection

In our study, a 30 cm diameter Cu-Be wheel was used to cast 7% $Si-Al$ ribbon. The wheel was a cylindrical rim, with wall thickness 1.3 cm. Raw metal contained in a graphite crucible was heated to 987 K (100 K superheat) via an induction heater. Then, liquid metal was forced from the crucible by an applied Argon over-pressure through a nozzle 1 mm from the wheel surface onto the wheel rotating at $200-325$ RPM, corresponding to linear speeds of $7-12$ m/s. Typically, 0.5 kg of material is cast into ribbon of width 5 cm and thickness $75-250$ μm in less than 10 s. Material properties and cast parameters for our typical casting operations are given in Table 1, as well as their symbols to be used in the following sections.

The casting apparatus has been outfitted to monitor i) temperatures at two different positions within the spinning wheel substrate, along with ii) the wheel speed, iii) the gap distance and iv) the crucible pressure. After completion of the cast, v) the thickness of the product is measured as it depends on position along the ribbon.

Threaded holes of various depths drilled into the inner surface of the annular wheel rim house embedded K-type thermocouples (TC). Data presented here comes from TC's embedded at nominal depths of 2 and 9 mm below the outer wheel surface register the temperature changes of the wheel during a cast, shown for a typical cast in Figure 3.2. Perfect contact between a TC and the wheel is difficult to

Table 3.1: Properties and Parameters

Property	**Symbol**	**Range**	**Typical Value**	**Units**
Casting Parameters				
Wheel speed	U	$5-12$	10	m/s
Gap	G	$0.5-2$	1	mm
Crucible pressure	ΔP		2500	Pa
Ribbon				
Thickness	τ	$50-250$	100	μm
Width	W_r		0.05	m
Liquid density	ρ_ℓ		2300	kg/m^3
Solid density	ρ_r		2700	kg/m^3
Liquid heat capacity	$C_{p,\ell}$		1030	$J/kg-K$
Solid heat capacity	$C_{p,r}$		938	$J/kg-K$
Latent + $100K$ Super heat	h_s		4.9×10^5	J/kg
Wheel				
Wall thickness	ξ		0.013	m
Circumference	C		1.9	m
Width	W		0.13	m
Density	ρ		8960	kg/m^3
Heat capacity	C_p		385	$J/kg-K$
Thermal conductivity	k		200	$J/m-K-s$
Thermal diffusivity	α		5.6×10^{-5}	m^2/s
Others				
Half puddle width	z_s		0.025	m
Puddle length	x_s	$1-2$	1	cm
Puddle time	t_s	$1-2\times10^{-3}$	1×10^{-3}	s

achieve. To improve this contact, the tip of the TC is coated with thermal grease. Temperature data are collected at 100 Hz. Note that, in principle, the temperature at the outer wheel surface could be measured with an IR thermal sensor but, at wheel speeds of 10 m/s, high sampling rates are needed for reasonable spatial resolution. In addition, access to the wheel surface close to the puddle is limited. These circumstances make IR sensing of temperatures impractical for our apparatus. Modeling will be tested against TC traces.

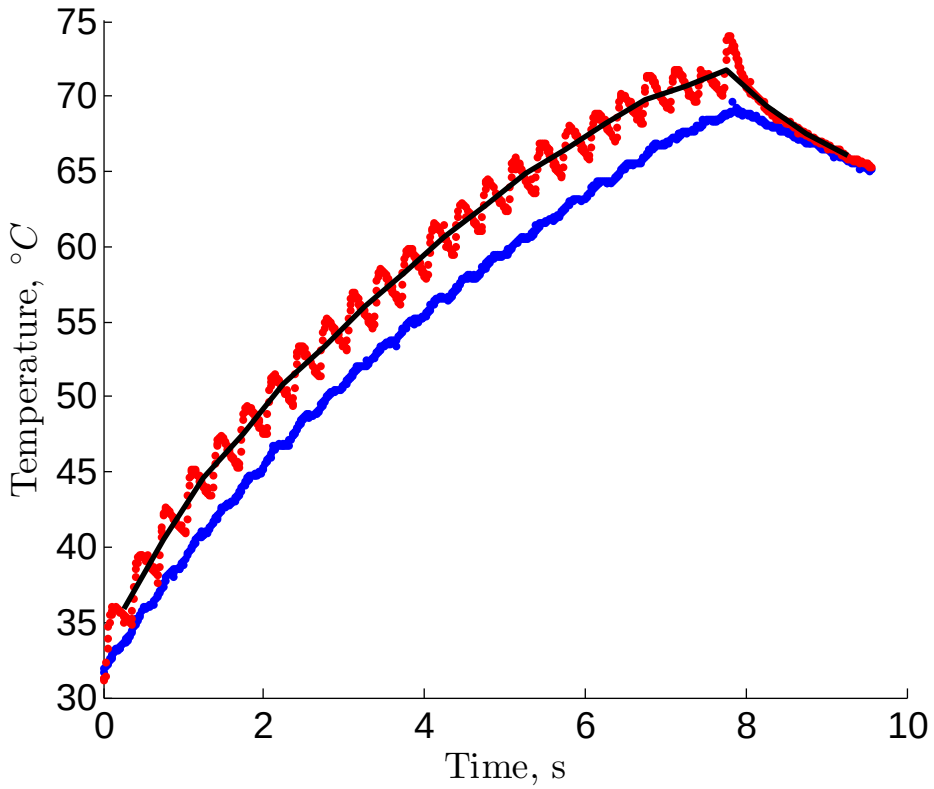

Figure 3.2: Temperature versus time at 2 mm and 9 mm from upper wheel surface, measured by thermocouples embedded within wheel. Black line drawn to highlight curvature of the overall temperature rise.

Several features of the TC traces illustrated in Figure 3.2 are worth noting: 1) temperatures at both depths are observed to increase during a cast, 2) the TC closer

to the wheel surface (red circles, online) exhibits periodic spikes, corresponding to when TC passed under the puddle in each revolution, 3) the TC further from the surface (blue circles, online) exhibits a smooth, nearly monotonic increase in temperature, and 4) the overall rise of the TC traces (black solid line) has a concave-down shape. The apparent thermal gradients indicate that conduction in the depth direction is significant, despite the thinness of the wheel wall thickness. We seek a model which captures these features.

The modeling challenge arises from the numerous competing conduction time- and length-scales. Refer to Figure 3.4 and Table 3. The wheel substrate sees the heat loading of molten metal once per circumference, the puddle revisit time, C/U. The duration of the heat loading is the puddle exposure time, t_s. Conduction of the applied heat through the substrate occurs in three dimensions with boundary conditions felt at different times, depending on the substrate geometry. Three lengths characterize the rim geometry: circumference C, thickness ξ, and width $2W$. Two lengths characterize the puddle extent: length x_s and width $2z_s$. These five lengths yield five conduction time-scales which together with the source loading times yield a total of seven time-scales. The task is to sort out which of these time-scales is dominant when, for how long, and how the various conduction regimes correspond to limiting solutions of the full conduction problem.

Wheel speed and gap were set prior to the cast and measured throughout. Ribbon is cut into segments post-cast to determine the thickness. Gap, G, and thickness, τ are plotted versus time in Figures 3.3), respectively. The gap distance was observed to decrease overall, but also exhibits oscillations. The oscillation is due to wheel out-of-roundness from machining imperfections, resulting in local

high and low spots that persist throughout the cast. The overall gap decrease is caused by wheel expansion as its temperature rises. The effect of the decreasing gap can be seen in the thickness plot, which also exhibits periodicity and overall decrease. Theisen, et al. (2010) use a simple model of wheel heat-up in which heat is assumed instantaneously spread throughout the wheel volume, combined with a uniform volumetric expansion model to derive a semi-empirical predictor of gap change throughout a cast [76]. The validity of this approach will be discussed.

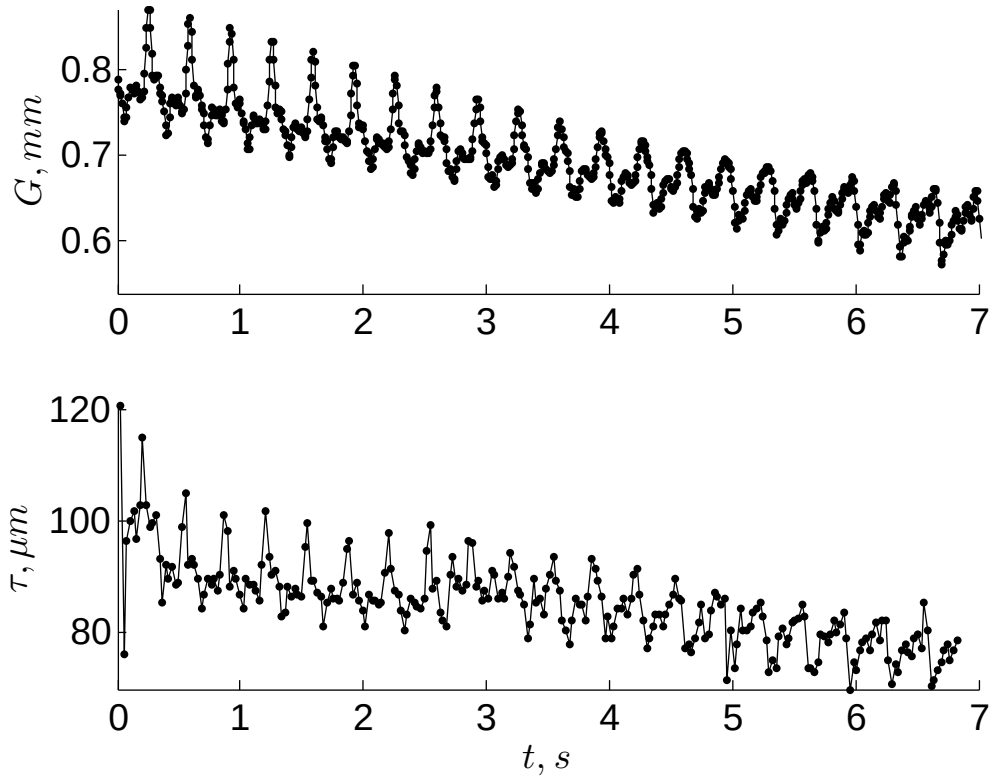

Figure 3.3: Gap (upper) and thickness (lower) data versus time within a cast. Both decrease overall in time and have some periodicity per revolution, corresponding to wheel out-of-roundness. Solid line in thickness plot added to guide the eye.

3.3 Wheel Heating

Our purpose in this section is to derive a model of heat conduction within the wheel. We begin by presenting governing equations and boundary conditions for our model. Then, we present the solution to these equations and various simplifications, summarized in Table 4. Finally, we derive several heuristic rules from our exact solutions as to when each approximation may be valid.

3.3.1 Governing Equation

To understand the spatial and temporal variations within the wheel, a control volume of a 3-dimensional slab of the wheel, with thickness ξ and half-wheel width W, shown in Figure 3.4 will be selected and followed. Suppose that, contained within this slab, there is is a thermocouple with position (x, y, z). The following language will be used to refer to these coordinates: the x-direction is called 'circumferential,' and is in the direction of rotation of the wheel; the y-direction is called 'radial,' and is in the direction pointed outward from the center of the cylindrical wheel; the z-direction is called 'axial,' and is parallel to the axis of rotation.

In the wheel-frame point-of-view, conduction within the slab is governed by the 3-dimensional heat equation. A natural coordinate choice would be cylindrical, however, it can be shown that the small ratio of wheel thickness to radius, $\xi/R_w \sim 0.04$, reduces the heat equation to rectangular coordinates with $O(\xi/R_w)$ corrections. Ignoring these, the governing equation is

$$T^{(t)} = \alpha(T^{(xx)} + T^{(yy)} + T^{(zz)}). \tag{3.1}$$

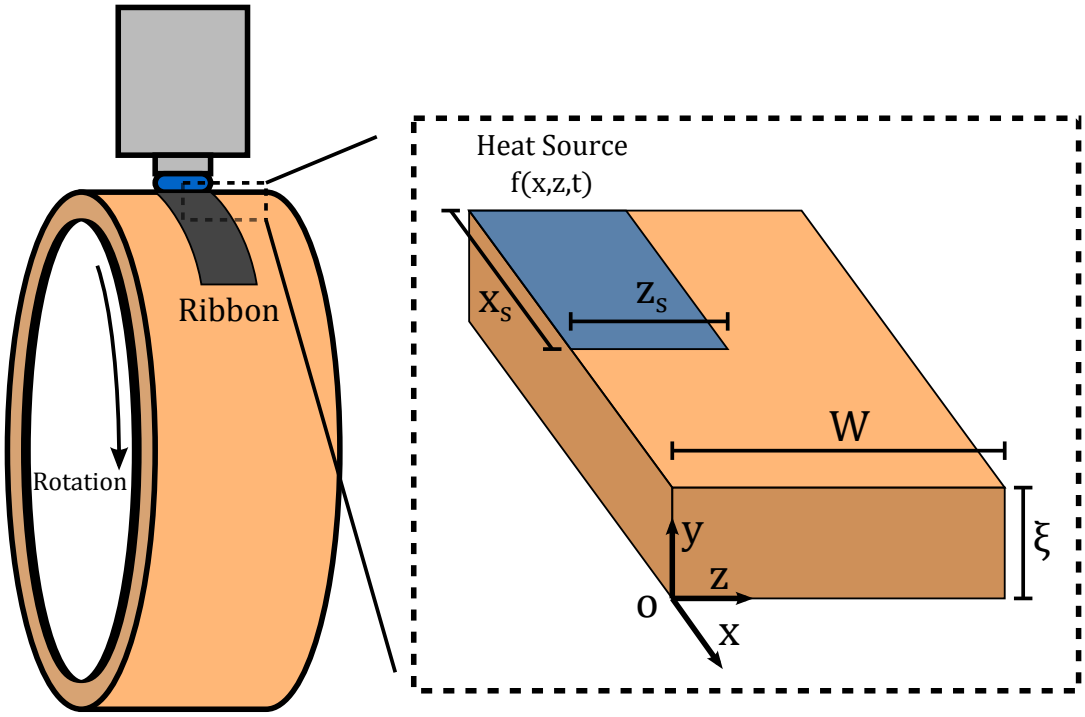

Figure 3.4: 3-dimensional control volume with width W, length L, and thickness τ. Time dependent heat source with length x_s and width z_s acts on upper surface. Direction definitions: x or 'circumferential' in rotation direction, y or 'radial' beginning at inner wheel surface and moving radially outward, and z or 'axial' beginning at wheel center and moving parallel to the axis of rotation.

Note that the superscript with parenthesis notation will always be used to denote partial derivatives to distinguish from other sub- and superscripts. Various simplifications to equation 3.1 will be considered, but first, we make an argument to ignore the circumferential direction entirely. The slab will experience a heating phase as it passes under the puddle and then a zero-heating (or cooling) phase for the remainder of each wheel revolution. The circumferential position of the puddle heat-source will appear to move relative to our slab with wheel speed, U. Its position is $x = -Ut$. Scaling equation 3.1 according to

$$t \sim \xi^2/\alpha, \qquad y \sim \xi, \qquad z \sim W, \qquad x \sim Ut = U\xi^2/\alpha, \qquad a = \xi/W$$

reduces it to

$$T^{(t)} = (1/Pe)^2 T^{(xx)} + T^{(yy)} + aT^{(zz)} \tag{3.2}$$

where a is the wheel thickness-to-width aspect ratio and $Pe \equiv U\xi/\alpha = O(10^3)$. Large Peclet number estabilishes that heat transfer by conduction is much smaller than by advection by translation. Thus, by ignoring the circumferential direction, we incurs $O(10^-6)$ errors. The 3-dimensional slab is reduced to a 2-dimensional one, shown in Figure 3.5a. *In all cases that follow, this simplification is invoked:* $T \neq T(x)$. Physically, this can be interpretted by examining two time scales: a translation time $C/U \sim 0.2\ s$ and a conduction time scale $\xi^2/\alpha \sim 3\ s$. Thus, even for the chosen length scale ξ, which is small relative to the circumference C, conduction is an order of magnitude slower than translation. If two adjacent control volumes were chosen, both would experience heating from the puddle before significant conduction ocurred between them.

3.3.2 Boundary Conditions

Equation 3.2 contains two second-order spatial derivatives and one first-order temporal derivative, requiring four boundary conditions and one initial condition for the initial-boundary-value problem (IBVP) to be well posed. First, it is assumed that the wheel is intially at constant temperature $T(t = 0) = T_o$.

The only source of heat in the problem comes from ribbon quenching, occuring at the wheel surface, $y = 1$. Most of the heating occurs directly underneath

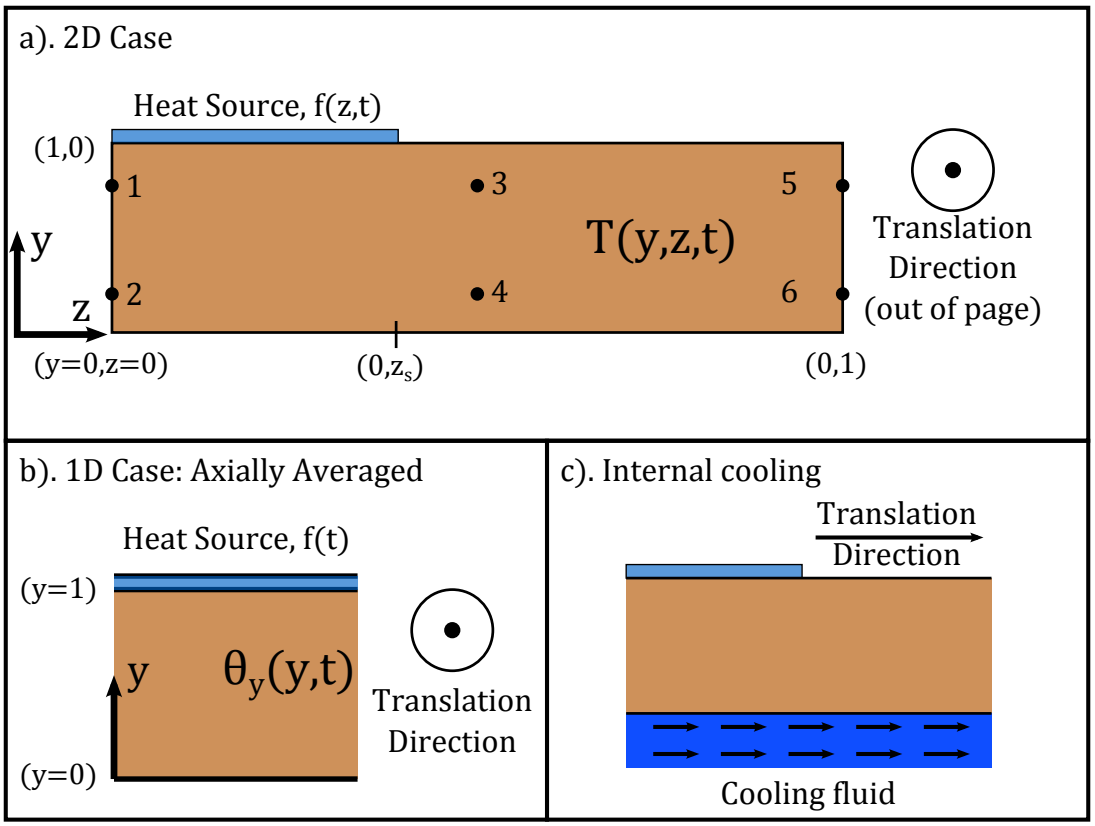

Figure 3.5: Simplified 2- and 1-dimensional views of the control volume, neglecting circumferential direction. Numbers 1-6 represent thermocouple positions which will be referred to repeatedly.

the puddle, although some heat is transferred post-solidification before the ribbon breaks contact with the wheel. For a ribbon with thickness τ and puddle width $2z_s$, the mass rate of ribbon formation in the puddle is $2\rho_r \tau z_s U$. For solidification to occur, the ribbon must transfer its super- and latent heat to the wheel. The rate of energy transfer to the wheel is $2\rho_r z_s U h_s$, letting h_s represent the total energy of solidification.

To specify flux boundary conditions for the IBVP, the area through which the source is delivering energy is needed. In our case, these dimensions are the puddle

length, x_s, and width, $2z_s$. Hence,

$$q_s = \frac{\rho_r \tau U h_s}{x_s} \tag{3.3}$$

For typical casting conditions $q_s \sim 10^8\ W/m^2$.

As indicated in Figure 3.5a, the puddle does not extend to W in the axial direction and so a boundary condition for $z > z_s$ is needed. This area of the wheel sees only the surrounding air, so we estimate the wheel-to-air heat flux. A typical heat-transfer coefficient for air flowing past a metallic surface is $H_{air} = 50 W/m^2 - K$. Supposing that, at a maximum, the surface of the wheel approaches the puddle-melt temperature, 887 K, and that the ambient air is 300 K, a maximum wheel-to-air heat flux is esimated to be

$$q_{air} = H_{air}(T_{surface} - T_{air}) \approx 3 \times 10^4\ W/m^2 \tag{3.4}$$

By this estimate, air losses represent 0.03% of the heat-input to the wheel, and will be ignored. To summarize, the chosen control volume experiences heating at $y = 1$ in the region $0 \leq z \leq z_s$ while it is underneath the puddle. The region $z > z_s$ at $y = 1$ and the region $0 \leq z \leq z_s$ outside of the puddle are assumed insulated. Similarly, the boundary at $z = 1$ is also surrounded by air, and is assumed insulated. A zero-flux boundary at $z = 0$ is also imposed, assuming symmetry about the midplane of the wheel. Boundary and initial conditions are summarized in Table 2, where $q(t)$ abruptly changes depending on the position.

During each revolution, the control volume will experience a heating and a cooling phase. The heating condition at the surface thus has axial *and* temporal dependence. Furthermore, the puddle conditions are known to vary throughout a cast; the q during the first and tenth revolution may be numerically different, for example. Additionally, the ribbon may adhere to the wheel while it cools after leaving

Initial and boundary conditions for 2-dimensional solution		
Initial temperature	$t = 0$	$T = T_o$
Inner edge	$z = 0$	$T^{(z)} = 0$
Outer edge (OE)	$z = 1$	$T^{(z)} = 0$
Lower surface (LS)	$y = 0$	$T^{(y)} = 0$
Upper surface	$y = 1$	$kT^{(y)} = \begin{cases} q(t) & z \le z_s \\ 0 & z > z_s \end{cases}$

Table 3.2: Summary of initial and boundary conditions

the puddle, introducing a second heating phase for the wheel per revolution. To allow for these, $q(t)$ is given the time-dependent form

$$q(t) \equiv \left\{ \begin{array}{ll} q_1 & t_1 \le t < t_2 \\ q_2 & t_2 \le t < t_3 \\ \vdots & \\ q_p & t_p \le t < t_{p+1} \end{array} \right\} \tag{3.5}$$

where $q_j = const$ during each time interval. As an example, suppose the cast begins at $t_1 = 0$. Beginning at the puddle, the CV will experience heating q_1 for one puddle time, t_s and q_1 will be applied from $0 \le t \le t_2 = t_s$. Then, after leaving the puddle, an insulated condition, $q_2 = 0$, is applied for the remainer of the revolution, $t_2 = t_s \le t \le t_3 = t_{rev}$. This is repeated for n-revolutions with q_j possibly varying. Here $t_s = x_s/U$ and $t_{rev} = (C_w - x_s)/U$.

One final quantity will be useful in the analysis to follow. Suppose that the time-dependent flux is smeared in time to represent a constant, effective flux q_e into the wheel

$$q_e \equiv \frac{1}{t_p - t_1} \int_{t_1}^{t_p} q dt = \frac{1}{t_p - t_1} \sum_{j=1}^{p} q_j (t_{j+1} - tj). \tag{3.6}$$

Model	**Definition**	**Governing Eq.**	**Top Surface BC**
Full 2D	$u(y,z,t)$	$u^{(t)} = u^{(yy)} + au^{(zz)}$	$u^{(y)} = f(z,t)$
Axial-averaged 1D	$\theta_y(y,t) \equiv \int_0^{z_s} u dz$	$\theta_y^{(t)} = \theta_y^{(yy)}$	$\theta_y^{(y)} = \int_0^{z_s} f(z,t) dz$
Spatial-averaged 0D	$\bar{\theta}(t) \equiv \int_0^1 \int_0^{z_s} u dy dz$	$\bar{\theta}^{(t)} = \int_0^{z_s} f(z,t) dz$	
Zero-flux condition at all boundaries other than $y = 1$. Initial temperature assumed zero.			

Table 3.3: Hierarchy of conduction Models

3.3.3 Simplifications and Solutions

To complete the non-dimensionalization equations 3.2, 3.3, 3.5 and 3.6, the following scalings are added

$$u \equiv \frac{T - T_o}{T_c}, \qquad q \sim q_s, \qquad \text{with } T_c \equiv q_s \xi / k$$

leaving the full 2D initial-boundary value problem given in Table 3, where the step behavior in space and time in the surface boundary condition discussed above is represented by $f(z,t)$. It is understood that a zero-flux condition is imposed at all non- $y = 1$ boundaries and the initial (scaled) temperature is taken to be zero. These will not be rewritten.

The full 2-dimensional solution is plotted in Figure 3.6 for two radial depths and three axial positions, identified in Figure 3.5. Points (1) and (2), at the wheel center are directly beneath the heat-source. At point (1), the effect of the puddle during each revolution is apparent as spikes, however at point (2) lower in the wheel, the temperature rise is monotonic, not exhibiting spikes. It is also clear that while the heat source is applied, the temperatures at (1) and (2) are never the same at a given instant. For slower wheel speeds, there is more time between heat-

ing phases and these temperatures can approach each other. This will be discussed in the data comparison section. At axial positions beyond the heat-source (3)-(6), temperature profiles nearly coincide for both radial positions. Temperature spikes are not observed. At the outer edge of the wheel, (5) and (6), the temperature is seen to remain zero until after about 2.5 s, when it begins to rise. Before this time, the slab appears semi-infinite in the 'z-direction.' After this time, the outer axial boundary condition is felt.

One of the practical uses of this model is predicting the temperature at the

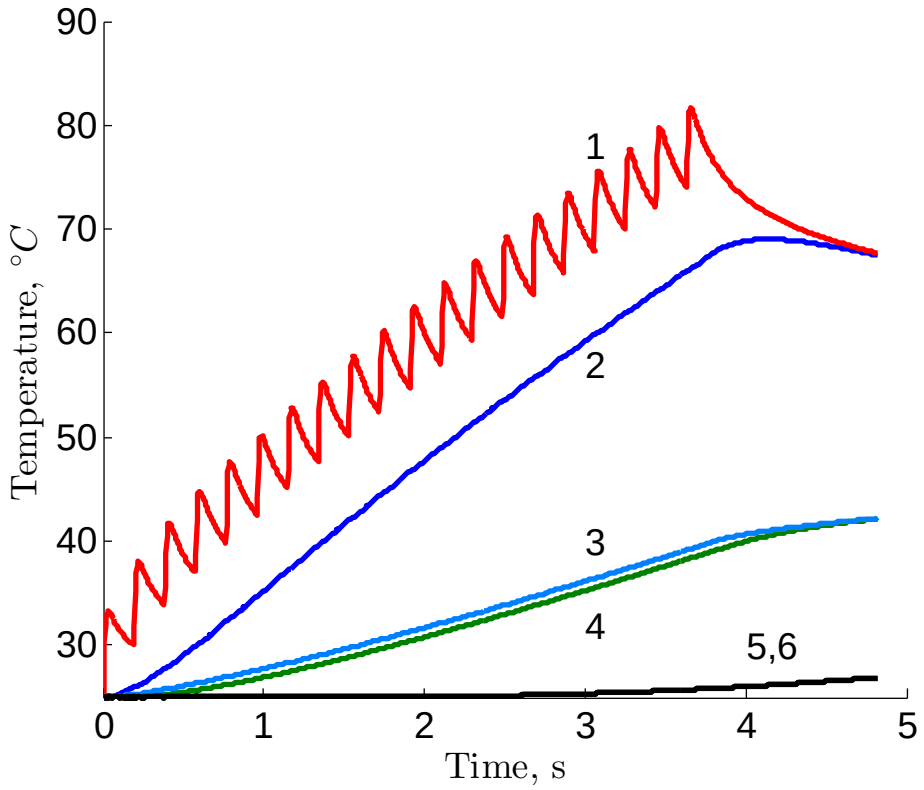

Figure 3.6: Predicted temperature versus time from (2D) model at various radial and axial locations, under typical casting conditions summarized in Table 1.

upper and lower wheel surfaces. If, during solidification, there were perfect contact between the melt and the wheel surface, one would expect the wheel surface to

instantaneously reach the melt temperature. For $Al-7\%Si$ cast on a copper wheel, the melt temperature, 614 $^\circ C$, is well below the copper melting point of 1085 $^\circ C$. However, if iron were to be cast, its melt temperature $> 1500\ ^\circ C$ is greater than the substrate's. Thus, in the case of perfect melt-wheel contact, iron alloys could destroy the casting wheel. Plots of the upper surface temperature given in Figure 3.7 reveal that the wheel surface only rises by $\sim 100\ ^\circ C$ for $Al-7\%\ Si$ alloys, and only achieves a maximum temperature for a short time. After the wheel passes from the puddle, the surface temperature rapidly decays as heat is conducted into the wheel. At the lower surface, the temperature rises monotonically.

Rapid temperature fluctuations happen only in the region directly beneath the heat source. Although the full solution has shown that there is axial conduction during a cast, it will be insightful to consider a 1-dimensional version of the full solution to understand the overall shape of the temperature rise in the TC plots. An axially averaged temperature is defined as

$$\theta_y(y,t) \equiv \int_0^1 u(y,z,t)dz \tag{3.7}$$

reducing the problem to the axial-averaged 1D problem given in Table 3, depicted in Figure 3.5b. Due to the step-nature of $f(z,t)$, the integral in the surface boundary condition reduces to $\int_0^1 f(z,t)dz = q(t)z_s$.

Plots of the axial-averaged model are given as solid circles in Figure 3.8, for the same radial positions as points (1) and (2) in Figure 3.6. Spikes are observed at (1) but not at (2). However, after a period of time (indicated by the dashed line in Figure 3.8, the time-averaged shape of the temperature profiles becomes linear, as opposed to the concave-down shape seen in the full solution and the data. This indicates that axial conduction out of the region below the heat-source becomes

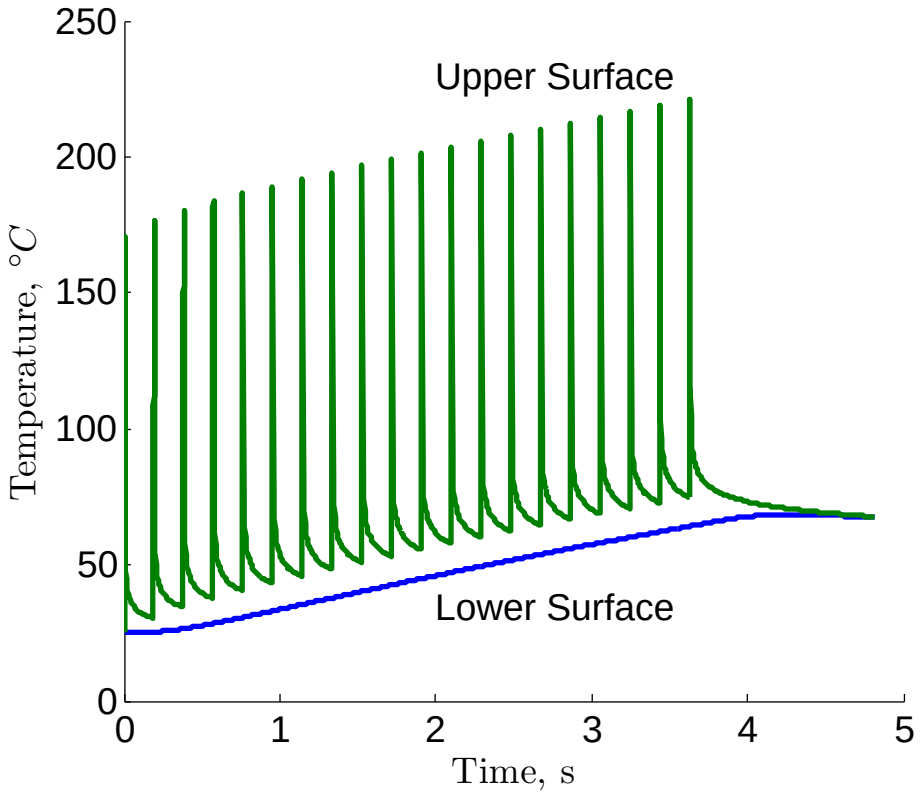

Figure 3.7: Predicted temperature versus time at upper and lower wheel surfaces from (2D) model. Temperature is predicted to rise by $> 100\ K$ at the upper surface and then rapidly decay as heat conducts radially into the wheel.

important in experiment and the full solution. To illustrate this more clearly, full and axial averaged solutions are plotted together in Figure 3.9. Around $2s$, the full solution predicts lower temperatures than the axial average.

Temperature traces in both the 1- and 2-dimensional models exhibit curvature at the cast start. To examine this, the axial-averaged 1D IBVP (Table 3) is considered, with the effective flux (equation 3.6) imposed at the outer wheel surface. The advantaged to solving this problem with a time *independent* surface condition is that solutions are well known. At early times, the surface temperature grows like a semi-infinite slab $2q_e(\alpha t/\pi)^{1/2}/k$ [16]. After the initial transience, the surface

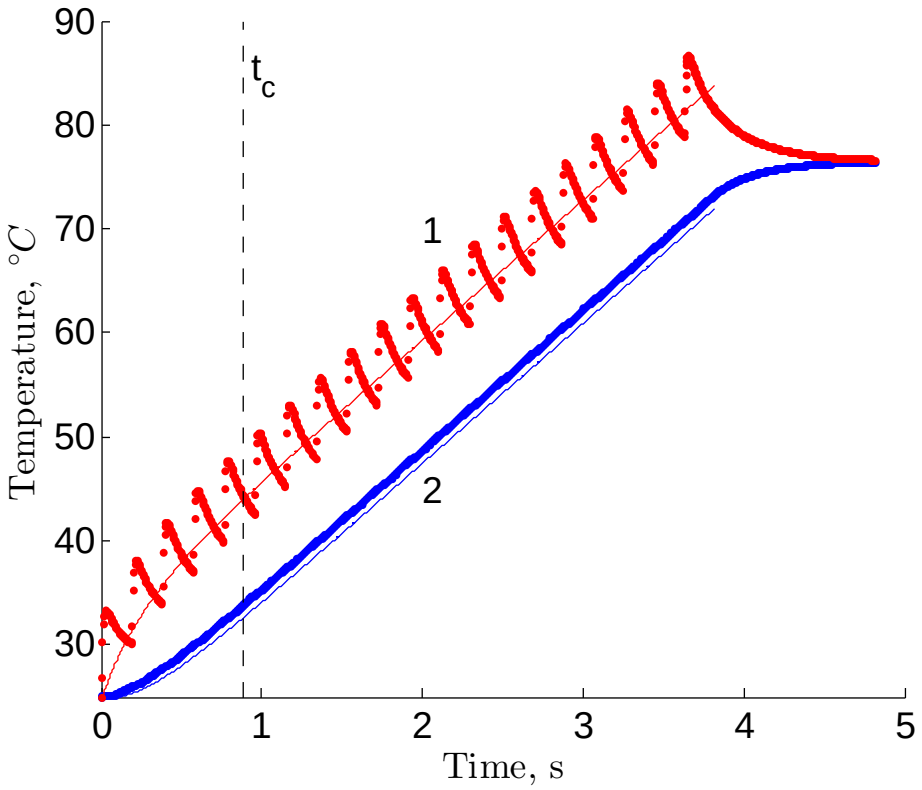

Figure 3.8: Predicted temperature versus time from (A1D) model. Solid lines: temperature when cyclic heat source is applied, dotted lines: temperature when heat source is averaged in time. To the left of dashed line, $t < t_{LS}$, wheel acts as a semi-infinite solid. To the right of the dashed line, $t > t_{LS}$, the lower surface is felt and overall temperature growth is linear with time.

temperature grows linearly as $q_e[\alpha t/\xi + 1/3]$ [16]. The transition occurs when the temporal growth rates of each model are equal, at a time

$$t_c = \xi^2/\pi\alpha. \tag{3.8}$$

Figure 3.8 is a plot of the axial-averaged solution for the cyclic and effective flux. The initial transience, apparent in both plots, lies to the left of t_c, given as a dashed line. To the right of t_c, the overall growth rate is linear. It is also found that at time $2t_c$, axial conduction becomes significant and the wheel behaves like a 2-dimensional solid.

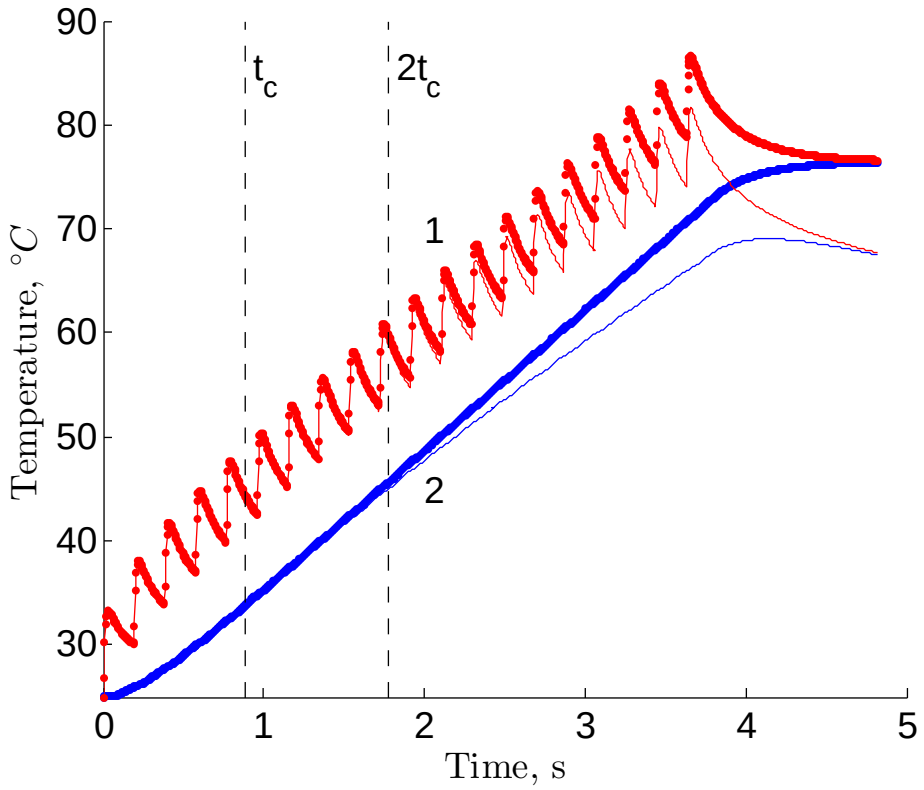

Figure 3.9: Predicted temperature versus time, comparing (2D) and (A1D) models. Temperature growth is linear $t_{LS} < t < t_{OE}$, but then axial conduction (absent in (A1D)) causes downward curvature in the overall temperature g

3.4 Data comparison against model prediction

Before looking directly at thermocouple data, the full solution is used to examine the effect of changing parameters in the model. First, we note that

- k, α, ξ, W and h_s are material or geometric constants and are assumed unchanging within a cast.
- U is set beforehand and measured during a cast. It does not change appreciably during a cast ($< 1\%$).
- τ and z_s are measured within a cast and observed to *decrease* throughout

the cast typically.

- x_s is difficult to directly measure with accuracy, but has been observed to increase during a cast.

The effect of changing τ, x_s, and U will be considered individually, holding all other parameters at their constant values.

To illustrate the effect of decreasing τ, an exaggerated change from 150 to 50 μm over 20 revolutions will be imposed. This will reduce the numerical value of q_j for each revolution. Predictions of the full model are given in Figure 3.10. While similar in appearance to Figure 3.2, the concavity of the overall rise is amplified at points (1) and (2) in the slab. Inspection of this plot shows that, as τ decreases, the size of the temperature spike at position (1) *decreases* per revolution.

The puddle length, x_s, does not enter the model directly, since the x-direction is ignored completely. Instead, it influences the duration of the heating phase for each revolution. Predictions are shown for an increasing x_s from 1 to 2 cm in Figure 3.11. Increasing puddle length *increases* the temperature rise at position (1) for each revolution. This gives an overall concave-up shape to the curve, something never observed in our data.

Like puddle length, U is not directly input into the model. Instead, it affects the duration of the heating *and* cooling phase for each revolution. A faster wheel speed will shorten the heating phase, yielding smaller temperature spikes, and shorten the cooling phase, giving less time for heat to conduct radially inward. Though the temperature rise per revolution will be smaller, there will be less time between heating phases, hindering the approach of temperatues at (1) and (2) to

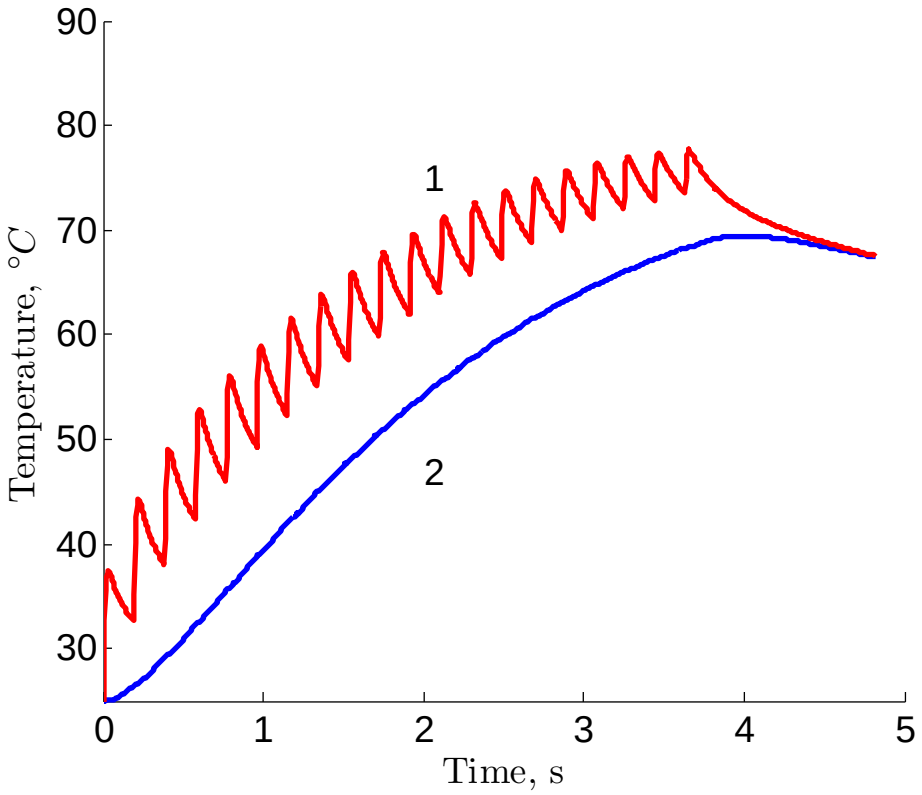

Figure 3.10: Predicted temperature versus time as thickness τ decreases from 150 to 50 μm over 20 revolutions. The effect is to decrease the temperature rise per revolution, contributing to the overall concave-down shape of the traces.

each other. For slower wheel speeds, the heating phase will be longer, yielding a greater temperature rises per revolution. However, increased cooling time allows conduction to nearly equalize the temperatures at (1) and (2). This is shown in Figure 3.12.

A comparison with data is given in Figure 3.13. This cast was not chosen for comparison because of good agreement with model and data, but because the thickness data for this cast, shown in Figure 3.3 is 'well-behaved,' in that the overall trend is a slow, linear decrease. Note that the thickness data ends at 6 s, and so the data was linearly extrapolated beyond this. The puddle length for this cast

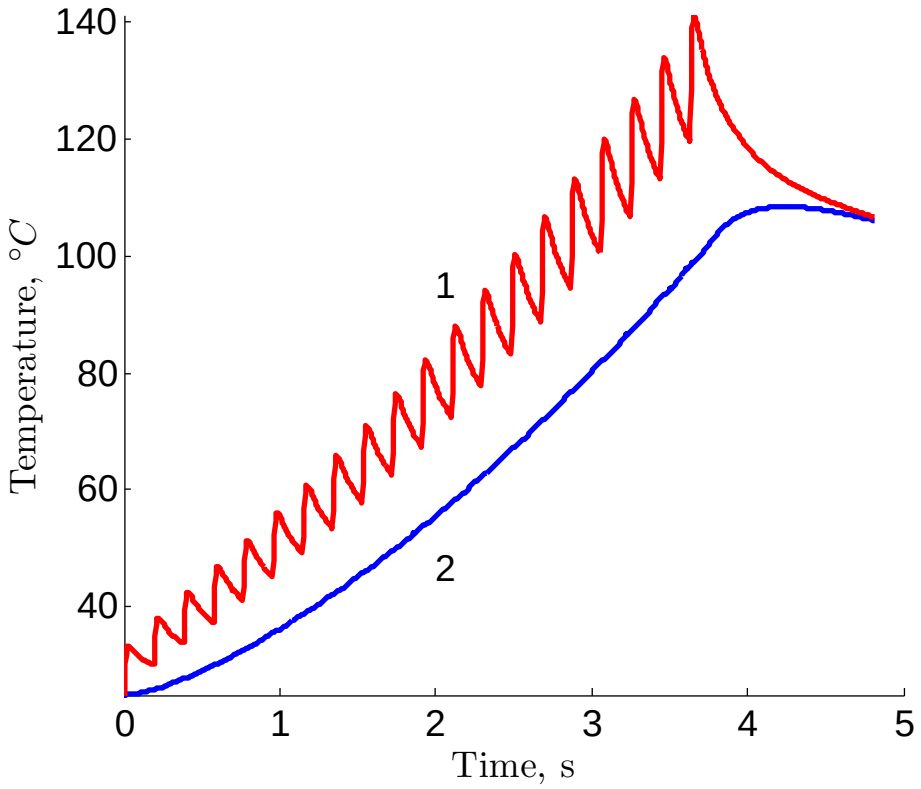

Figure 3.11: Predicted temperature versus time as puddle length L_s increases from 1 to $2cm$ over 20 revolutions. The effect is to increase the heating time that the CV experiences, increasing the temperature rise per revolution, contributing to an overall concave-up shape of the traces. Although L_s has been observed to increase during a cast, such a pronouced concave-up shape has never been observed in the data.

is un-measured. Here it is assumed to be 1 cm, a typical value [76]. The wheel speed is 5.8 m/s. The thickness and wheel speed are the only measured parameters input into the model. Discrepancies with the data early in the cast are likely due to fluctuations in unknown puddle length, and late in the cast are likely due to the use of extrapolated thickness data.

Finally, we discuss the analysis of Theisen, et al. (2010)[76]. They define a control volume bounded by wheel circumference, rim thickness ξ, and width $2z_s$, and assume that the heat is spread uniformly throughout as a function of time. In

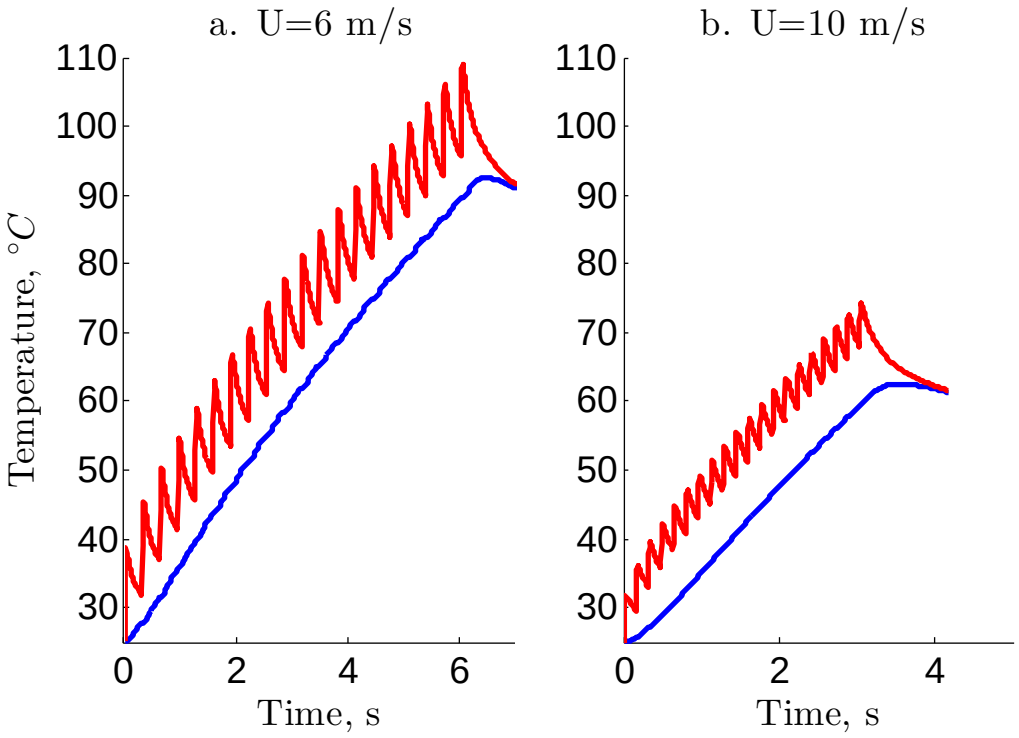

Figure 3.12: Predicted temeprature versus time for wheel speed $U = 6\ m/s$ (left) and $U = 10\ m/s$ (right). For slower speeds, heating phase is longer per revolution, yielding a greater overall temperature rise. Cooling times are also longer, so TC traces approach eachother at the end of each revolution. For faster speeds, heating phase is shorter per revolution, yielding lower overall temperature rise. Cooling times are also shorter, so large radial gradients persist.

the context of Table 3, this is a 0-dimensional, spatially average model. They then assume uniform volumetric expansion to determine the change in gap throughout a cast. They find good agreement of gap and overall temperature rise early in the cast, but see diminished quality of fit $2 - 2.5\ s$ into the cast. As discussed above, this is the time frame when axial conduction out of a ribbon width control volume begins to affect the temperature. Their model could be improved by allowing the width of their control volume to increase in the cast.

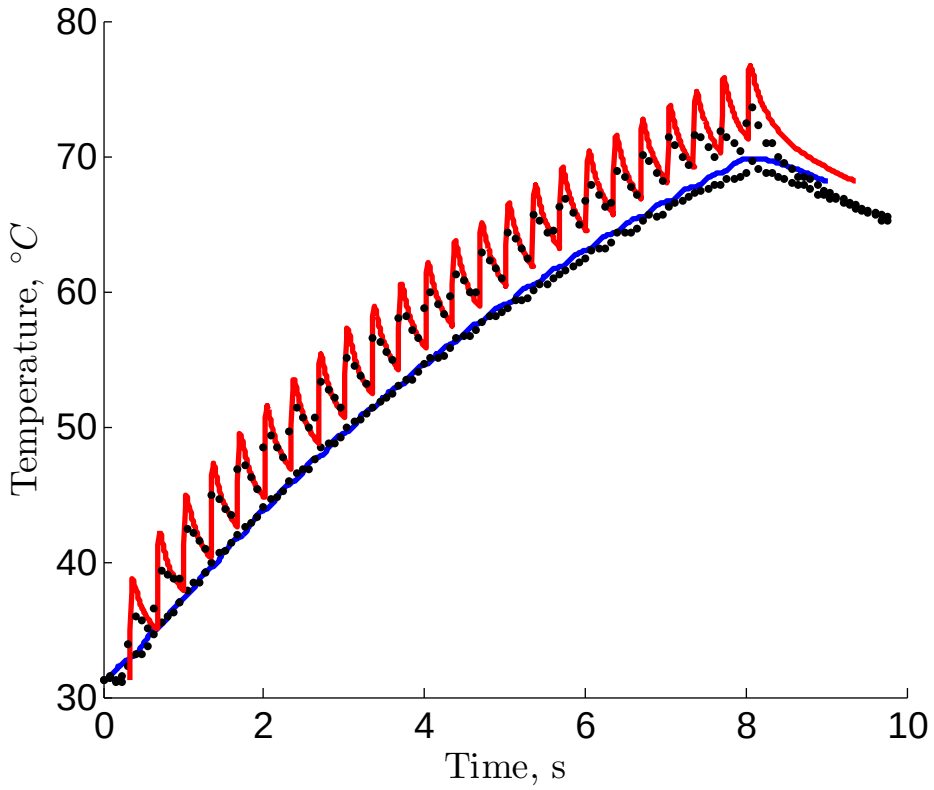

Figure 3.13: Measured (dots) versus predicted (line) temeperature versus time. Here, L_s was assumed to be constant and the cast was chosen such that τ decreased steadily (i.e. no sudden changes in τ). Since L_s was not measured for this cast, exact agreement with the data is not expected.

3.5 Internal cooling

In an industrial application, casting might go on for extended periods of time and the wheel temperature would continue to rise. To avoid this, an internal cooling system could be introduced, as discussed by Karpe, et al. (2011)[45]. To achieve wheel cooling, a cooling fluid could be circulated inside of the wheel depicted in Figure 3.5c, removing heat from the inner wheel surface. For a fluid

flowing past a solid boundary, the usual expression for the heat-flux across the boundary is $H(T - T_0)$, where H is a interfacial heat-transfer coefficient, T is the temperature of the solid, and T_0 is the *constant* fluid temperature. Assuming that the fluid temperature is the same as the initial slab temperature, the non-dimensional boundary condition at $y = 0$ in the conduction model above becomes

$$u^{(y)} = Bu \tag{3.9}$$

$$B \equiv H\xi/k \tag{3.10}$$

where u is the dimensionless temperature defined above, ξ is the rim thickness, k is the wheel thermal conductivity, and B is the Biot number, representing the ratio of heat-transfer resistance within the solid to across the solid-liquid interface. The solution, given in Table 3.4, is similar to the case of an insulated inner edge, with the eigenfunctions and eigenvalues of the Fourier series slightly different.

A plot of the surface temperature for $Bi = 1$ is given in Figure 3.14. Like the insulated case, the temperature rapidly rises and falls with each revolution. However, unlike the insulated case which had a continually rising temperature, the overall temperature for the cooled case reaches a 'steady' state. The temperature continues to rapidly rise and fall, but the final temperature at the end of each revolution, $u*$ remains the same. This temperature is found to be

$$u = q_e \left[y + 1/B \right] \tag{3.11}$$

where q_e is the effective flux defined in 3.6.

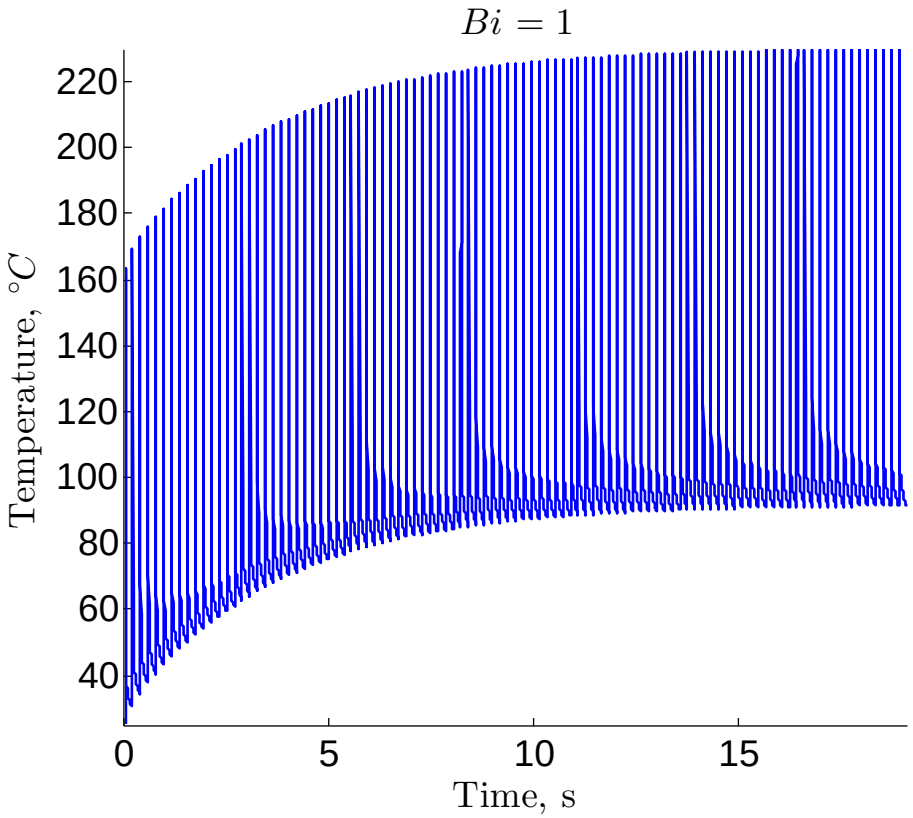

Figure 3.14: Temperature profile at wheel upper surface with internal cooling for $Bi = 1$.

3.6 Summary

A simple conduction model has been used to explain the features of embedded thermocouple output during planar-flow melt spinning casts. These features are: i) an overall increase in wheel temperature by $40 - 50^{\circ}C$, ii) sharp temperature spikes near the wheel surface, but a monotonic temperature rise deeper in the wheel, iii) overall concave-down shape of temperature profiles. Various averages of the full conduction model were used to understand temperature profiles in the wheel and the effect of changes in ribbon thickness, puddle length, and wheel speed were examined. The results are summarized:

1. Circumferential conduction can be neglected due to large Peclet number
2. Radial thermal gradients exist directly beneath the solidification zone, but outside of this zone temperatures increases in the same manner for all depths
3. Initial curvature of the overall heatup occurs while the wheel acts like a semi-infinite solid. The effect of the inner surface sets in at $t = \xi^2/\alpha\pi$
4. After $t = \xi^2/\alpha\pi$, the heat-affected zone grows linearly in the radial direction like a one-dimensional solid with a flux applied at one boundary and insulated at the other. This persists until axial conduction becomes signifcant at $t = 2.3\ s$.
5. The concave-down nature of the temperature profiles is caused by axial conduction out of the region directly beneath the puddle. Another source of curvature is *decreasing* ribbon thickness, which is typically observed during a cast.
6. *Increasing* puddle length gives temperature profiles an overall concave-up shape, which has never been observed in our data.
7. Temperatures within the wheel underneath the puddle approach eachother as wheel speed *decreases*.
8. Using wheel speed and thickness as input parameters, the temperature profiles can be predicted and compared with thermocouple data.

3.7 Appendix

Solution of the conduction models introduced in Table 3 are summarized in Table 4. The 'outer' sums with indices n or m are the usual Fourier series type solutions which arise in conduction problems. A new feature of these solutions, not

presented in standard conduction texts [16] is the 'inner' sum, with index p. The inner sum counts the number of heating/cooling cycles that the control volume has experienced, where J is the current cycle. For every cycle, p takes values from 1 (first cycle) to $J-1$ (the last cycle before the current one), accounting for the heating history of the control volume. Note that, if $J = 1$, then the inner sum drops out, and the 1-dimensional solutions reduce to well known cases of a slab with constant heat-flux boundary condition at one surface [16].

Model	Solution
Full 2D	$u = z_s p\Lambda_{00}$ $+2\sum_{n=1}^{\infty} z_s\chi_n(1)\chi_n(y)e^{-\lambda_n^2 t}\Lambda_{n0}/(\lambda_n^2)$ $+2p\sum_{m=1}^{\infty}\hat{\psi}_m(z_s)\psi_m(z)e^{-a\nu_m^2 t}\Lambda_{0m}/a\nu_m^3$ $+4\sum_{n=1}^{\infty}\sum_{m=1}^{\infty}\hat{\psi}_m(z_s)\psi_m(z)\chi_n(1)\chi_n(y)e^{-\mu_{nm}t}\Lambda_{nm}/\nu_m\mu_{nm}$
Axial Average 1D	$\theta_y = z_s p\Lambda_{00} + 2\sum_{n=1}^{\infty} z_s\chi_n(1)\chi_n(y)e^{-\lambda_n^2 t}\Lambda_{n0}/(\lambda_n^2)$

$\Lambda_{00} \equiv q_J\left(t - t_{J-1}\right) + \sum_{p=1}^{J-1} q_p\left(t_p - t_{p-1}\right)$
$\Lambda_{n0} \equiv q_J\left(\exp\left[\lambda_n^2 t\right] - \exp\left[\lambda_n^2 t_J\right]\right) + \sum_{p=1}^{J-1} q_p\left(\exp\left[\lambda_n^2 t_p\right] - \exp\left[\lambda_n^2 t_{p-1}\right]\right)$
$\Lambda_{0m} \equiv q_J\left(\exp\left[a\nu_m^2 t\right] - \exp\left[a\nu_m^2 t_J\right]\right) + \sum_{p=1}^{J-1} q_p\left(\exp\left[a\nu_m^2 t_p\right] - \exp\left[a\nu_m^2 t_{p-1}\right]\right)$
$\Lambda_{nm} \equiv q_J\left(\exp\left[\mu_{nm} t\right] - \exp\left[\mu_{nm} t_J\right]\right) + \sum_{p=1}^{J-1} q_p\left(\exp\left[\mu_{nm} t_p\right] - \exp\left[\mu_{nm} t_{p-1}\right]\right)$

Insulated case:
$\chi_n = \cos(\lambda_n y),\ \psi_m = \cos(\nu_m y),\ \bar{\psi}_m = \sin(\nu_m y),\ \lambda_n = (n\pi),\ \nu_m = (m\pi)$

Cooled case:
$\chi_n = a_n\left[\sin(\lambda_n y) + \lambda_n\cos(\lambda_n y)/B\right],\ \psi_m = \cos(\nu_m y),\ \bar{\psi}_m = \sin(\nu_m y)$
λ_n roots of: $B\cos(\lambda_n) - \lambda_n\sin(\lambda_n) = 0,\ \nu_m = (m\pi)$
$a_n = \left[4B^2\lambda_n / \left\{2\lambda_n(B^2 + B + \lambda_n^2) + (\lambda^2 - B^2)\sin(2\lambda_n) - 2B\lambda_n\cos(\lambda_n)\right\}\right]^{1/2}$

Table 3.4: Solutions to various heat-conduction models

CHAPTER 4

CAPILLARY VIBRATIONS AND PERIODIC FEATURES IN PLANAR-FLOW MELT SPINNING

4.1 Introduction

In the planar-flow melt spinning process, liquid metal is forced through a nozzle of breadth B onto a rotating chill wheel which extracts latent heat, causing solidification, Figure 1.4. The gap G separating the nozzle from the wheel is sufficiently small ($O(10^{-3}\ m)$) that capillary pressure balances fluid inertia, causing a liquid bead or puddle to form, held in place by surface tension. Upon solidification, ribbon with final thickness τ is removed from the puddle region by the rotating the wheel. The rotation rate of the wheel can be expressed as a linear translation rate, called the wheel speed U. See Chapter 1 for details.

It has been shown that the narrow gap in PFMS and the prescence of a solidification 'suction' layer stabilize the fluid flow in the puddle [65]. Nonetheless, localized thickness variations in the ribbon, most often referred to as ribbon defects, are observed over many length scales. Whether these defects degrade or enhance the quality of the product depends on the application; in either case, precise understanding and control of them is desired. As 'defect' implies quality degradation, we also use the terms 'feature' or 'thickness variation' to refer to them.

Praisner, et al. discuss a number of ribbon features in PFMS as a function of casting parameters such as wheel speed, applied pressure, and molten metal superheat [62]. They identify 'steaks,' 'dimples,' and 'wavy' features as distinct casting

features. The wavy feature spanned the width of the ribbon and appeared periodically. These will be the focus of this chapter.

Periodic features on the wheel- and air-side of the ribbon are visible to the naked eye. These are localized thickness variations which span the width of the ribbon, and appear to be continuous wavy lines. The top and bottom (air- and wheel-side) of a piece of ribbon are depicted in Figure 4.1. Through optical profilometry (Byrne, et al. 2006), discrete 'bubbles' are revealed on the wheel-side, while a continuous 'valley' appears on the air-side [12].

It is believed that vibrations of the upstream mensicus (USM) allow air bub-

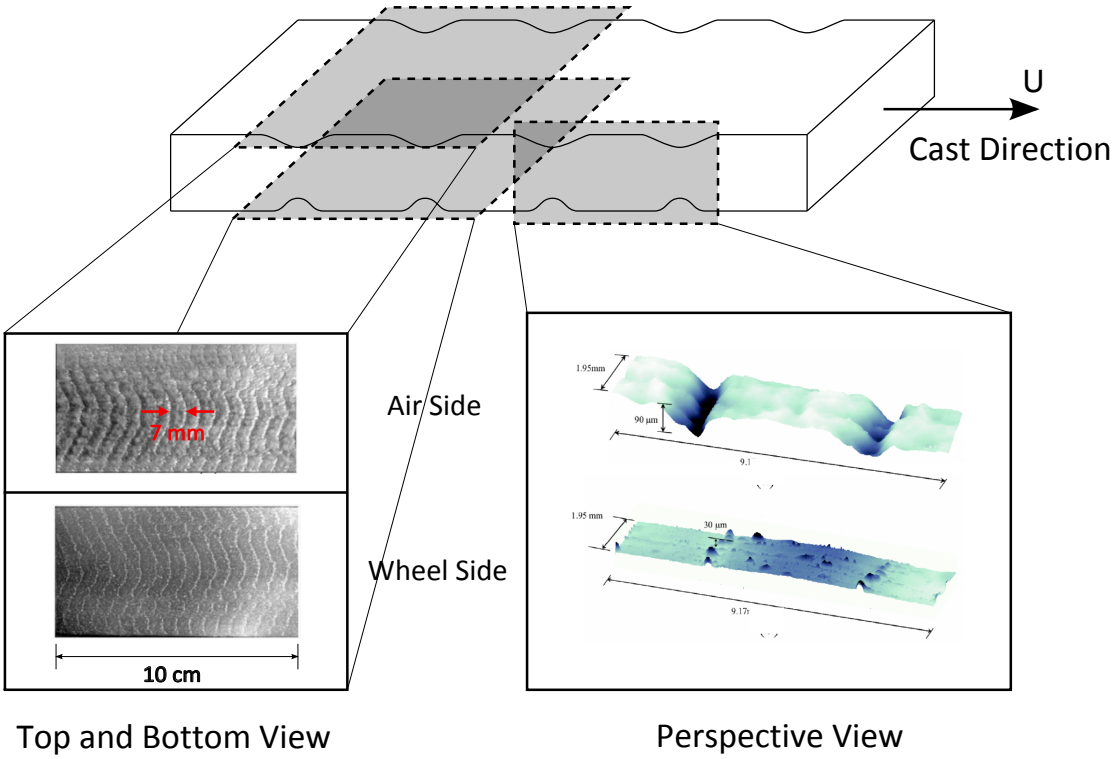

Figure 4.1: Periodic thickness variations appear on the air- and wheel-side of the ribbon which span the width. Optical profilometry [12] reveals discrete bubbles on the wheel-side and continuous vallies on the air-side

bles to become entrained betweeen the puddle and the wheel. The air pockets act

as an insulator, reducing the rate of heat-transfer from the puddle to the wheel, locally reducing the ribbon thickness. Thus, the shape of the solidified metal on the wheel side is caused by the physical presence of air pockets, and the shape on the air-side is caused by reduced solidification rates due to the heat-transfer interruption caused by air entrainment. This is shown in Figure 4.2. USM vibrations were observed using high-speed video by Byrne, et al. (2006) and eight still images from one period are shown in Figure 4.2[12].

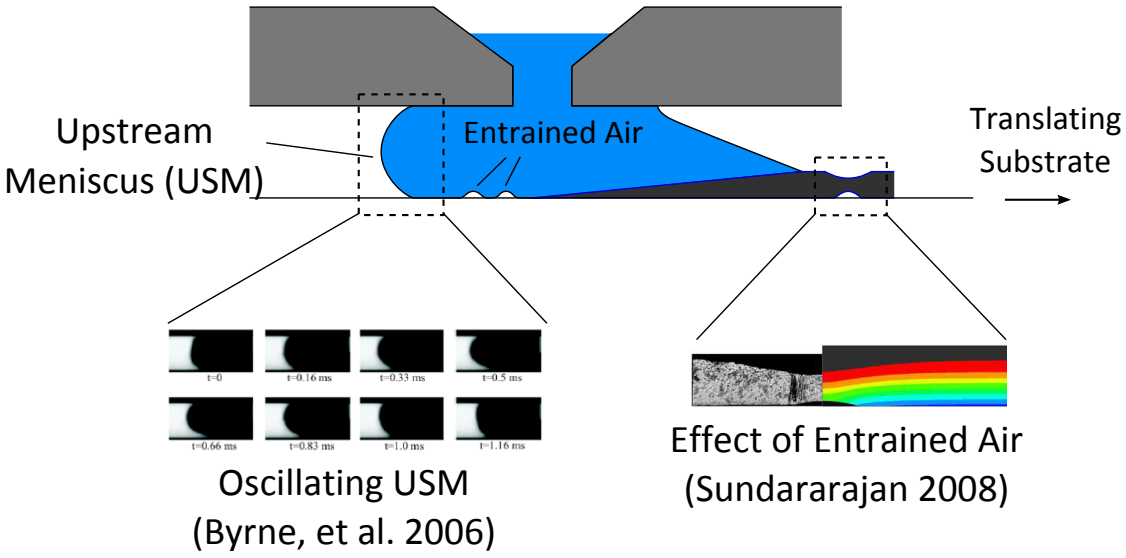

Figure 4.2: Vibrations of the USM are thought to cause air entrainment. Air acts as an insulator between the solidifying metal and wheel, reducing heat transfer and subsequent ribbon thickness.

Numerical modeling of the solidification by Sundararajan (2008) predicted the effect of an air pocket between the wheel and puddle and found favorable agreement with actual ribbon[72], shown in Figure 4.2. Heat transfer-interruptions have also been intentionally introduced as a means of creating patterns on the ribbon. Bryne, et al. (2007) used a high-powered laser to create local hot points on the wheel, causing dimples in the ribbon product. They also painted boron-nitride

on the wheel to act as a heat-transfer interruption, and were able to transfer prescribed patterns onto the ribbon [11].

Two distinct periodic features are discussed in the literature. A lower frequency feature called crosswave (CW) was observed to appear with $\lambda \sim 1\ cm$ spacing, corresponding to a frequency $f \sim 1\ kHz$, where $f \equiv U/\lambda$ [Byrne, et al (2006)][12]. Using dimensional analysis, it was found that the frequency of this feature was proportional to the characterstic capillary frequency, $f_c = (\sigma/\rho G^3)^{1/2}$, suggesting that the feature is related to capillary vibrations of the puddle [12]. A plot of CW frequency versus f_c is given in Figure 4.3. The data appear to fall on a line with slope 2.1.

A second periodic feature of higher frequency, called herringbone (HB), was discussed by Cox and Steen [20]. This feature, while similar in appearance to CW, appeared with $\lambda \sim 1\ mm$ spacing corresponding to $f \sim 10\ kHz$. The data ploted versus f_c do not appear to fall around a line like the CW data, Figure 4.3. However, dimensional analysis suggests that HB also depends on a wheel-speed Weber number, We_U defined in Table 4.1. A plot of CW and HB versus We_U is given in Figure 4.4. CW is seen to have a zero-order dependence on the Weber number, falling on the constant line $f/f_c = 2.1$. HB falls on line with slope 0.08. The data presented here fall on a line with slope 0.04, because the factor of 1/2 used in the definition of We_U by Cox and Steen is omitted here.

Furthermore, Cox and Steen found that the geometry of the puddle is different for the formation of CW and HB. A necessary condition for the formation of HB is that the USM *must* pin at the nozzle inlet slot. If the USM depins, CW was

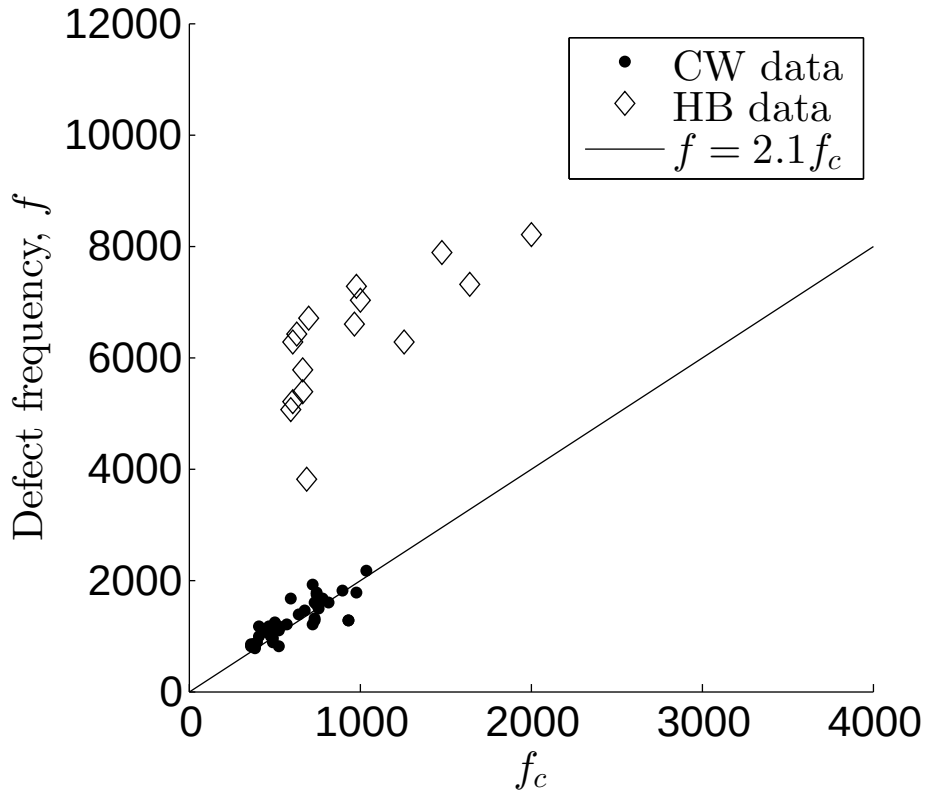

Figure 4.3: CW and HB data versus capillary frequency, f_c. CW data fall on line $f = 2.1 f_c$, while HB data do not appear to fall closely around a line.

observed, Table 4.1. They conclude for HB formation that the flow of metal under the nozzle and above the solidification region has no recirculation zone, but that for CW formation flow separation occurs, allowing a 'buffer' region of fluid which damps out the vibrations involved in HB formation. A summary of the known information about CW and HB features is given in Table 4.1.

The purpose of the following analysis is to examine these experimental findings with a simple model. In particular, two questions are addressed: 1)what is meant by pinning/de-pinning of the USM, and 2)what effect does flow past the USM have on the motion of the interface? Pinning the USM at the nozzle corner restricts the puddle length, L. It also allows inlet flow from the nozzle to travel

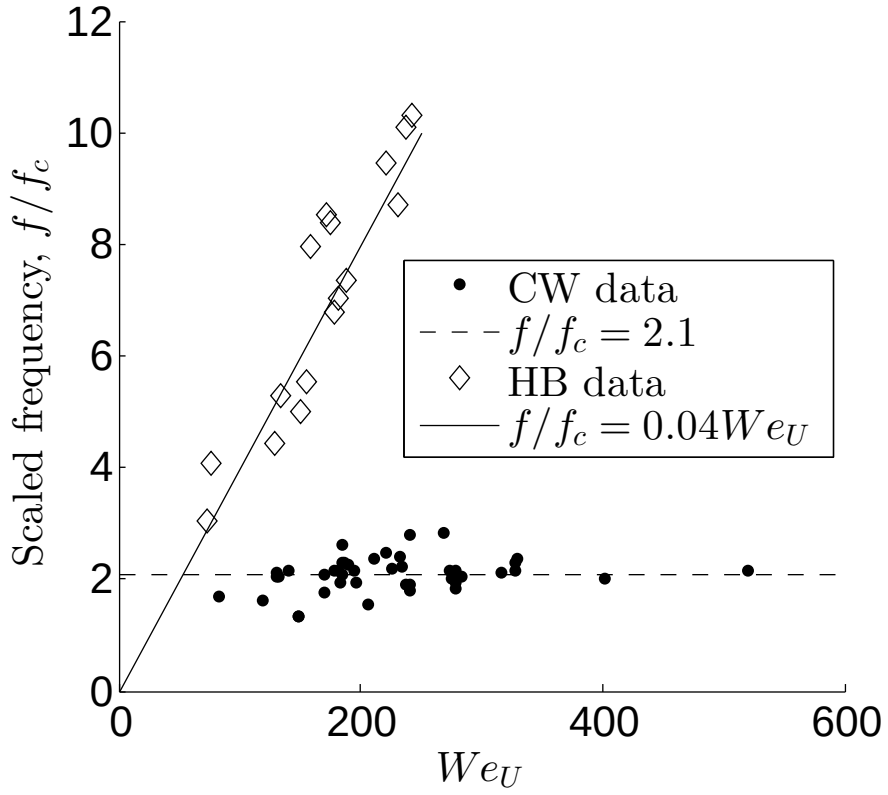

Figure 4.4: Scaled CW and HB data versus wheel-speed Weber number,We_U. CW data fall on constant line $f/f_c = 2.1$, while HB data fall on line $f/f_c = 0.04We_U$.

down along the interface, as Cox and Steen (2013) point out [20]. Additionally, the strict meaning of a *pinned* contact line (CL) is that the CL position along the substrate is fixed. The following analysis will examine the effect on the vibrational frequency of the interface of

- varying the puddle length, L,
- pinning the CL by pinning, or alternatively, fixing its contact angle (CA),
- imposing flow past the interface.

	Crosswave (CW)	Herringbone (HB)
	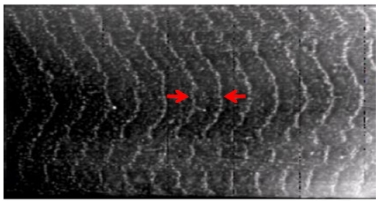	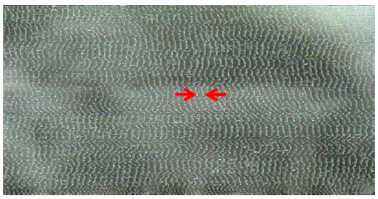
Spacing, λ	$10^{-2}\ m$	$10^{-3}\ m$
Frequency f	$1,000\ Hz$	$10,000\ Hz$
USM Position	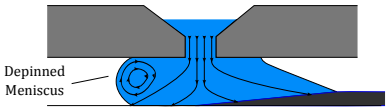	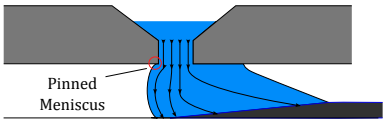
Scaling	$2.1 f_c We_U^0$	$0.04 f_c We_U^1$
$f_c \equiv (\sigma/\rho G^3)^{1/2}, \qquad We_U \equiv \rho U^2 G/\sigma$		

Table 4.1: Summary of two periodic ribbon features.

4.2 Experiment and Observations

A graphite crucible contains liquid metal prior to casting. At the cast onset, metal is forced at speed $u_{in} \sim 1m/s$ through the crucible nozzle with breadth $B \sim 1mm$ into the puddle region. The distance between the nozzle and the wheel is called the gap $G \sim 1mm$. The puddle extends both up- and downstream of the inlet and has length $L \sim 1cm$. The ribbon solidifies in the puddle to final thickness $\tau \sim 100\mu m$ and exits the puddle with wheel speed $U \sim 10m/s$, c.f. Figure 1.4.

U and G are set prior to a cast and measured throughout. High-speed video of the puddle is obtained for many casts. From these, meniscus vibrations are recorded and L can be measured. Post cast, the ribbon is cut into segments, weighed and measured to determine τ. To estimate the un-measured inlet velocity u_{in} from measured τ, U, and B, a steady puddle mass balance can be used

$$\rho_s \tau U = \rho_\ell B u_{in}, \tag{4.1}$$

where ρ_s and ρ_ℓ are the solid and liquid densities. Finally, the number of CW or HB features is counted on a cut segment. The number of features is related to the wavelength λ using $f \equiv U/\lambda$ and reported as a feature frequency.

4.3 Model of upstream meniscus motion

The upstream region of the gap will be modeled as a rectangular channel with a free interface, shown in Figure 4.5. The channel will be considered 2-dimensional, with its horizontal and vertical components denoted by the x- and y-coordinates, respectively. The upper and lower walls are, in general, permeable. The right-hand wall is impermeable. Opposite of the right-hand wall is a free interface which represents the upstream-mensicus (USM), whose shape is given by a function $h(s,t)$, where s is a spatial parameter on the free interface (like arclength).

The following assumptions are made:

1. Liquid is 2-dimensional: $\mathbf{v} = \mathbf{v}(\mathbf{x}, \mathbf{y}, \mathbf{t})$

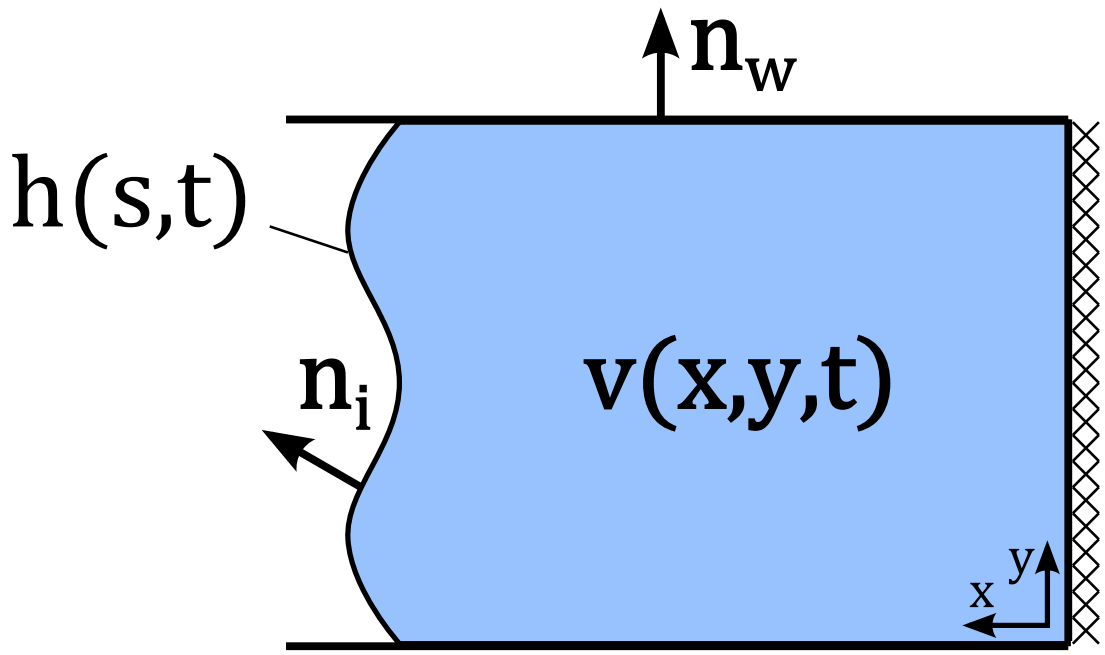

Figure 4.5: Definition sketch of a fluid in a rectangular channel with one free interface.

2. Liquid is inviscid $\mu \to 0$ and incompressible $\rho = const$
3. Passive air at pressure P_a is separated from the liquid by a free interface
4. Gravitational effects are negligible: Bond number $Bo << 1$
5. Liquid is irrotational: $\nabla \times \mathbf{v} = 0$

Assumptions 2. and 5. allow the use of a velocity potential defined: $\mathbf{v}(\mathbf{x}, \mathbf{y}, \mathbf{t}) = \nabla\phi(x, y, t)$, which satisifies the Laplace and Bernoulli equations, discussed in the next section.

4.3.1 Governing equations

Continuity

For an incompressible, irrotational flow(assumptions 1 and 5), the continuity equation requires that the velocity potential ϕ must satisfy Laplace's equation in the rectangular domain of the channel,

$$\nabla^2\phi = \frac{\partial^2\phi}{\partial x^2} + \frac{\partial^2\phi}{\partial y^2} = 0. \tag{4.2}$$

Momentum

An inviscid fluid (assumption 2) not subject to gravity (assumption 4) satisfies the Euler equation of motion

$$\frac{\partial \mathbf{v}}{\partial t} + (\mathbf{v}\cdot\nabla)\mathbf{v} + \frac{\nabla P}{\rho} = 0,$$

where $P = P(x, y, t)$. Making use of irrotationality (assumption 5), the velocity potential and pressure must satisfy the Bernoulli equation

$$\frac{\partial \phi}{\partial t} + 1/2(\nabla\phi)^2 + \frac{P}{\rho} = c(t) \tag{4.3}$$

where $c(t)$ is a spatially *independent* function for a given fluid streamline.

Kinematics

At the right wall, no-penetration is required ($\mathbf{v}\cdot\mathbf{n_w} = 0$). At the top and bottom interfaces, flow is allowed. The flow of fluid through the walls will be considered to be *steady*, but may vary as a function of horizontal position x. Denoting the

upper and lower walls with the subscripts u and ℓ, $\mathbf{v} \cdot \mathbf{n_w} = f_j(x)$, where $j = u, \ell$. In terms of ϕ these conditions become

$$\left(\frac{\partial \phi}{\partial n}\right)_w = \begin{cases} f_u(x) & (upper) \\ 0 & (right) \\ f_\ell(x) & (lower) \end{cases} \tag{4.4}$$

where $\partial\phi/\partial n \equiv \nabla\phi \cdot \mathbf{n}$ and subscript w denotes 'walls'.

The normal component of the velocity imparts a motion on the free interface according to the kinematic condition

$$\left(\frac{\partial \phi}{\partial n}\right)_s = \frac{\partial h}{\partial t} \tag{4.5}$$

where s denotes the free surface.

Momentum balance across interface

The normal stress boundary condition for an inviscid fluid of constant surface tension is given by the Young-Laplace equation

$$P_a - P = \sigma K \tag{4.6}$$

$$K \equiv \nabla \cdot \mathbf{n}_i \tag{4.7}$$

which relates the pressure jump across the interface to its mean curvature K multiplied by surface tension. The mean curvature is a function of the interface shape, $K = K(h(s,t))$, where s is the spatial parameter along the interface. For the flat and cylindrical coordinates used below, the 2D curvature can be expressed

$$\begin{aligned} &h''/[1 + (h')^2]^{3/2} && (flat) \\ &h^2 + 2(h')^2 - hh''/[h^2 + (h')^2]^{3/2} && (cylindrical), \end{aligned} \tag{4.8}$$

where $'$ represents a derivative with respect to s.

Volume constraint

The total volume is constant for an incompressible fluid. The interface is constrained to satisfy this constraint with

$$\int_{\Gamma} h = 0 \tag{4.9}$$

where Γ denotes integration along the free-interface.

Non-dimensionalization

Equations 4.2-4.9 will be scaled such that

$$length \sim G, \qquad pressure \sim \sigma/G, \qquad \phi \sim u_c G, \qquad t \sim (\sigma/\rho G^3)^{1/2}$$

where u_c is a characteristic velocity whose value will differ depending on whether or not there is base-flow in the channel.

4.4 Linearization and eigenvalue problem

Equations 4.2-4.9 comprise a non-linear system of equations. In particular, $(\nabla\phi)^2$, $(\partial\phi/\partial n)_w$, and $\nabla \cdot \mathbf{n_i}$ appearing in equations 4.3, 4.5, 4.7 are non-linear terms. These equations will be *linearized* to analyze the stability of known base-states to infinitessimal disturbances. Assuming a *steady* base-state, the following linearizations are defined:

$$\phi(x,y,t) = \phi_0(x,y) + \epsilon\phi_1(x,y,t), \qquad h = h_0(s) + \epsilon h_1(s,t)$$

$$P(x,y,t) = P_0(x,y) + \epsilon P_1(x,y,t), \qquad c(t) = c_0 + \epsilon c_1(t).$$

The base-state and disturbances equations are written in Table 4.2

	Base	Disturbance
Continuity	$\nabla^2\phi_0 = 0$	$\nabla^2\phi_1 = 0$
Bernoulli	$(w^2/2)(\nabla\phi_0)^2 + P_0 = c_0$	$w\partial\phi_1/\partial t + w^2\nabla\phi_0 \cdot \nabla\phi_1 + P_1 = c_1$
Walls	$(\partial\phi_0/\partial n)_w = f_\alpha,\ \alpha = u, \ell$	$(\partial\phi_1/\partial n)_w = 0$
Kinematic	$w(\partial\phi_0/\partial n)_s = 0$	$w(\partial\phi_1/\partial n)_s = \partial h_1/\partial t$
Young-Laplace	$P_a - P_0 = K_0$	$P = -K_1$
Dynamic	$(w^2/2)(\nabla\phi_0)^2 + P_a - K_0 = c_0$	$w\partial\phi_1/\partial t + w^2\nabla\phi_0 \cdot \nabla\phi_1 = K_1$

Table 4.2: Functions f_α represent flow through the walls in the base-state and are given by Equation 4.4. K_0 and K_1 are the $O(1)$ and $O(\epsilon)$ contributions to the curvature. The no-flow case is recovered by setting $w = 1$ and $\phi_0 = 0$ where $w^2 = \rho u_c^2 G/\sigma$.

The dynamic equations are found by applying the Bernoulli equation at the interface, where the pressure is related to the interface curvature.

4.5 Flat base-state

An initially flat interface is considered in this section. For a flat interface, $h_0 = L$, $K_0 = 0$, and $K_1 = \partial^2 h_1(y)/\partial y^2$. The kinematic boundary condition is

$$w\frac{\partial \phi_1}{\partial x} = \frac{\partial h_1}{\partial t} + w\left(\frac{\partial \phi_0}{\partial y}\right)\frac{\partial h_1}{\partial y} \tag{4.10}$$

and the dynamic boundary condition is:

$$\frac{\partial^2 h_1}{\partial y^2} = w\frac{\partial \phi_1}{\partial t} + w^2\left(\frac{\partial \phi_0}{\partial y}\right)\frac{\partial \phi}{\partial y}, \tag{4.11}$$

where the ϕ_0 term relates to the base-flow in the channel.

4.5.1 No-flow and base-flow

The equations presented so far have been general enough to accomodate any steady base-flow $\phi_0(x, y)$. Now, two flow conditions will be considered: no-flow, where the fluid is quiescent in its base-state ($\phi_0 = 0$), and base-flow, where a constant, vertical velocity is specified ($\phi_0 = -Uy$). The no-flow case is recovered from the base-flow case by setting $U = 0$. *Care must be taken when choosing the characteristic velocity u_c in w, however.* In the base-flow case, $u_c = U$. In the no-flow case, there is no imposed base-velocity, so we let $u_c = (\sigma/\rho G)^{1/2}$ and $w = 1$. *We represent both*

cases compactly as

$$w\frac{\partial \phi_1}{\partial x} = \frac{\partial h_1}{\partial t} - w\chi\frac{\partial h_1}{\partial y} \tag{4.12}$$

$$\frac{\partial^2 h_1}{\partial y^2} = w\frac{\partial \phi_1}{\partial t} - w^2\chi\frac{\partial \phi}{\partial y} \tag{4.13}$$

where

$$\begin{cases} \chi = 1, w \equiv (\rho U^2 G/\sigma)^{1/2} & \text{base-flow} \\ \chi = 0, w = 1 & \text{no-flow.} \end{cases} \tag{4.14}$$

Reduction to normal modes

The disturbance equations are linear and therefore we seek solutions which are exponential in time

$$\phi_1 = F\exp[\gamma t], \qquad h_1 = \eta\exp[\gamma t].$$

In general, γ is complex with growth rate b and frequency ω

$$\gamma \equiv b + i\omega.$$

The dynamic and kinematic conditions become

$$w\frac{\partial F}{\partial x} = \gamma\eta - w\chi\frac{d\eta}{dy} \tag{4.15}$$

$$\frac{\partial^2 \eta}{\partial y^2} = w\gamma F - w^2\chi\frac{\partial F}{\partial y}. \tag{4.16}$$

Solution to Laplace's equation

The velocity function F must satisfy Laplace's equation, no penetration at the 3 walls ($y = 0, y = 1, x = 0$), and the kinematic condition at the interface. Note

that for base-flow, the flow boundary conditions are satisfied at $O(1)$, leaving no-penetration conditions at $O(\epsilon)$. The solution is

$$F = \sum_{n=1}^{\infty} B_n \cosh(n\pi x)\cos(n\pi y)\int_0^1 \left[w^{-1}\gamma\eta - \chi\frac{d\eta}{dy}\right]\cos(n\pi y)dy \tag{4.17}$$

where $F = F(\eta(y))$, $B_n = 2/(n\pi\tanh(n\pi L))$. Its $x-$ derivative on the interface is

$$\frac{\partial F}{\partial x} = -\sum_{n=1}^{\infty} B_n(n\pi)\cosh(n\pi x)\sin(n\pi y)\int_0^1 \left[w^{-1}\gamma\eta - \chi\frac{d\eta}{dy}\right]\cos(n\pi y)dy. \tag{4.18}$$

Eigenvalue problem

Inserting 4.17 and 4.18 into the dynamic condition yields

$$\frac{\partial^2\eta}{\partial y^2} = \tag{4.19}$$

$$\sum_{n=1}^{\infty} B_n\cosh(n\pi L)\cos(n\pi y)\int_0^1 \left[\gamma^2\eta - w\gamma\chi\frac{d\eta}{dy}\right]\cos(n\pi y)dy \tag{4.20}$$

$$+\sum_{n=1}^{\infty} \chi B_n(n\pi)\cosh(n\pi L)\sin(n\pi y)\int_0^1 \left[w\gamma\eta - w^2\frac{d\eta}{dy}\right]\cos(n\pi y)dy. \tag{4.21}$$

The interface function η will be approximated as a series

$$\eta = \sum_{k=1}^{N} c_k\nu_k(y) \tag{4.22}$$

where c_k are constants and the choice of ν will be discussed in the next section. Finally, to reduce the equation to an algebraic one, an inner product will be defined

$$\int_0^1 (\cdot)\cos(j\pi y)dy$$

yielding a polynomial eigenvalue problem

$$\left[\gamma^2 A_{jk} + \gamma B_{jk} + C_{jk}\right]c_k = 0 \tag{4.23}$$

where

$$A_{jk} \equiv \sum_{n=1}^{\infty} D_n \int_0^1 \cos(n\pi y)\cos(j\pi y) \int_0^1 \nu_j \cos(n\pi y) dy \tag{4.24}$$

$$B_{jk} \equiv \chi w \sum_{n=1}^{\infty} D_n \int_0^1 \cos(n\pi y)\cos(j\pi y) dy \int_0^1 \frac{d\nu_j}{dy} \cos(n\pi y) dy \tag{4.25}$$

$$+ (n\pi) \int_0^1 \sin(n\pi y)\cos(j\pi y) \int_0^1 \nu_j \cos(n\pi y) dy \tag{4.26}$$

$$C_{jk} \equiv - \int_0^1 \frac{d^2\nu_j}{dy^2} \nu_k dy \tag{4.27}$$

$$- \chi w^2 \sum_{n=1}^{\infty} D_n \int_0^1 \sin(n\pi y)\cos(j\pi y) \int_0^1 \frac{d\nu_j}{dy} \cos(n\pi y) dy. \tag{4.28}$$

In the *no-flow* case, ($\chi = 0$ and $w = 1$) these matrices reduce to

$$A_{jk} \equiv \sum_{n=1}^{\infty} D_n \int_0^1 \cos(n\pi y)\cos(j\pi y) \int_0^1 \nu_j \cos(n\pi y) dy \tag{4.29}$$

$$B_{jk} \equiv 0 \tag{4.30}$$

$$C_{jk} \equiv - \int_0^1 \frac{d^2\nu_j}{dy^2} \nu_k dy. \tag{4.31}$$

Contact line conditions and basis functions

Three pairs of contact line (CL) conditions will be considered: two neutrally wetting CL (NN), one neutral and one pinned CL (PN), and two pinned CL (PP). These 3 conditions are illustrated for the no-flow case in Figure 4.6 and for the base-flow case in Figure 4.7.

The basis functions chosen to approximate h are assumed to be sine and cosine

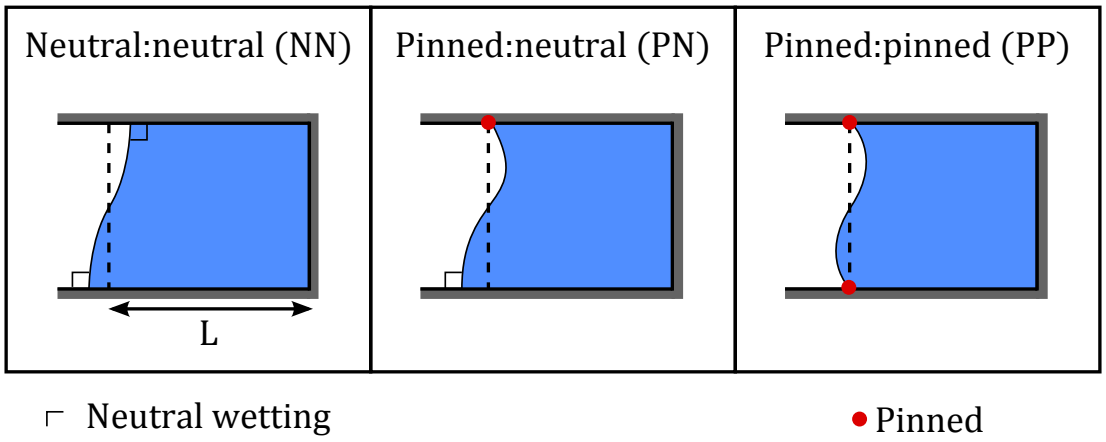

Figure 4.6: Flat interface cases with no base-flow: neutrally wetting CL (NN), one neutrally wetting, one pinned CL (PN), and two pinned CL (PP).

terms. The governing equations require that conservation of volume is satisfied, $\int_\Gamma h = 0$. In addition, they can be chosen to satisfy contact line conditions. The CL conditions for the NN, PN, and PP cases and their corresponding basis functions are given in Tables 4.3 and 4.4.

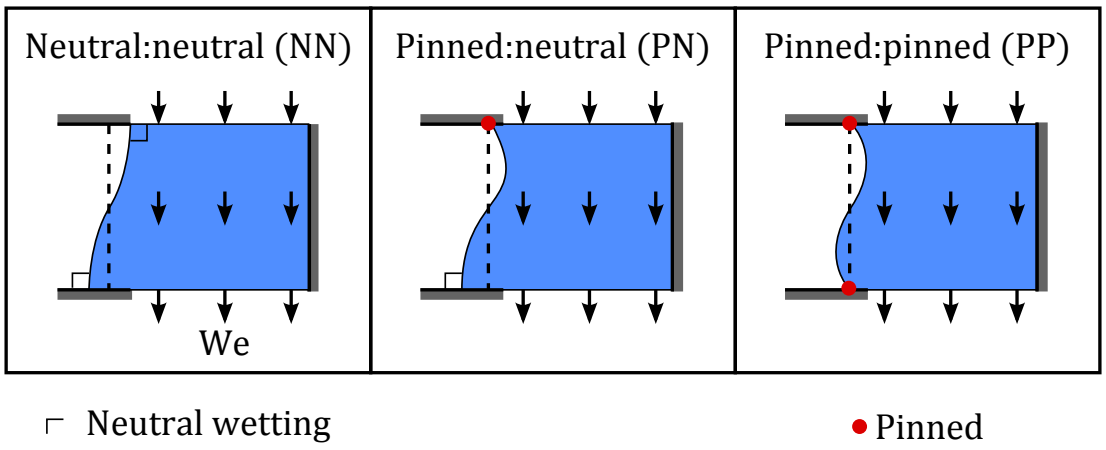

Figure 4.7: Flat interface cases with constant vertical base-flow: neutrally wetting CL, one neutrally wetting, one pinned CL, and two pinned CL.

Case	Boundary condition
Neutral:neutral (NN)	$dh(0)/dy = dh(1)/dy = 0$
Pinned:neutral (PN)	$dh(0)/dy = h(1) = 0$
Pinned:pinned (PP)	$h(0) = h(1) = 0$

Table 4.3: Contact line conditions for the flat interface problem.

4.5.2 No-flow

NN case: analytical solution

For the case of no-flow ($w = 1$, $\chi = 0$) and neutral wetting (NN), a solution can be found analytically by separation of variables or alternatively by the method outlined above. Both methods yield the same solutions, as expected. Inserting the

Case	Basis function, ν_k
NN	$\cos(k\pi y)$
PN	$\cos((2k+1)\pi y/2) + \cos(\pi y/2)/(2k+1)$ (k odd) $\cos((2k+1)\pi y/2) - \cos(\pi y/2)/(2k+1)$ (k even)
PP	$\sin((k+1)\pi y)$ (k odd) $\sin((k+1)\pi y) - \sin(\pi y)/(k+1)$ (k even)

Table 4.4: Basis functions ν_k used to approximate the interface disturbance for flat interface base-state.

basis functions and solving the eigenvalue problem for γ, it is found that γ has no real component, $\gamma = i\omega$. It is found that

$$\omega = \pm \left[(n\pi)^3 \tanh(n\pi L/G) \right]^{1/2}. \tag{4.32}$$

This frequency is given by Myshkis [58]. ω is the angular frequency, while the defect frequency is a linear frequency. ω is related to the linear frequency f by

$$f = \frac{2\pi}{\omega}. \tag{4.33}$$

The linear frequency f is reported in the remainder of this chapter. The effect of fluid 'volume' is seen by varying L/G, and is shown for the first 3 modes in Figure 4.8. For $L/G > 0.5$, the frequency is nearly independent of channel length. The corresponding mode shapes of the disturbed interfaces are given in Figure 4.9.

PN and PP cases

The NN case can be thought of as the 'natural' case for the flat interface. Constraining one or both contact line to be pinned is expected to raise the frequency.

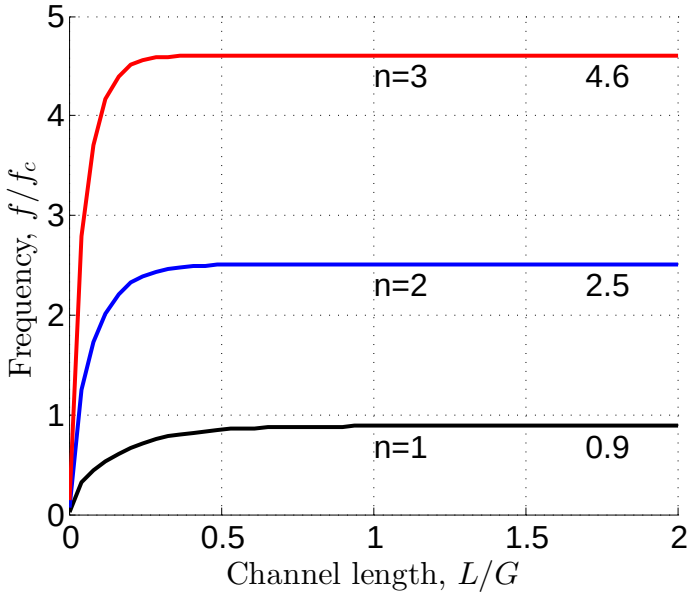

Figure 4.8: Scaled frequency versus channel length for no-flow NN case with asymptotes listed.

This is found to be the case for PN and PP cases. Like the NN case, γ is found to have no real part, $\gamma = i\omega$. The PN frequency is plotted against length in Figure 4.10 and corresponding interface shapes in Figure 4.11. The PP frequency versus length and corresponding interface shapes are shown in Figures 4.12 and 4.13, respectively. Similar to the NN case, eigenvalues are purely imaginary and become nearly independent of L/G for $L/G > 0.5$.

The first mode for the NN, PN, and PP cases versus channel length are shown in Figure 4.14. The asymptotic value of the three cases are approximately 5.6, 8.5 and 12.3 respectively. Thus, constraining both contact lines to be pinned more than doubles the vibrational frequency from the neutral wetting case.

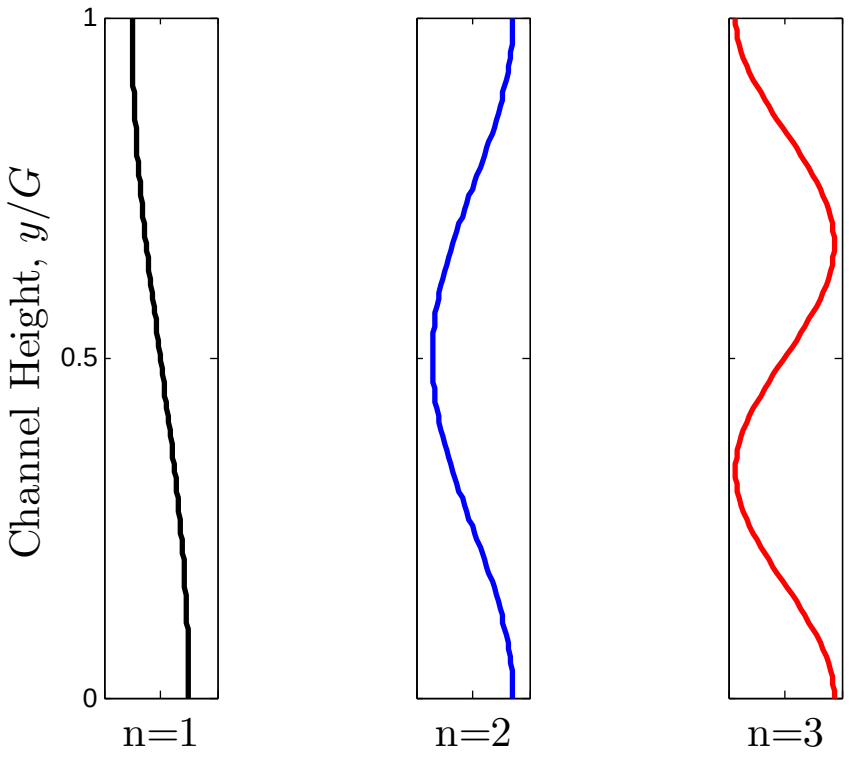

Figure 4.9: Interface shapes of first 3 modes for no-flow NN case for $L/G = 2$.

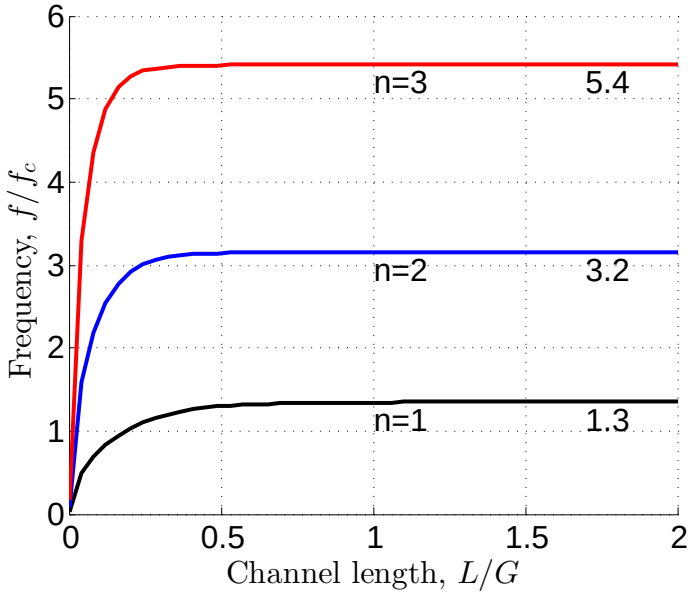

Figure 4.10: Scaled frequency versus channel length for no-flow PN case with asymptotes listed.

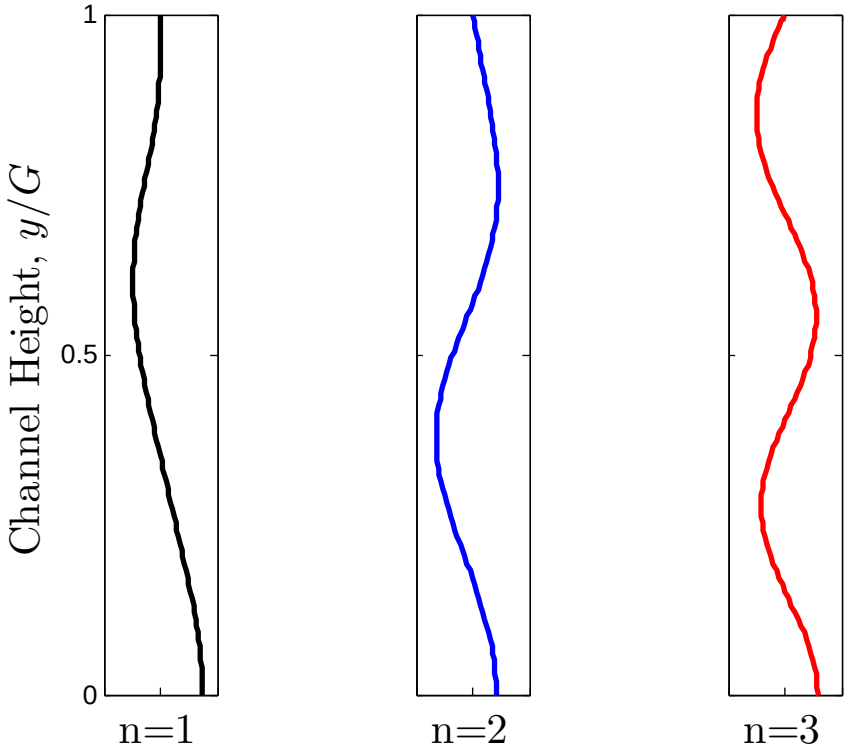

Figure 4.11: Interface shapes of first 3 modes for no-flow PN case for $L/G = 2$.

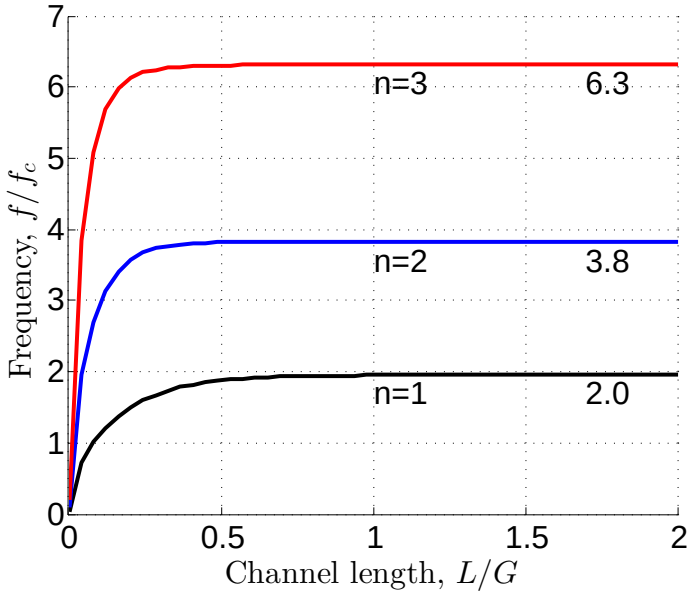

Figure 4.12: Scaled frequency versus channel length for no-flow PP case with asymptotes listed.

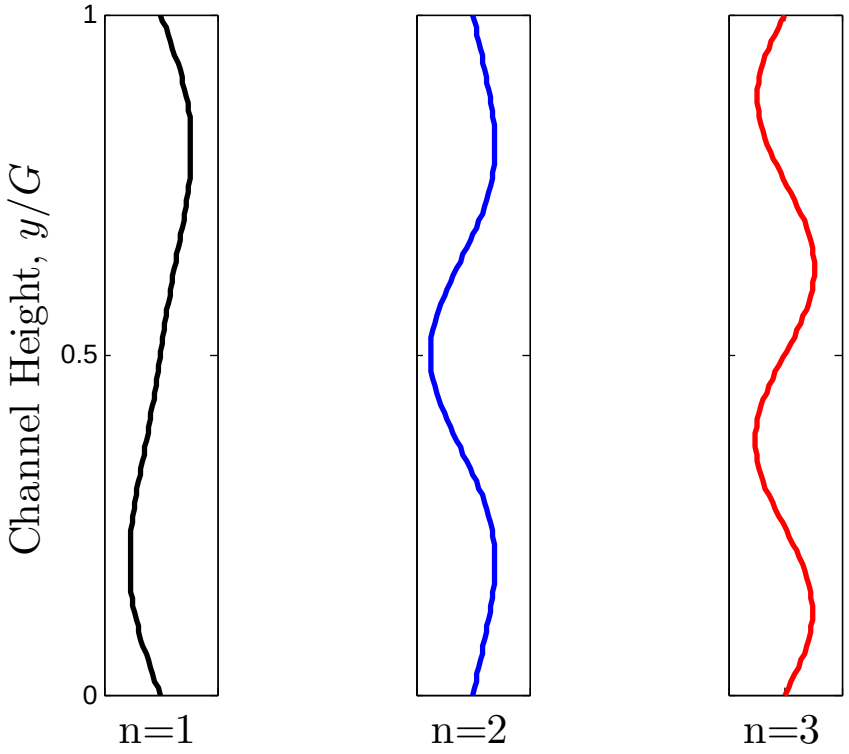

Figure 4.13: Interface shapes of first 3 modes for no-flow PP case for $L/G = 2$.

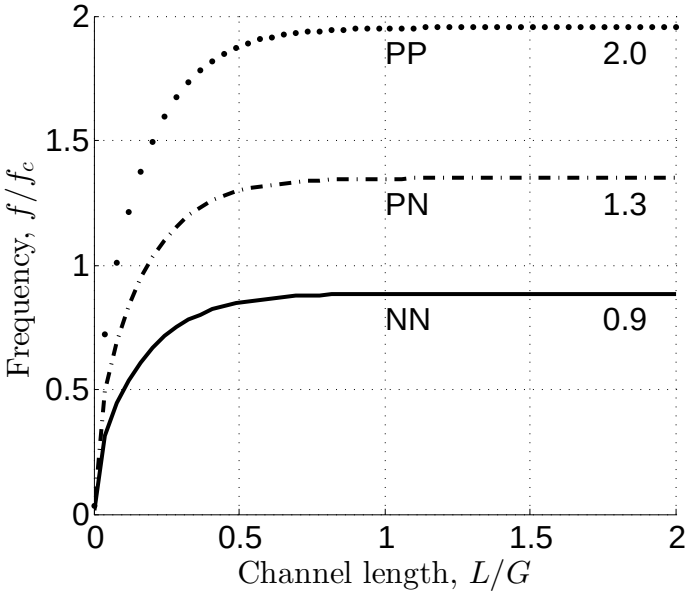

Figure 4.14: Scaled frequency ($n = 1$) versus channel length for no-flow NN, PN, and PP cases, with listed asymptotic values of 0.9, 1.3, and 2.0, respectively.

4.5.3 Base-flow NN, PN, PP

To introduce a dependence on the $We = \rho u_c^2 G/\sigma$, where $u_c = U$, base-flow must be present in the channel. The flat interface case with constant base flow are presented now for the NN, PN, and PP cases. The basis functions are the same as those used in the no-flow case, Table 4.4.

Here γ is allowed to be complex, $\gamma = b + i\omega$. It is found that the NN and PP cases are purely imaginary, $\gamma = i\omega$. *However, the PN case is found to have a real component b.* The NN frequency versus We is given in Figure 4.15 for $L/G = 2$. The frequency shows a power law dependence on the Weber number. At $We = 0$, the frequencies reduce to the zero base-flow values given in Section 4.5.2 as expected. The PP case, shown in Figure 4.16, is similar in appearance to the NN case.

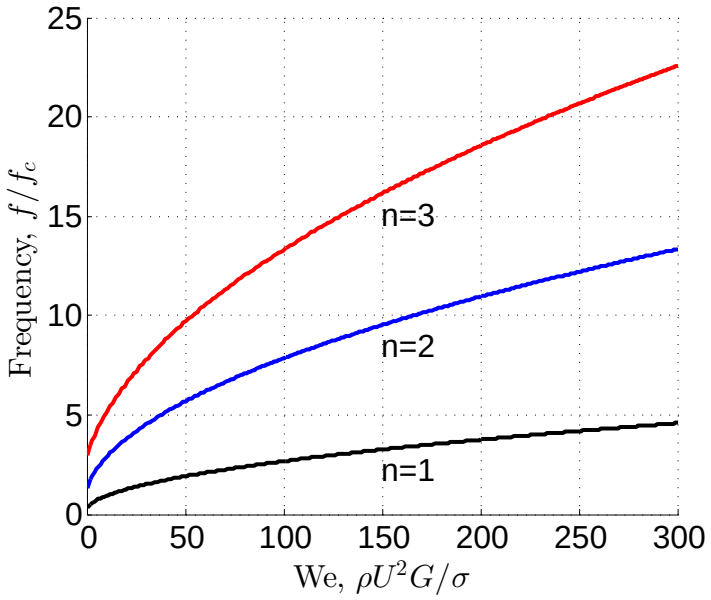

Figure 4.15: Scaled frequency versus We for base-flow NN case for $L/G = 2$.

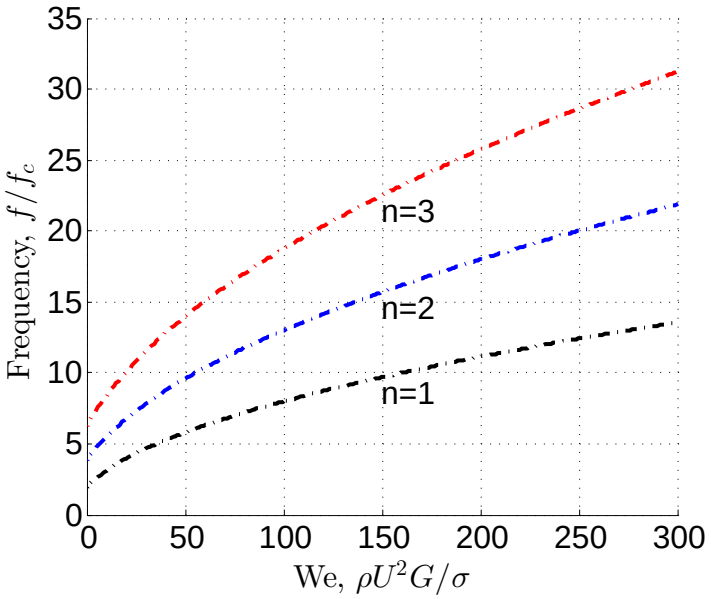

Figure 4.16: Scaled frequency versus We for base-flow PP case for $L/G = 2$.

Both the NN and PP boundary conditions are symmetric about the mid-gap plane, which is evident in Figures 4.9 and 4.13. The PN case however does not have such a symmetry. While this case was stable when there was no base-flow, the presence of base-flow results in an eigenvalue with imaginary *and* real component. The imaginary component is shown in Figure 4.17. The real component b is shown in Figure 4.18. The disturbance growth rate *increases* with We.

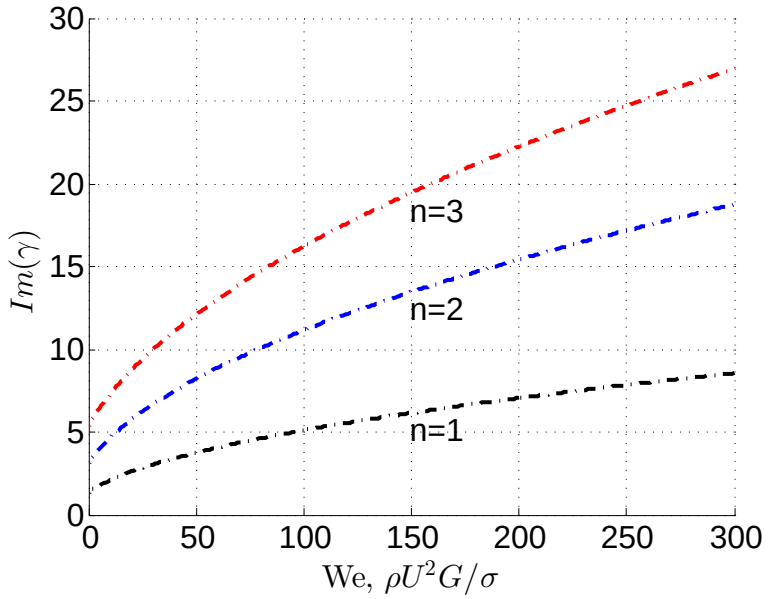

Figure 4.17: Frequency versus We for the base-flow PN case for $L/G = 2$.

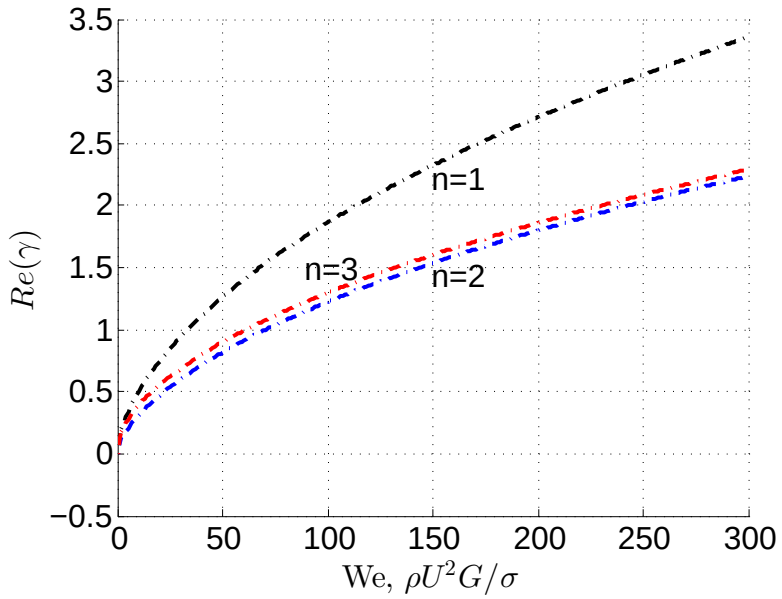

Figure 4.18: Instability growth rate versus We for base-flow PN case for $L/G = 2$.

4.5.4 Cylindrical base-state (no-flow)

Cylindrical coordinate system

The flat interface model problems have the advantage of simplicity, even having an analytical solution in the NN no-flow case. In addition, an analytical base-flow can be used to illustrate the effect on the frequency. However, the casting USM is typically closer to *cylindrical*. The same rectangular channel is considered, with three non-permeable walls, but now with a cylindrical base-state interface. The definition sketch is given in Figure 4.19.

Three cases will be considered: two fixed CA (FF), one fixed CA and one pinned

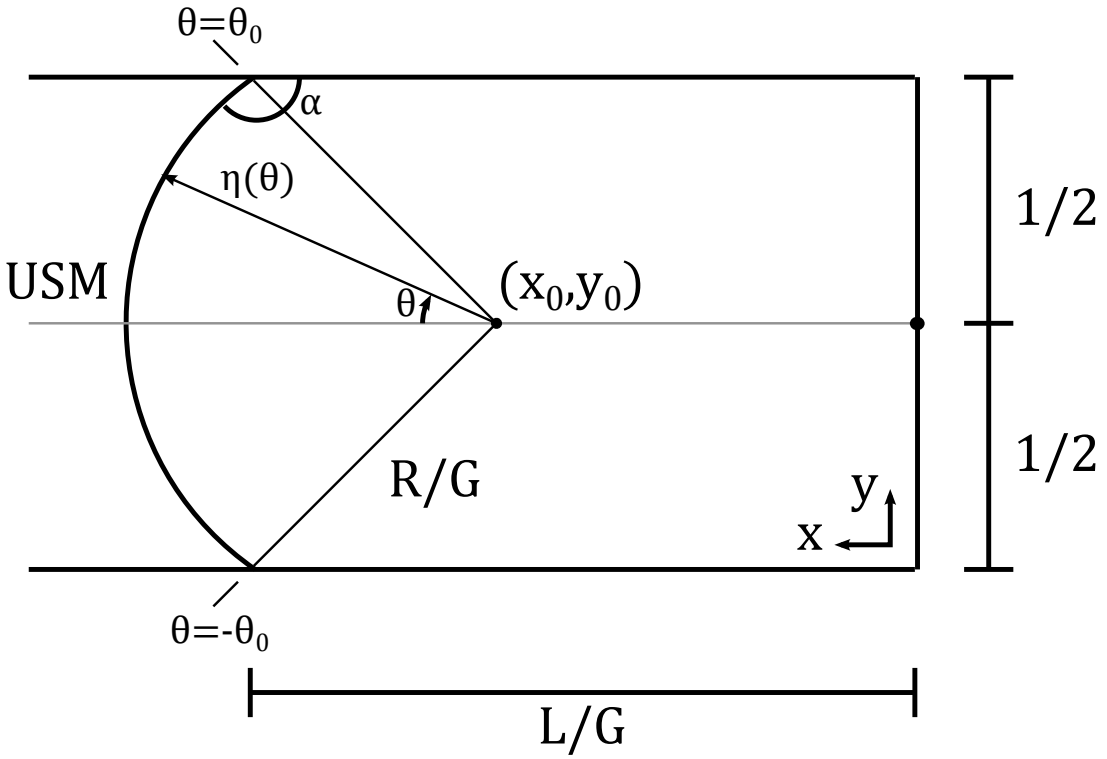

Figure 4.19: Definition sketch of a fluid in a rectangular channel with a cylindrical interface base-state USM. Extent of meniscus θ_0 is related to the contact angle α, $\alpha = \theta_0 + \pi/2$.

CL (PF), and two pinned CL (PP), illustrated in Figure 4.20. The case of base-flow will not be considered, as a tractable analytical base-state with the mixed cartesian and polar coordinates is not readily found.

A circular segment with origin (x_0, y_0) and radius R rests in the rectangular

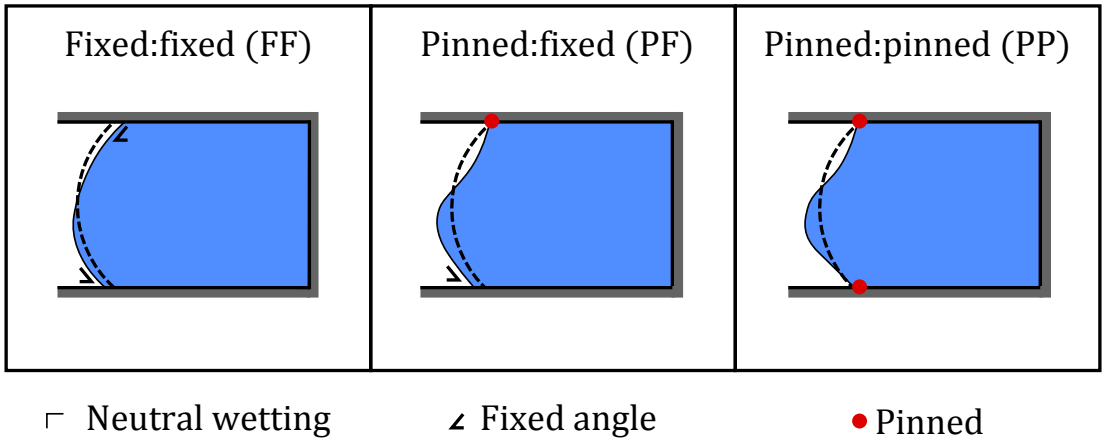

Figure 4.20: Three cylindrical base-states: two fixed CA (FF), one fixed CA and one pinned CL (PF), and two pinned CL (PP).

channel, shown in Figure 4.19. Polar coordinates are used to describe the interface, with a polar angle $-\theta_0 \leq \theta \leq \theta_0$, such that $\theta = 0$ is parallel to the x-axis and $\pm\theta_0$ is the angle at which the fluid makes contact with the wall. The contact angle $\alpha = \theta_0 + \pi/2$. The linearized equations are the same as given in Table 4.2. Here, $h_0 = R$, $K_0 = 1/R$, and $K_1 = (d^2h_1/d\theta^2 + h_1)/R^2$. In normal-modes reduced form, the kinematic and dynamic conditions are

$$\frac{\partial F}{\partial r} = \gamma\eta \tag{4.34}$$

$$\frac{\partial^2 \eta}{\partial \theta^2} + \eta = R^2\gamma F \tag{4.35}$$

where $\eta = \eta(\theta)$ and $F = F(x, y)$. The eigenvalue problem has mixed coordinates. In the channel, $F(x, y)$ must satisfy Laplace's equation, while at the interface, po-

lar coordinates are used.

Reduction to eigenvalue problem

In the flat case, a solution to Laplace's equation was found such that $F = F(\eta)$. Then, a series solution was assumed for η which was then used to approximate the eigenvales. In the cylindrical case, due to the added complication of having mixed coordinates, a different approach is taken (see Bostwick (2011) or Myshkis (1987)[5][58]. Here, η is eliminated from the eigenvalue problem. To do this, a Green's function is defined such that the dynamic condition 4.35 can be inverted

$$\int_{-\theta_0}^{\theta_0} G(s,\theta)\left[\frac{\partial^2 \eta}{\partial \theta^2} + \eta\right] ds = \eta = R^2\gamma \int_{-\theta_0}^{\theta_0} G(s,\theta)F(x,y)ds. \tag{4.36}$$

The Green's function is associated with the curvature operator, but must also have two boundary conditions associated with it. These will be discussed in the next section. First, the eigenvalue problem formulation is completed.

In general, equation 4.36 will *not* satisfy conservation of volume. However, because the gradient of F yields the velocity, a constant can be added to F without changing the velocity. Letting $F = C + F'$, equation 4.36 becomes

$$\eta = R^2\gamma \left[C \int_{-\theta_0}^{\theta_0} G(s,\theta)ds + \int_{-\theta_0}^{\theta_0} G(s,\theta)F'(x,y)ds\right].$$

Requiring $\int_{-\theta_0}^{\theta_0} \eta = 0$, the constant is found to be

$$C = -\int_{-\theta_0}^{\theta_0} G(s,\theta)F'(x,y)ds \Big/ \int_{-\theta_0}^{\theta_0} G(s,\theta)ds. \tag{4.37}$$

Finally, equation 4.36 can be combined with the kinematic condition to yield the eigenvalue problem

$$\frac{\partial F'}{\partial r} = R^2\gamma^2 \left[C \int_{-\theta_0}^{\theta_0} G(s,\theta) ds + \int_{-\theta_0}^{\theta_0} G(s,\theta) F'(x,y) ds \right]. \tag{4.38}$$

Now, a series form of F' is assumed such that its basis functions satisfy Laplace's equation and the no-penetration condition at the three walls. We let

$$F' = \sum_{n=1}^{k} c_k f_k(x,y) \tag{4.39}$$

$$f_k = a_k \cosh(k\pi x)\cos(k\pi y) \tag{4.40}$$

where a_k are normalization constants and c_k are unknown constants. a_k are chosen such that, on the flat interface, $\int_0^1 f_k(L,y) f_k(L,y) = 1$. Normalizing in this way is important for keeping the matrix elements in the numerical computation order 1 or smaller [58].

The series is inserted in equation 4.38. To reduce the problem to a matrix eigenvalue problem, an inner product with the jth basis function is taken

$$\int_{-\theta_0}^{\theta_0} (\cdot) f_j ds.$$

Note that, because of the mixed coordinates, equations relating x, y to θ are needed. According to Figure 4.19, these relations are

$$x = x_0 + R/G\cos(\theta) \tag{4.41}$$

$$y = y_0 + R/G\sin(\theta) \tag{4.42}$$

$$x_0 = L/G - \cot(\theta_0)/2 \tag{4.43}$$

$$y_0 = 1/2 \tag{4.44}$$

Boundary conditions and Green's functions

Like the flat case, the contact line can be constrained; either the contact angle can be forced to remain at its base-state value or the contact line can be pinned. Again, three cases will be considered: both contact angles fixed (FF), one contact angle fixed and one pinned contact line (PF), and both contact lines pinned (PP). Following an approach similar to that of Davis (1980) [24] for a rivulet, the boundary condition for a fixed contact angle is

$$\frac{d\eta}{d\theta} \pm \tan\theta_0 \eta = 0, \quad \theta = \pm\theta_0.$$

The boundary conditions for the three cases are given in Table 4.5. The Green's

Case	Boundary condition
FF	$[d\eta/d\theta \pm \tan\theta_0\eta]_{\pm\theta_0} = 0$
PF	$h\big\|_{\theta_0} = [d\eta/d\theta - \tan\theta_0\eta]_{-\theta_0} = 0$
PP	$h\big\|_{-\theta_0} = h\big\|_{\theta_0} = 0$

Table 4.5: Boundary conditions for the cylindrical base-state.

function for each of the cases are given in Table 4.6. Note that the PF and PP Green's functions are defined in the usual way. The FF case is a generalized Green's function, admitting infinitely many solutions.

Case	Green's Function
FF †	$\cos(\theta)\sin(t) - \cos(t)\sin(\theta) + Z(t,\theta) \quad -\theta_0 \leq t < \theta$
PF	$\cos(t)\sin(\theta_0 - \theta)/\cos(\theta_0) \quad -\theta_0 \leq t < \theta$
PP	$\sin(t + \theta_0)\sin(\theta_0 - \theta)/\sin(2\theta_0) \quad -\theta_0 \leq t < \theta$

Table 4.6: Green's functions for the cylindrical base-state problems. $Z \equiv [t\cos(\theta)\sin(t) + \theta\cos(t)\sin(\theta)]/[\theta_0 + \sin(\theta_0)\cos(\theta_0)]$. † Generalized Green's function with θ and t are exchanged for $\theta < t \leq \theta_0$. $Tan(\theta_0)$ is an eigenvalue of the curvature with FF boundary conditions, so there are infinitely many solutions.

Vibration of curved interfaces

The eigenvalues for all cases were found to be purely imaginary, $\gamma = i\omega$. Two parameters, L/G and base-state polar angle θ_0, can be varied. The three cases were found to exhibit very different frequencies as contact angle was varied. Note that in all plots of frequency versus θ_0, as θ_0 approaches 0°, the flat, no-flow results discussed above are recovered.

Case (FF) frequency is shown versus θ_0 for the first 4 modes and $L/G = 2$ in Figure 4.21. The first mode is shown to *increase* frequency with θ_0, while all higher modes *decrease*. This particular case was solved by Myshkis, and we find identical results [58]. Figure 4.22 shows the variation of frequency with L/G for various θ_0. As frequency increases with θ_0 for $n = 1$, the curves resemble those in Figure 4.8, approaching steady values for $L/G > 0.5$ For $n > 1$, there is crossing of the frequency curves for small L/G.

The (PF) frequency is shown in Figure 4.23. Here, all modes show an increase

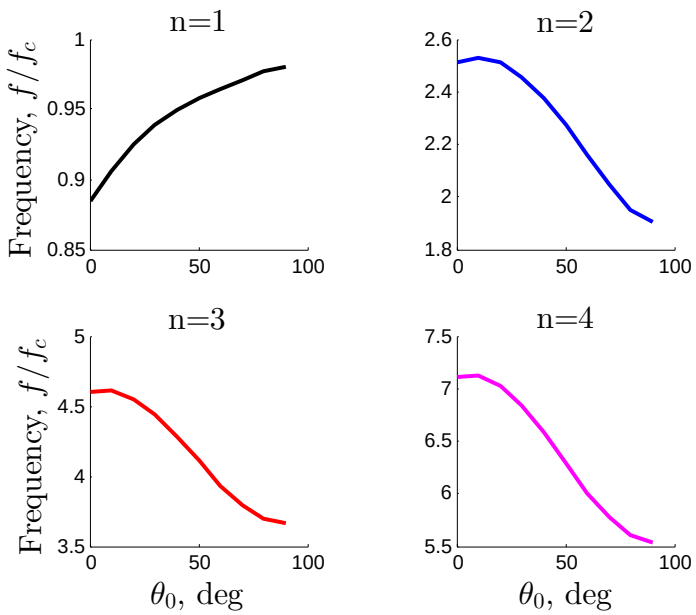

Figure 4.21: Cylindrical FF: scaled frequency versus θ_0 for $L/G = 2$.

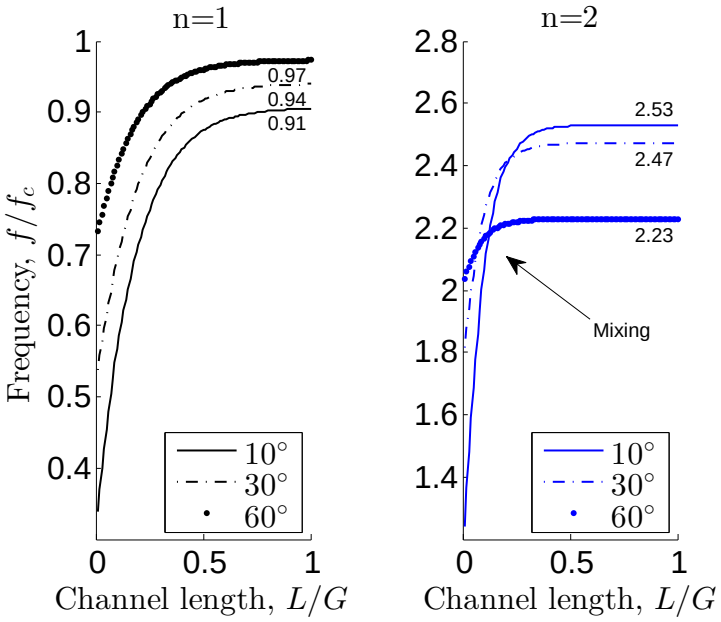

Figure 4.22: Cylindrical FF: scaled frequency versus channel length for various θ_0. Asymptotic values are shown.

in frequency with θ_0, with the most rapid increase as θ_0 approaches 90°. The fre-

quency versus L/G curves, shown in Figure 4.24, rapidly approach constant values for $L/G > 0.5$. The (PP) frequency is shown in Figure 4.25. Here, all modes

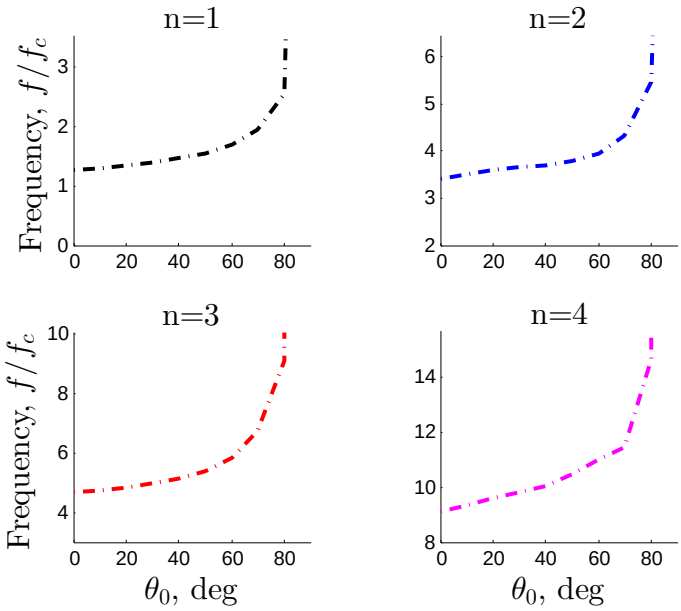

Figure 4.23: Cylindrical PF: scaled frequency versus θ_0 for $L/G = 2$.

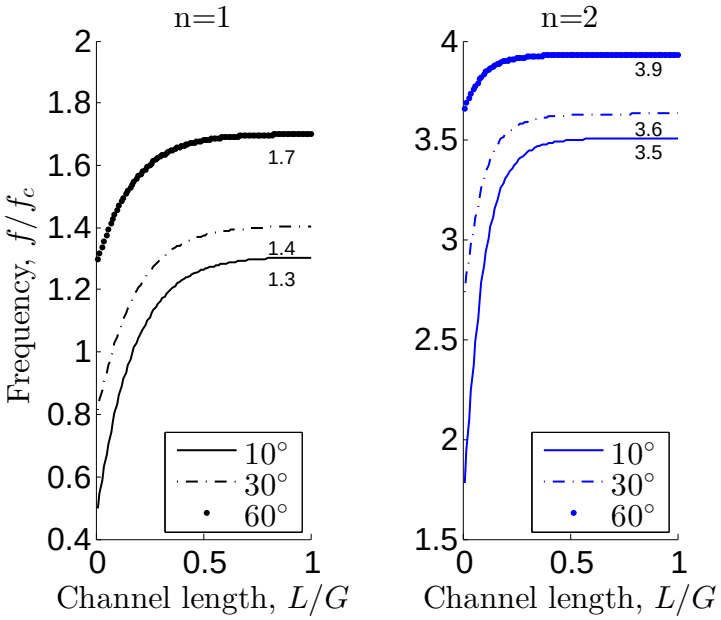

Figure 4.24: Cylindrical PF: scaled frequency versus channel length for various θ_0. Asymptotic values are shown.

show a decrease in frequency with θ_0. The frequency versus L/G curves, shown in Figure 4.26, rapidly approach constant values for $L/G > 0.5$. Like the fixed θ_0 cases, there is crossing of the frequency curves for small L/G.

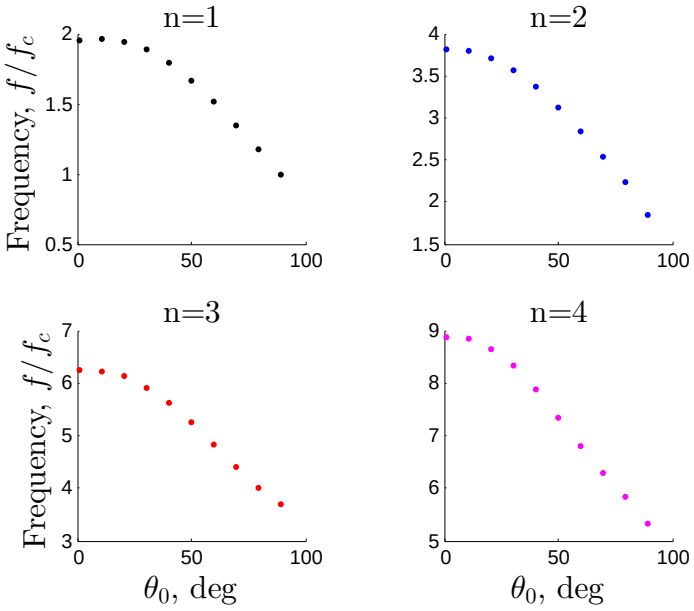

Figure 4.25: Cylindrical PP: scaled frequency versus θ_0 for $L/G = 2$.

4.6 Comparison with data and discussion

Nine cases have been considered. The results are summarized.

- Flat interface with no base-flow: The only free parameter is channel length L/G. For all contact line conditions, the asymptotic value of frequency is approached for $L/G > 0.5$. The NN case is the *natural* case, admitting an analytical solution. Constraining one (PN) or both contact (PP) lines raises the frequency.

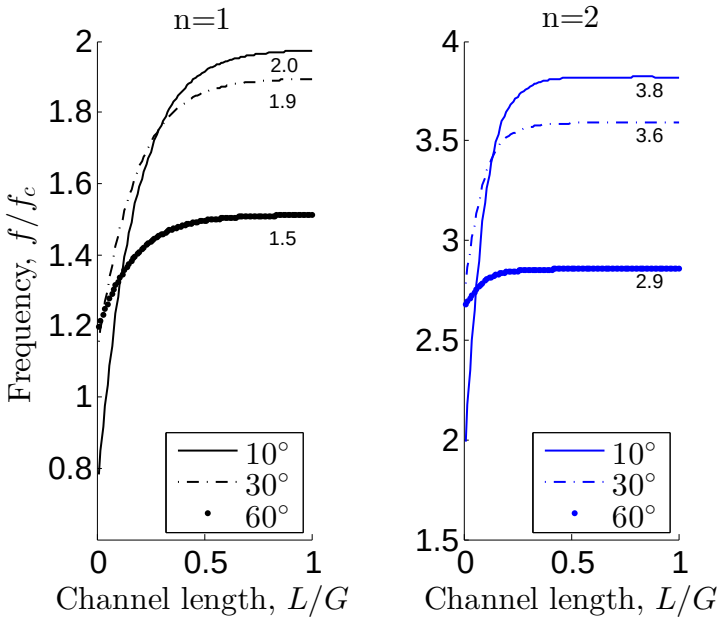

Figure 4.26: Cylindrical PP: scaled frequency versus channel length for various θ_0. Asymptotic values are shown.

- Flat interface with constant vertical base-flow: The presence of flow introduces a second parameter, We. Increasing We raises the frequency for all contact line conditions. The NN and PP cases have purely imaginary eigenvalues, while the PN case has complex ones for all $We > 0$. This real growth rate for the PN case suggests instability.

- Cylindrical interface with no base-flow: The free parameters are L/G and angle θ_0. All cases considered were found to have purely imaginary eigenvalues. All cases approach asymptotic values, for $L/G > 0.5$. For large L/G ($L/G = 2$), the FF frequency increased with contact angle for $n = 1$, but achieved a maximum near $0°$ for $n > 1$ and then decreased in value. For the PF cases, frequency always increased with contact angle α for all modes, where $\alpha = \theta_0 + \pi/2$. The PP case always decreased with contact angle for all modes. For smaller L/G, there is crossing of the frequency curves plotted against L/G for various contact angle.

The goal is to use model problems to shed light on the observations. The results are now compared with the data. Recall that the CW feature has $f = 2.1 f_c$. Since the USM is observed experimentally to be cylindrical, we turn to the cylindrical FF case. Plotting the frequency versus contact angle ($\alpha = \theta_0 + \pi/2$) for the $n = 2$ mode with $L = 2$ in Figure 4.27, it is seen that the frequency equals the CW frequency around $\alpha = 150°$. Byrne, et al. report, a typical value is 150° [12]. Scaled CW data are plotted against the We_U (showing no We_U dependence), with the cylindrical FF, $n = 2$ case model prediction in Figure 4.28 (reproduced CW data from Figure 4.4).

The introduction of vertical base-flow in the channel introduces We dependence.

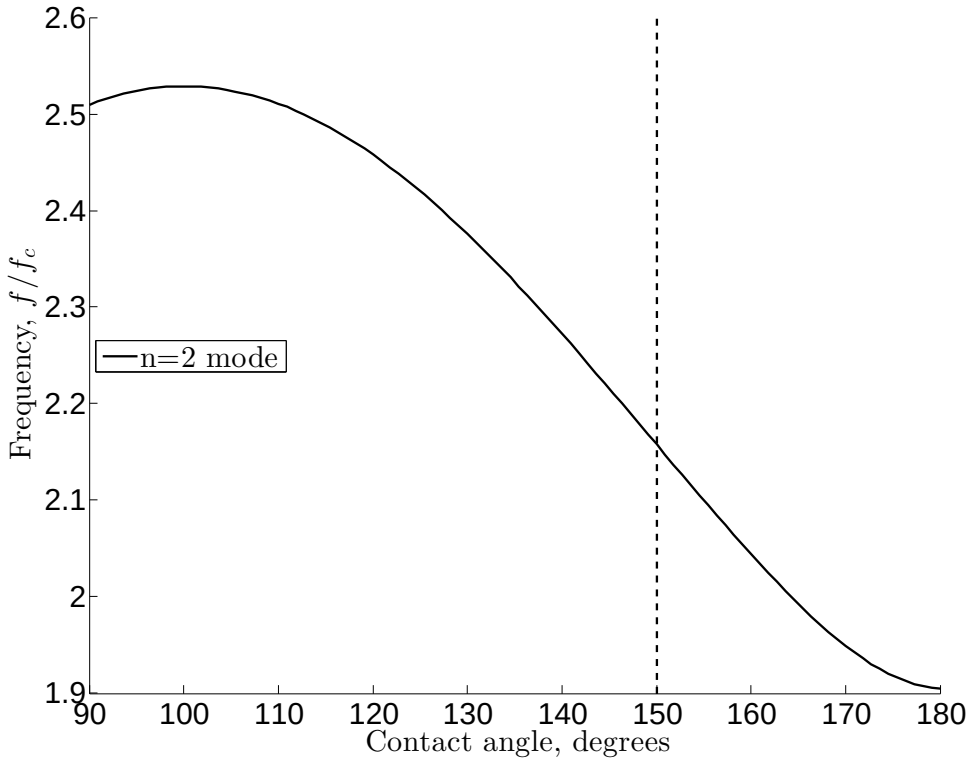

Figure 4.27: Variation of frequency with contact angle for FF, $n = 2$ case with $L = 2$. Typical observed USM contact angle is 150° (dashed line).

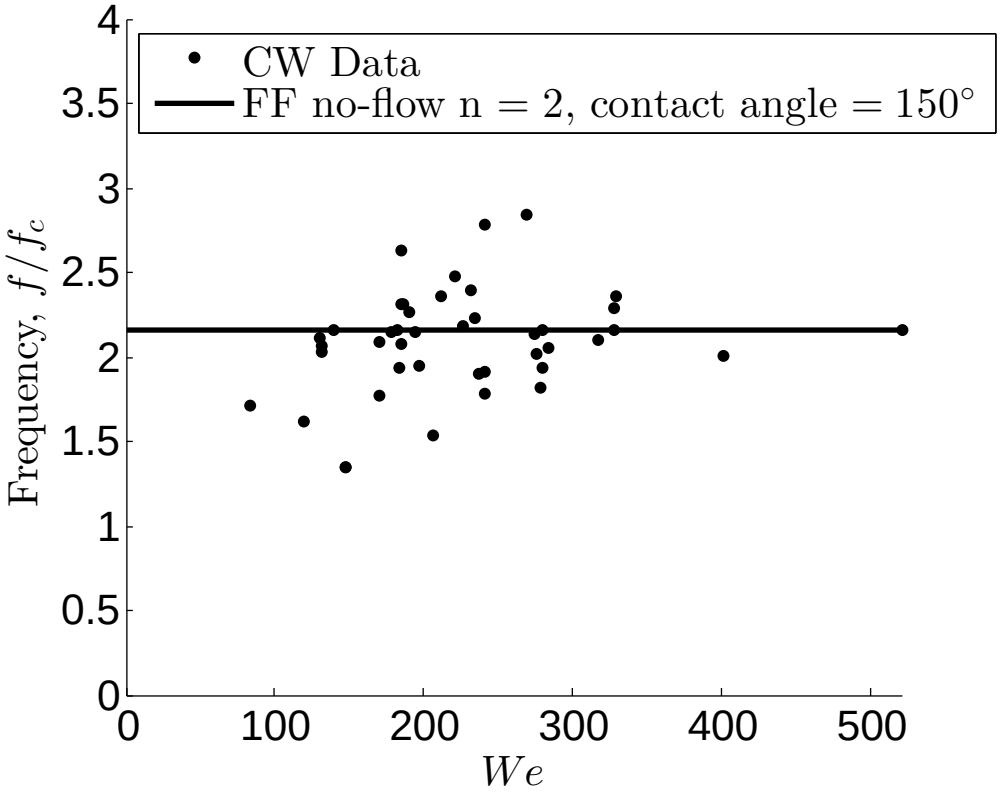

Figure 4.28: CW frequency data plotted versus We_U with model prediction from FF, $n = 2$ case with $L = 2$. Reproduced CW data of Figure 4.4.

In Cox and Steen, the We used is based on the wheel-speed U. The model prediction for NN base-flow, $n = 1$ case f versus We and HB data are plotted for We_U in Figure 4.29. The model frequency increases faster than the data. Not only does the model have poor agreement with the data, using the wheel-speed as the characteristic velocity does not make physical sense, as the flow past the interface is more closely the inlet velocity $u_{in} = TU/B$. Typically, $u_{in} \approx 1\ m/s$, 10 times smaller than the wheel speed. Flow in the puddle is an order of magnitude smaller than the wheel speed, so on this basis, we conclude that *the flow model can not capture the wheel-speed dependence of the HB data.*

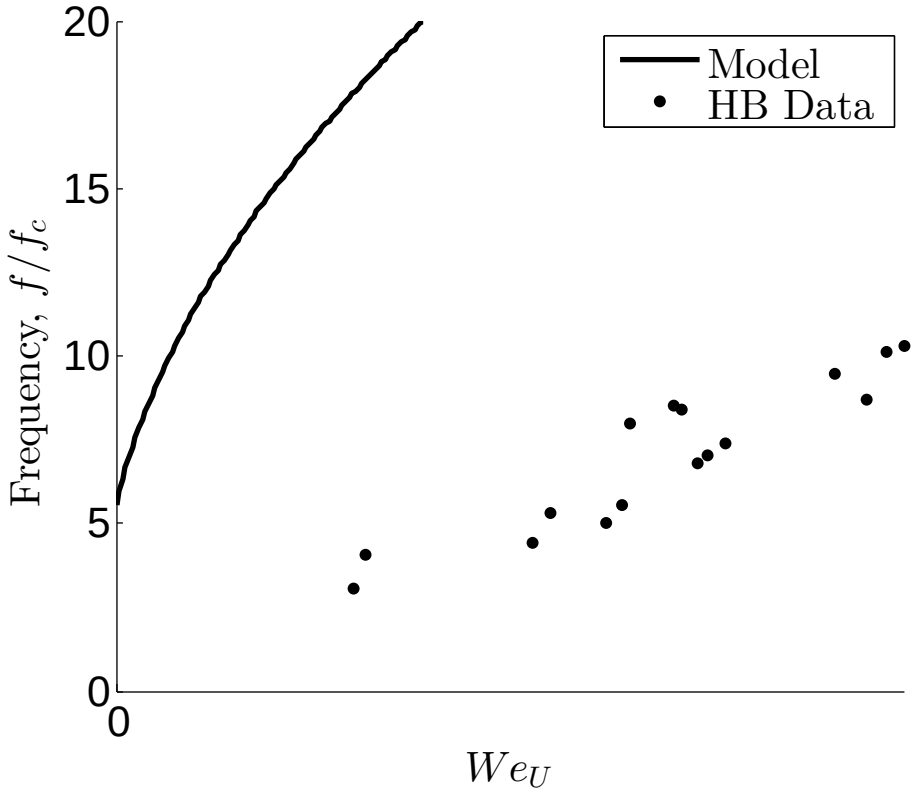

Figure 4.29: Variation of frequency with three different Weber numbers for the NN case with base-flow: We_U, We_{uin}, and We_{eff}, plotted with HB data. We_{eff} provides the closest agreement, but with an unexplained offset in frequency.

4.6.1 Herringbone and stick-slip model

The flow past the interface is an $\approx 0.1U$, and the model predictions for flow past an interface greatly overpredict the HB frequency. It is possible, however, to introduce U dependence with a stick-slip model. Suppose that, upon solidification, the lower contact line 'sticks' to the wheel and translates with speed U. Recall that for HB formation, the upper contact line is fixed. This is represented schematically in Figure 4.30. For simplicity, a flat interface is considered, initially having a contact angle $\alpha = \pi/2$ with the wheel. As the lower contact line translates, α increases. Ignoring the surface-tension between the solid and the gas, a contact-line force

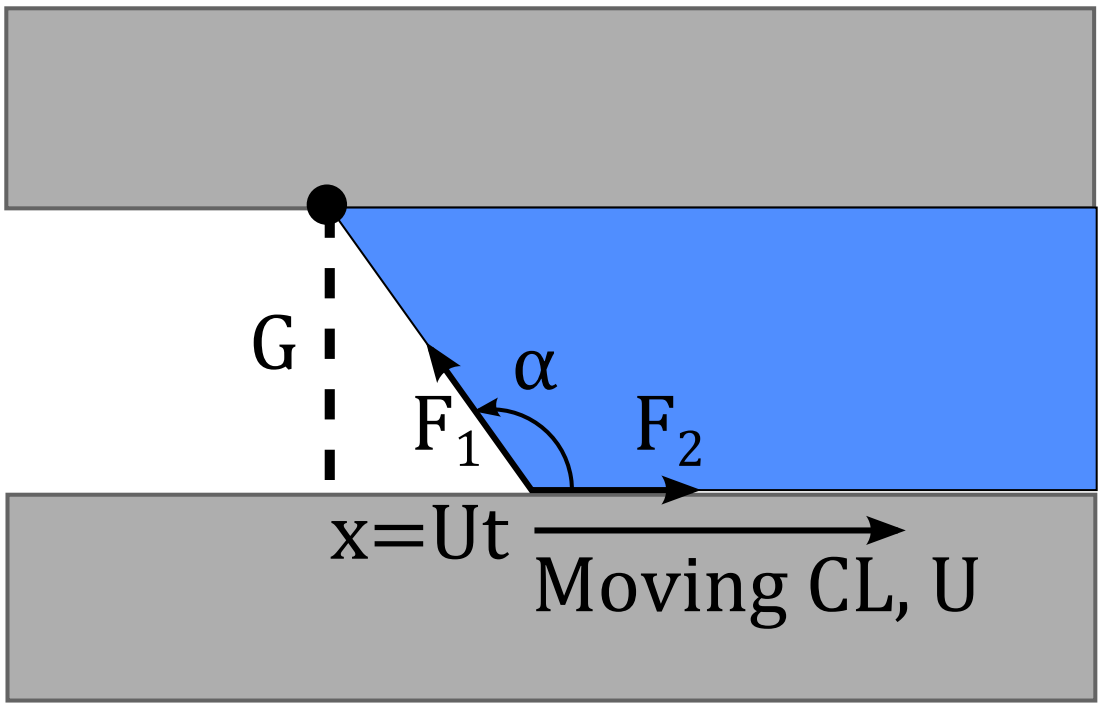

Figure 4.30: Schematic of a contact line stick-slip model. The upper contact line is pinned. Upon solidification, the lower contact line sticks to the wheel and tranlates with speed U.

balance can be made according to the Young-Dupre equation

$$F_2 + F_1 \cos(\alpha) = 0 \tag{4.45}$$

where F_2 is the liquid-solid force, and F_1 is the liquid gas force. At any instant, the interface forms a right triangle with height G and base $x = Ut$. Scaling $t \sim (\rho G^3/\sigma)^{1/2}$, it is found that

$$\tan(\pi - \alpha) = \frac{1}{We_U^{1/2} t}. \tag{4.46}$$

Suppose that the lower contact line sticks until the contact angle reaches a critical value α_c, and then instantaneously slips back to its flat, undisturbed shape. Allowing this even to repeat periodically, the frequency $f = 1/t_c$, where t_c is the time required for $\alpha = \alpha_c$. A stick-slip frequency is found to be

$$f = We_U^{1/2} \tan(\pi - \alpha_c). \tag{4.47}$$

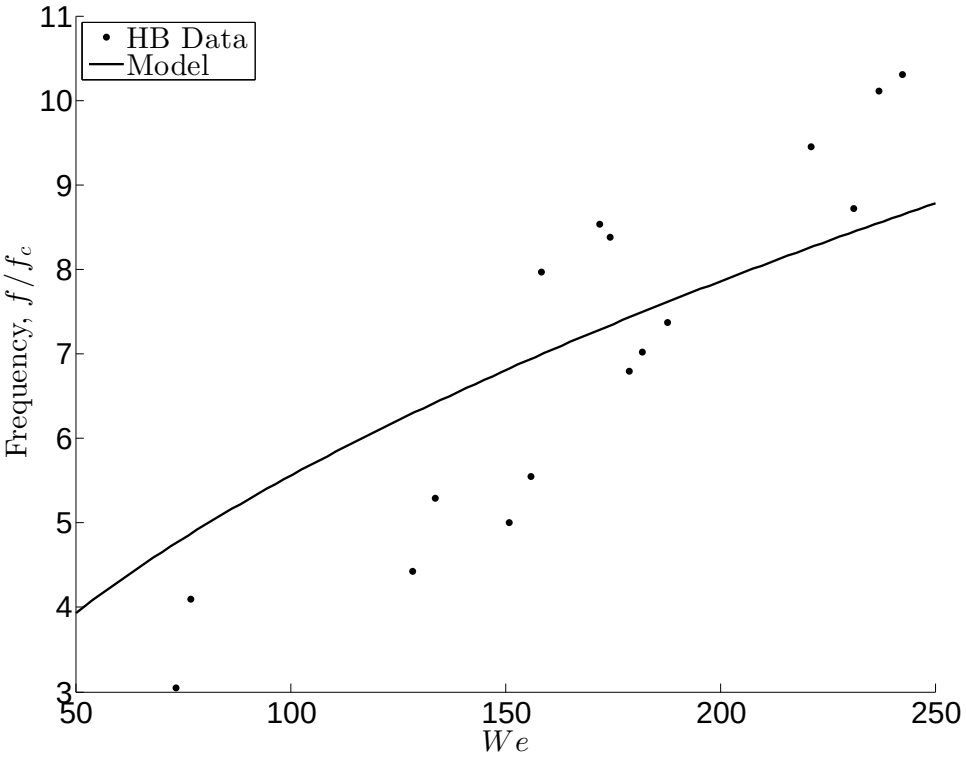

Figure 4.31: Stick-slip model fit to the HB data for $\alpha_c = 150°$.

Supposing that the contact line translates with the wheel until it reaches a critical contact angle α_c, Equation 4.47 can be fit to the herringbone data to find α_c. The best-fit, shown in Figure 4.31 was found for $\alpha_c = 150°$. The stick-slip approach has introduced a We_U dependence and gives reasonable agreement with the data.

CHAPTER 5

CASTING LAB UPDATE

5.1 Surface roughness analysis

The surface topology of ribbon at the micron scale was examined by Byrne et al. (2006) and Cox and Steen (2013). Periodic defects were examined using optical profilometry in these publications. A scan of the crosswave defect, originally presented in Byrne, et al. (2006)[12] and reproduced from Cox (2011) [21], is shown in Figure 5.1a. Discrete dimples thought to be caused by entrained air pockets are visible on the wheel side. Labeled in the figure is a dimple with 30 μm magnitude. The entrained air acts as an interuption to heat-transfer, resulting in thickness depressions, appearing as trenches on the air-side. In the scan shown, the air-side depression was on the order of 50 μm. Similarly, a scan of the herringbone defect, presented in Cox and Steen (2013)[20] and reproduced from Cox (2011)[21], is shown in Figure 5.1b. Again, discrete pockets are visible on the wheel-side, but in contrast to the crosswave defect, a well defined trench on the air-side is less apparent. The maximum wheel-side dimple is 28 μm, and other smaller dimples are present. These two studies were the only to examine the surface texture of the cast ribbon. Here we discuss the use of a borrowed surface roughness analyzer to have a preliminary look at ribbon and wheel surface texture.

In the summer of 2011, a Mitutoyo portable surface roughness analyzer (SRA) was lent by Metglas. The SRA drags a diamond-tipped mechanical stylus a distance of 4 mm across the surface being analyzed, as shown in Figure 5.2. The vertical deflection of the stylus as a function of horizontal position is stored. The

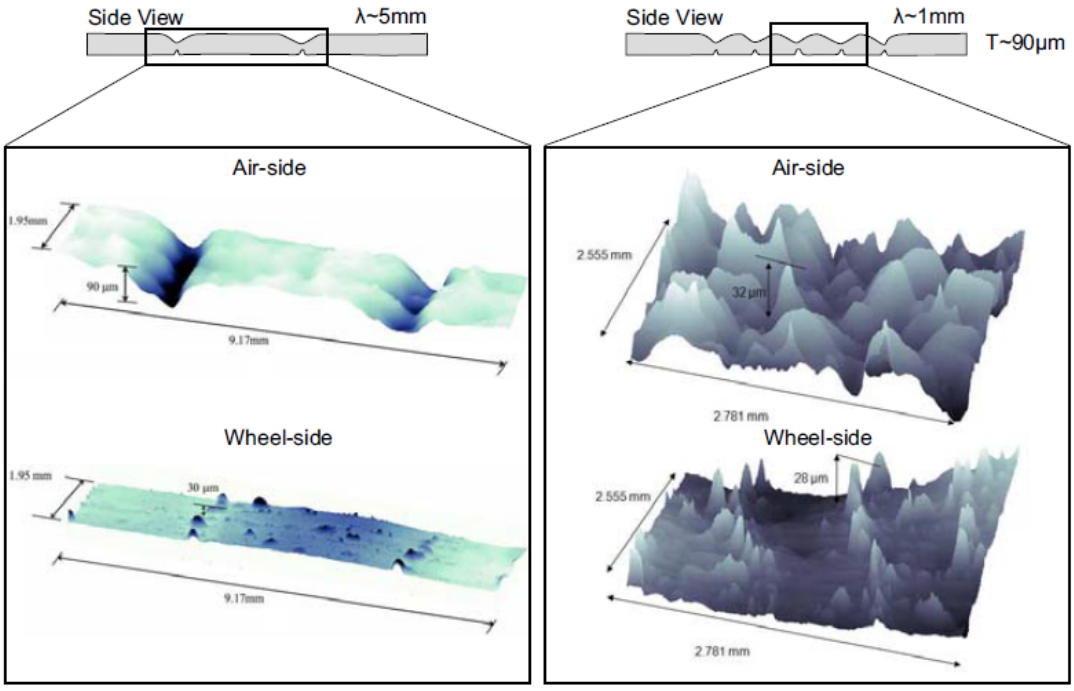

Figure 5.1: Optical profilometry scans of the ribbon wheel- and air-side for a) cross-wave defect and b) herringbone defect. Reproduced from Cox thesis (2011)[21].

data are collected by the insturment, and printed. The SRA was used on various ribbon pieces and on the wheel substrate.

One goal of this study was to determine if the SRA could be used to generate ribbon profiles like those measured by optical profilometry. A profile obtained by SRA of the wheel-side of a piece of ribbon with the herringbone defect is shown in Figure 5.3, upper. The scan shows 5 deviations from the nearly flat base-line, corresponding to 5 herringbone defects on the ribbon. The magnitude of these deviations ranges from $8 - 21\ \mu m$. These are on the same order as the profilometry scans of the herringbone, wheel-side dimples in Figure 5.1. Although the SRA yields 2-dimensional profiles which qualitatively resemble the profilometry scans,

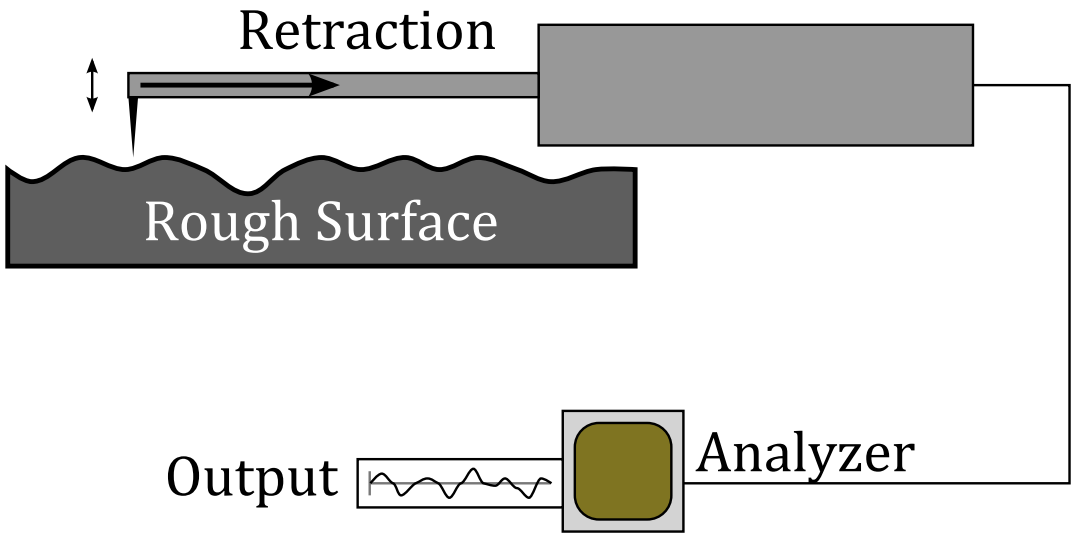

Figure 5.2: Schematic of Mitutoyo portable surface roughness analyzer (SRA). A diamond-tipped mechanical stylus is dragged across a surface and its vertical deflection is recorded as a function of horizontal position.

creating 3-dimensional profiles is difficult. The stylus is only free to move vertically and in *one* horizontal direction. To construct a 3-dimensional profile requires assembling multiple SRA scans. To do so, the ribbon must be moved relative to the stylus. Precisely controlling the position of the ribbon as it is moved is difficult and was not successfully completed. Fabrication of an apparatus to control this process is likely possible, but was not done.

Another goal of this study was to quantify the 'roughness' of the ribbon and substrate. Figure 5.3, lower, is a scan of a CuBe substrate. The substrate shown in the figure appears flat relative to the herringbone scan. To quantify the degree of 'flatness', a roughness factor f_R is defined as

$$f_R \equiv \frac{\sum_{n=1}^{N-1} \sqrt{(x_{n+1} - x_n)^2 + (y_{n+1} - y_n)^2}}{\sum_{n=1}^{N-1} (x_{n+1} - x_n)}. \tag{5.1}$$

where N is the number of data points saved by the instrument, and x_j and y_j are the horizontal and vertical positions of the j^{th} data point. Thus, f_R represents the

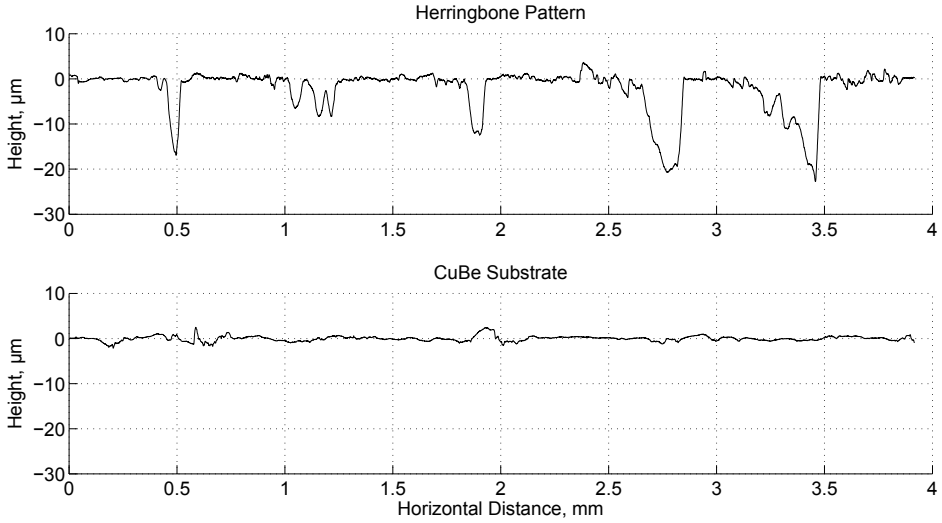

Figure 5.3: Upper: Ribbon wheel-side exhibiting herringbone defect; Lower: CuBe substrate

total horizontal and vertical distance traversed by the stylus relative to the horizontal 'length' of the sample. A perfectly flat sample would have $f_R = 1$. Any vertical motion of the stylus results in $f_R > 1$. Table 5.1 summarizes the samples analyzed, including crosswave and herringbone samples, 'smooth' defect-free samples, and a CuBe block polished with 150 and 400 grit sandpaper (note: 150 grit is the typical grit used for polishing the wheel). The f_R reported in Table 5.1 are all very nearly unity; deviations from the flat case are seen in the second decimal place of f_R with the exception of the air-side scan of $CJSU09\_37$. This is not surprising, as vertical deviations are on the μm scale while the total horizontal distance traversed by the stylus was 4 mm. The air-side scans had f_R values greater than the corresponding wheel-side scans. As air is entrained on the wheel-side, heat-transfer to the wheel is reduced, resulting in a thickness depression on the air-side. However, the metal which did not solidify in that region is still present in the puddle, and it is typical to see this metal solidified on either side of the air-side defect. This creates a surface with large 'roughness' relative to the wheel-side counterpart. The 'smooth'

Cast ID	Piece No.	Ribbon side	Defect	No. Defects	f_R	Comment
$CJSU09\_37$	56	W	HB	4	1.0612	
$CJSU09\_37$	56	A	HB	4	1.2142	Split
$CJSU09\_37$	56	W	CW	1	1.0182	nozzle
$CJSU09\_37$	56	A	CW	1	1.2268	cast
$ACSU09\_17$	57	W	HB	5	1.0213	
$ACSU09\_17$	57	A	HB	5	1.0317	
$ACSU10\_13$	10	W	HB	5	1.0129	High freq.
$ACSU10\_13$	10	A	HB	5	1.0218	HB
$CDSU07\_47$	61	W	-	-	1.1077	'Smoothest' cast
$ODSU06\_35$	69	W	-	-	1.0095	Smooth cast
$ODSU06\_35$	69	W	-	-	1.0039	
CuBe Block	-	-	-	-	1.0325	150 grit
CuBe Block	-	-	-	-	1.0327	150 grit
CuBe Block	-	-	-	-	1.0160	400 grit

Table 5.1: Summary of samples analyzed using SRA. W: wheel-side; A: air-side; HB: herringbone; CW: crosswave.

ribbons were ones with no visible periodic defect. $CDSU09\_47$ is regarded as the 'smoothest' ribbon produced in the casting lab, but its f_R is anomalously larger than many of the ribbons where defects were present. $ODSU06\_35$ was also a defect-free cast, with the lowest f_R values observed in this study.

A CuBe block was also scanned. The purpose was to determine if there was 'mating' between the substrate and ribbon wheel-side. The 150 grit samples had $f_R \approx 1.033$, similar to the values for wheel-side ribbon scans. Figure 5.4 shows a 'smooth' ribbon scan and a CuBe scan. It is evident that the frequency of the roughness of the CuBe block is greater than the ribbon, but the amplitude of the roughness is greater for the ribbon. Though the samples have similar f_R, there is no obvious templating of the wheel roughness into the ribbon. The solidification event rectifies the ribbon roughness.

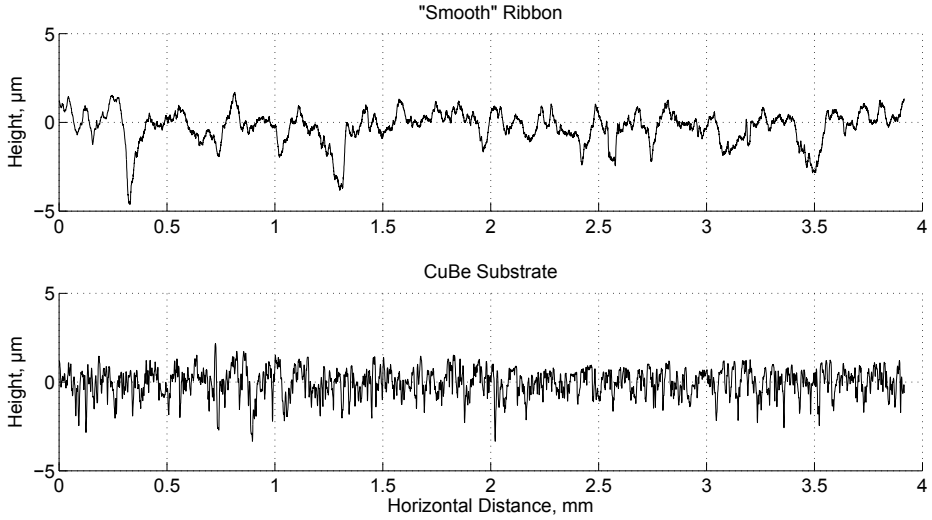

Figure 5.4: Wheel-side scan of 'smooth' ribbon (above) and CuBe substrate (below) polished with typical 150 grit sandpaper.

5.2 Wire casts

As discussed in Chapter 4, the appearance of periodic features can influence the quality of the final ribbon product. These features arise as a result of capillary vibrations of the USM. As a means of altering the frequency of these features, a horizontal wire was brought into contact with the puddle in experiments during Summer 2012. It is well-known that constraining a free interface can increase the vibrational frequency. Strani examined the vibrations of a spherical drop in partial contact with a solid surface [70]. Bostwick and Steen (2009) modeled the axis-symmetric vibration of a spherical drop with a circular ring surrounding it [4]. Prosperetti (2012) considered point constraints on interfaces with various geometries [63]. Motivated by these findings, a wire was introduced parallel to the wheel surface, extending along the USM to act as a 'line constraint' to the mensicus motion, especially motions in the streamwise direction, Figure 5.5.

The wire was stretched along the back of the puddle, Figure 5.5. The wire was fastened to a fixed plate on either side of the puddle and held taught by two bolts. The wire was made of steel, chosen to have a diameter much smaller than the gap. Positioning the wire vertically was challenging, but the goal was to have it suspended at half the gap height above the wheel. A photograph of the stretched wire is shown in Figure 5.6. One of the two side-plates and bolts used to fasten the wire are seen in Figure 5.7.

Whether the USM made contact with the wire was dependent on the puddle length and the upstream position of the wire relative to the nozzle opening. Contact was confirmed by high-speed video analysis of the puddle. Figure 5.8 shows a single image from a cast with no wire and a cast where contact was made with

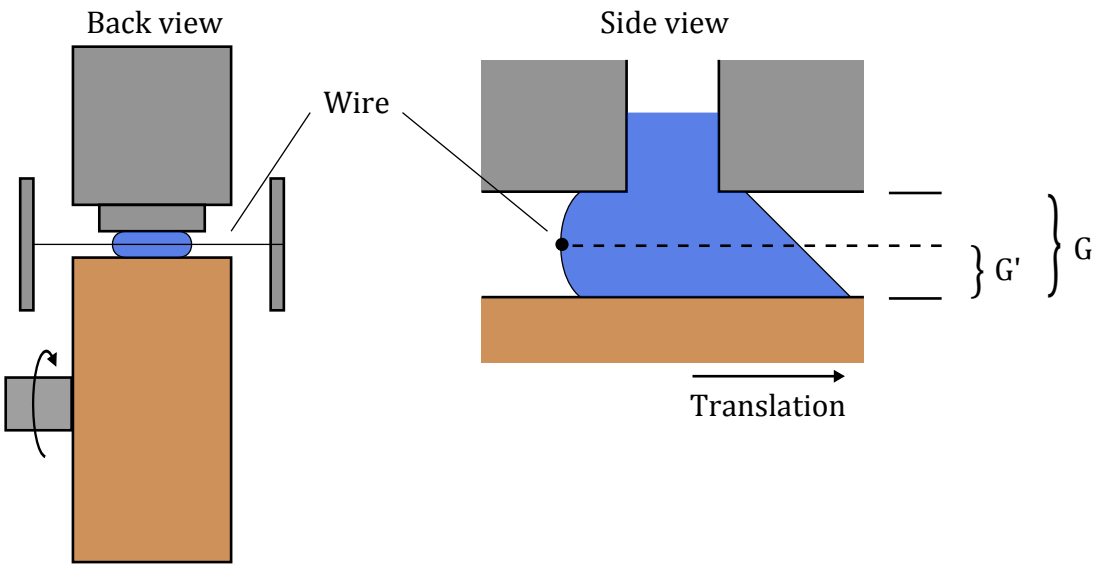

Figure 5.5: Schematic representation of a wire stretched along the back of the puddle. The wire was fastened to two side plates on either side of the wheel. The wire made contact with upstream mensicus. The distance of the wire to the nozzle G' was approximately half of the gap height G.

the wire. The cast with no wire allows the USM to take on a typical cylindrical shape. However, the wire created a 'kink' in the USM.

Twenty wire casts were performed. Some casts produced ribbon with the crosswave features, while others had herringbone. The number of features appearing on 15 cm segments of the cast ribbon were counted and related to a frequency using the wheel speed. As discussed in Chapter 4, the two features can be distinguished by plotting the defect frequency scaled by $f_c \equiv (\sigma/\rho G^3)^{1/2}$ versus $We \equiv \rho U^2 G/\sigma$ (note: this We definition is consistent with Cox and Steen[20], but differs by a factor of 1/2 from Chapter 4). Crosswave data correlate with a line of zero-slope and intercept of 2.1, indicating no We dependence, while herringbone correlate with slope 0.08 and zero-intercept, Figure 4.4.

The plot of the crosswave feature frequency versus We is shown in Figure 5.9

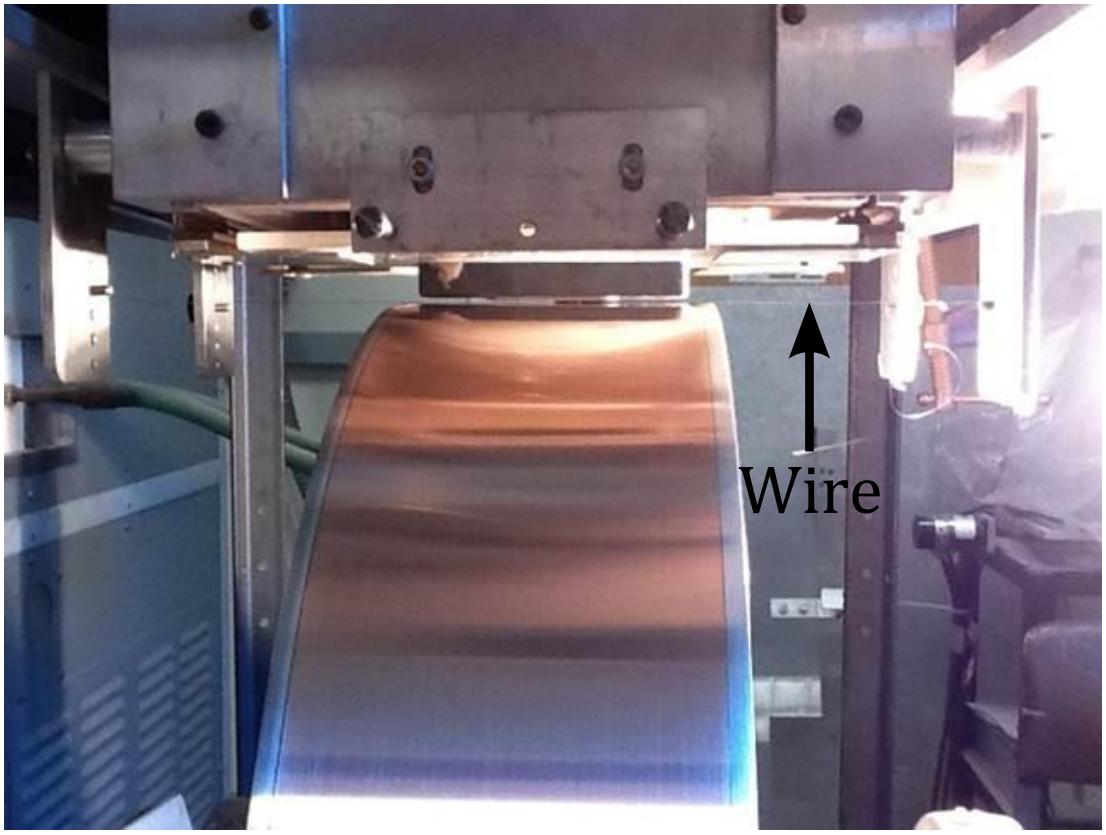

Figure 5.6: Photograph of the wire stretched along the back-side of the nozzle viewed from the front of the apparatus, i.e. looking upstream (against the casting direction).

for wire and no-wire casts. Here, EAT/MG data are collected from experiments reported in Theisen, et al. (2007) and data provided by MetGlas. The BLC CW line is the 'best-fit' line given in Cox and Steen (2013). Red circles are from wire casts. There is considerable scatter about the BLC line. However, the wire casts fall within the range of the non-wire data, with the exception of one outlier (scaled frequency ~ 3.6). There is no obvious effect of the wire on CW, as some data fall above and some below the BLC line.

A plot of the herringone feature frequency versus We is shown in Figure 5.10. EAT/MG herringbone data were not available. Instead, data from Cox and Steen

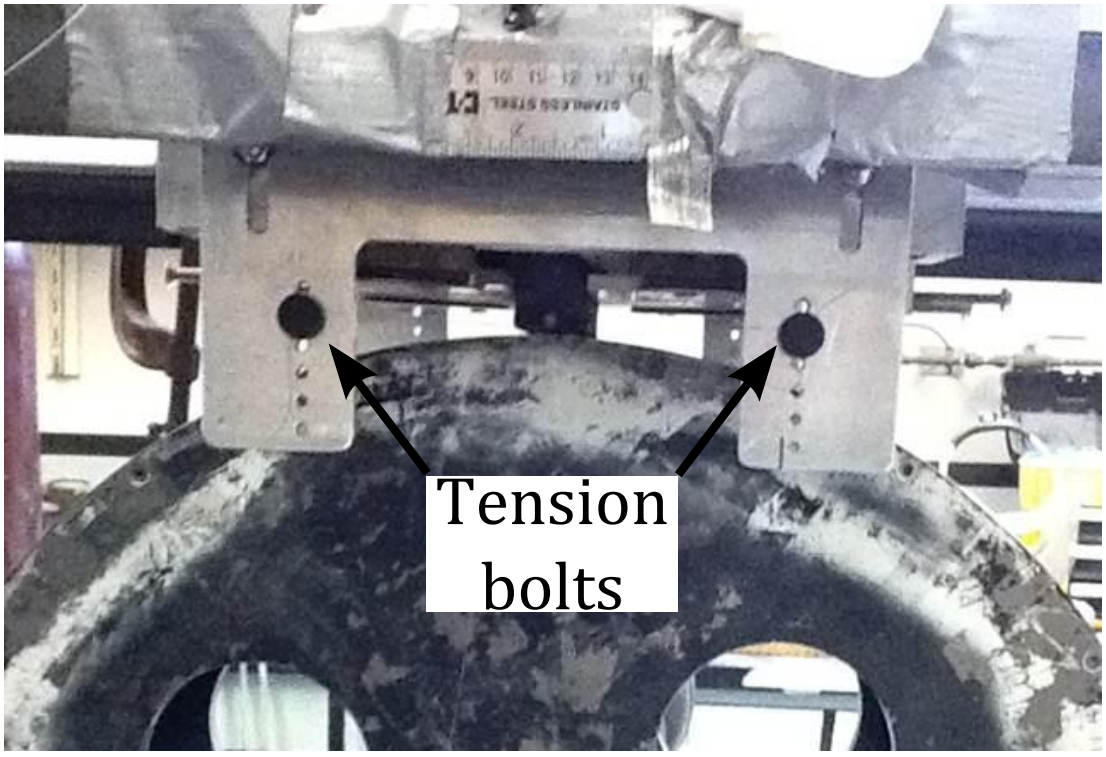

Figure 5.7: Photograph of a side-plate and bolts used to fasten wire.

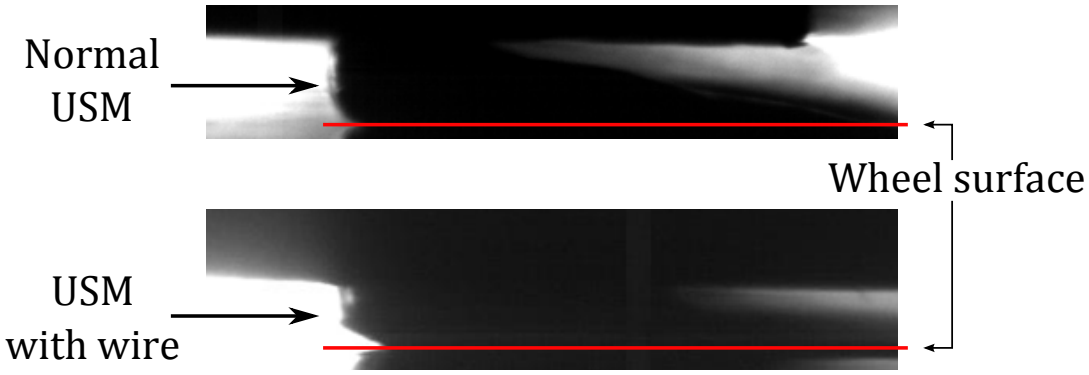

Figure 5.8: Puddle photograph for a non-wire and wire cast. Red lines have beend drawn to highlight the wheel surface. Wire contact with the USM is evident as the USM appears to have a kink.

(2013) were used, denoted BLC data. The BLC herringbone line is the 'best-fit' line presented by Cox and Steen for these data. Here, one of the wire cast points falls near that line, but the remaining data fall well above it. This suggests that the wire may influence the herringbone frequency. Recall that the herringbone fea-

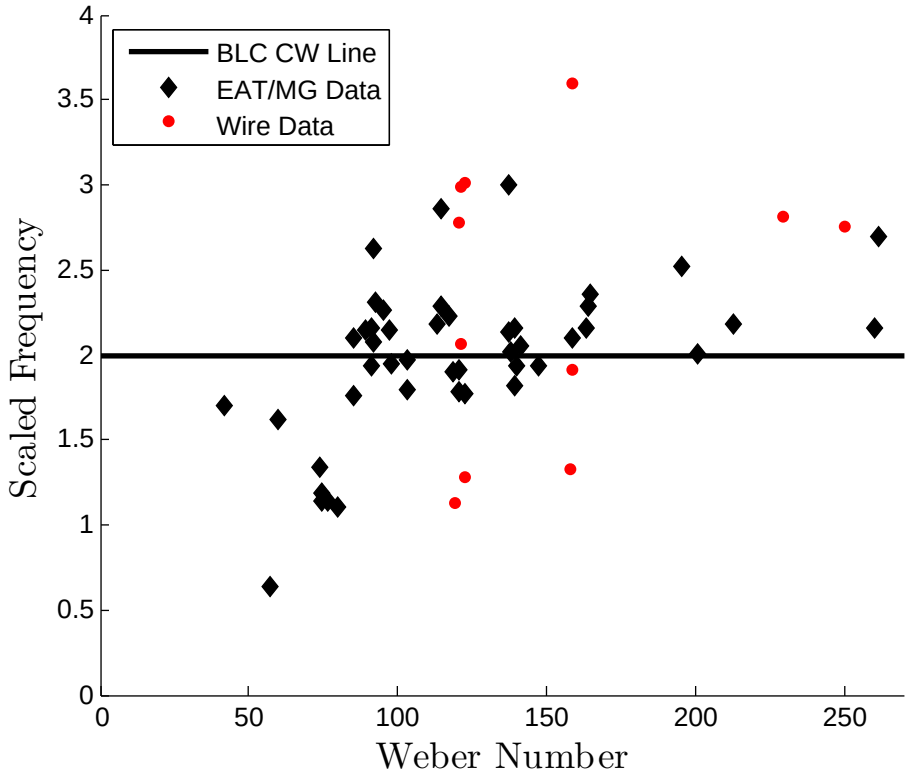

Figure 5.9: Scaled frequency versus Weber number for non-wire and wire casts with observed crosswave defect. Data are expected to fall around a line with zero-slope and intercept = 2 , shown as a solid line. No significant difference is created by the presence of the wire.

ture shares the capillary frequency dependence of crosswave, but has an additional dependence of the wheel speed. In particular, it was suggested in Cox and Steen (2013) [20] that a We dependence only appeared if the inlet flow traveled along the interface. The presence of a wire at the interface would disrupt this flow, thus altering the frequency.

The herringbone data were rescaled using an 'effective gap' G'. This was taken as the approximate distance from the wire to the wheel surface, estimated as half the set gap height and depicted in Figure 5.5. A plot of the rescaled wire data is given in Figure 5.11, where now the wire cast data fall on the BLC herringbone

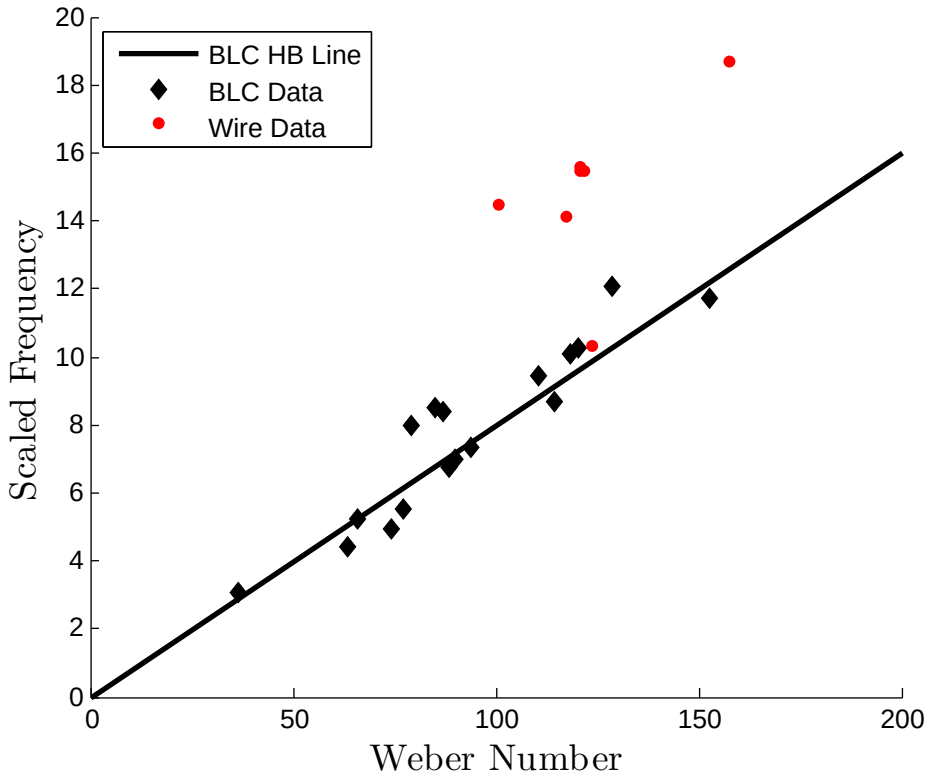

Figure 5.10: Scaled freuqency versus Weber number for non-wire and wire casts with observed herringbone defect. Data are expected to fall around a line with zero-intercept and slope = 0.08, shown as a solid line. Non-wire casts fall around this line, while wire casts fall above it.

line. There is no definitive explanation for this. However it is stated in Cox and Steen (2013) that a necessary condition for herringbone appearance is a pinned interface. In the absence of a wire, the distance between the pinning-point and the wheel is gap G. In wire casts, if the wire supplies a pinning constraint, then the distance between the pinning-point and the wheel is G'. Further study is required to fully understand this phenomenon.

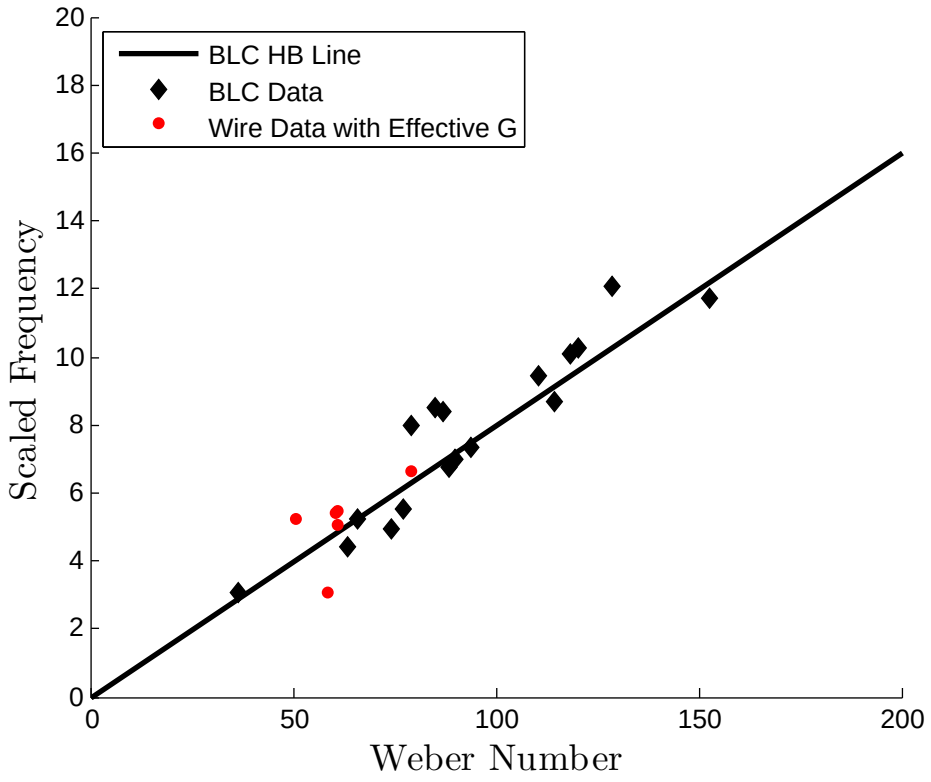

Figure 5.11: Scaled freuqency versus Weber number for non-wire and wire casts with observed herringbone defect. The wire casts have been given an 'effective gap' G', approximated as half the actual gap. Rescaled wire data using G' as gap fall on the herringbone line.

5.3 Boron Nitride casts

In the Summer 2013, controlled heat transfer interruptions were introduced to the wheel using Boron Nitride (BN). A BN suspsension was spray painted onto the wheel using an air brush. Stripes were painted in the axial (cross-stream) direction, depicted in Figure 5.12a. A photograph of an actual stripe on the wheel is shown in Figure 5.13. These stripes were produced by laying down a masking tape mask and then spraying the BN on. BN, an insulator relative to the wheel, reduces the solidification rate and yields thinner ribbon, depicted in Figure 5.12b. The purpose of this study was to determine the critical thickness of a BN stripe

to reduce the ribbon thickness sufficiently to cause a 'break' during the cast. BN stripe thickness, τ_{BN} is defined as the height of the stripe measured radially outward from the wheel surface. Stripe width is measured in the direction of wheel rotation. Thickness and width definitions are shown in Figure 5.12.

The thickness of the boron nitride depends on the flow-rate of suspension from the

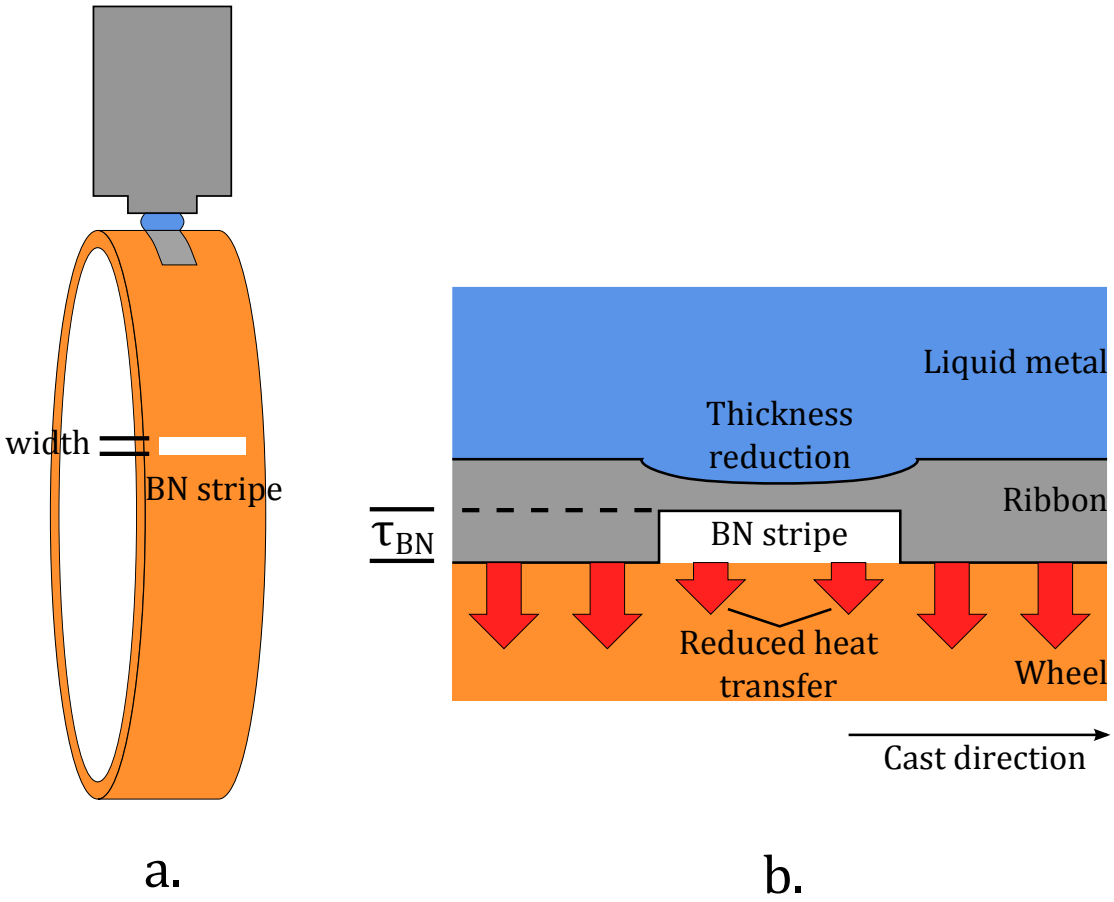

Figure 5.12: a. Schematic of a Boron Nitride (BN) stripe painted on the wheel. b. BN creates a heat-transfer interruption, reducing the amount of heat transfered to the wheel and causing a local ribbon thickness depression.

air brush, the speed of motion of the airbrush as it is passed by the wheel, and the distance between the air-brush nozzle and the wheel. To estimate the thickness, BN was sprayed onto transparency sheets and the difference in weight was mea-

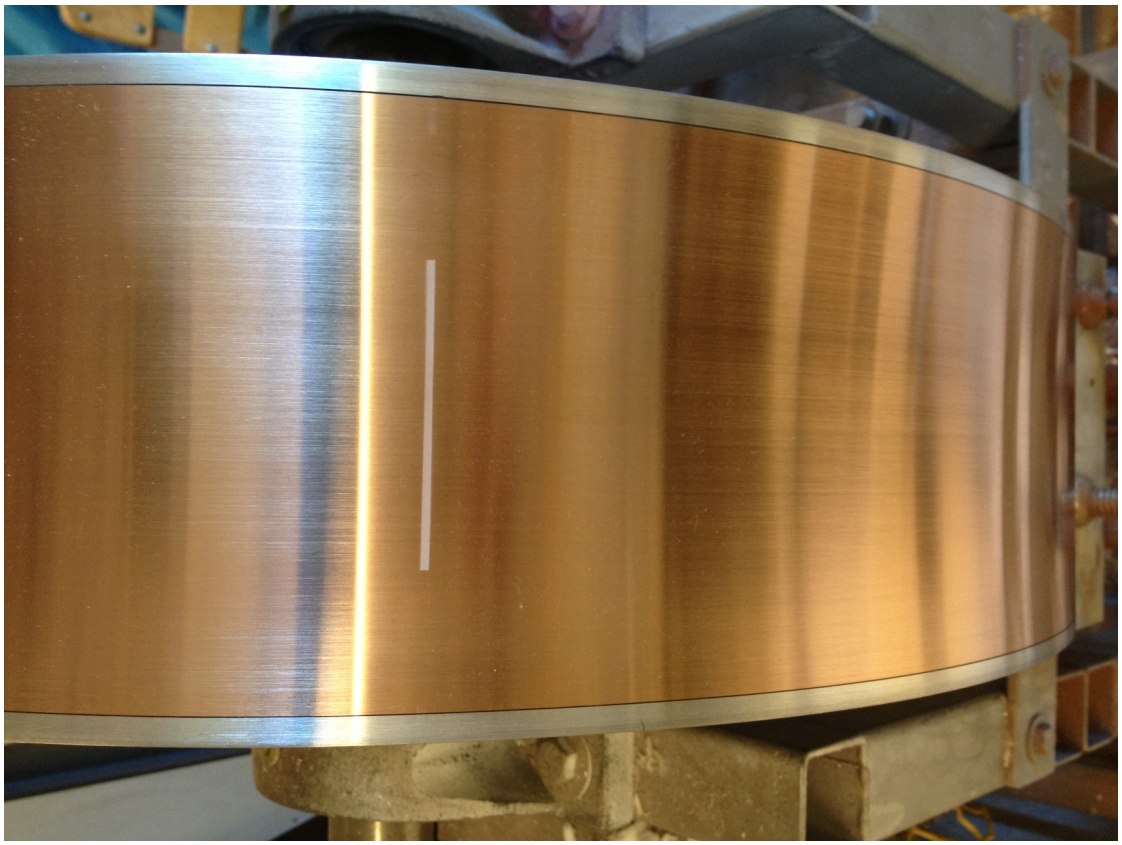

Figure 5.13: 1 mm wide BN stripe painted on the Cu-Be casting wheel as viewed from above the wheel.

sured. The thickness of the deposited BN, shown in Figure 5.14, was determined from the weight and dimensions of the rectangle sprayed onto the transparency. The data are given in Table 5.3, and show that the average thickness per pass of the air-brush is 0.62 μm. This is an estimate with considerable variability.

Five experiments were performed to try to identify the BN stripe thickness required to break the ribbon. It was found that, at a thickness between 2.7 and 4.7 μm BN stripe thickness, there was a transition from ribbon not breaking to ribbon breaking. The data are summarized in Table 5.3.

One of the difficulties in drawing conclusions from these data is that the ribbon

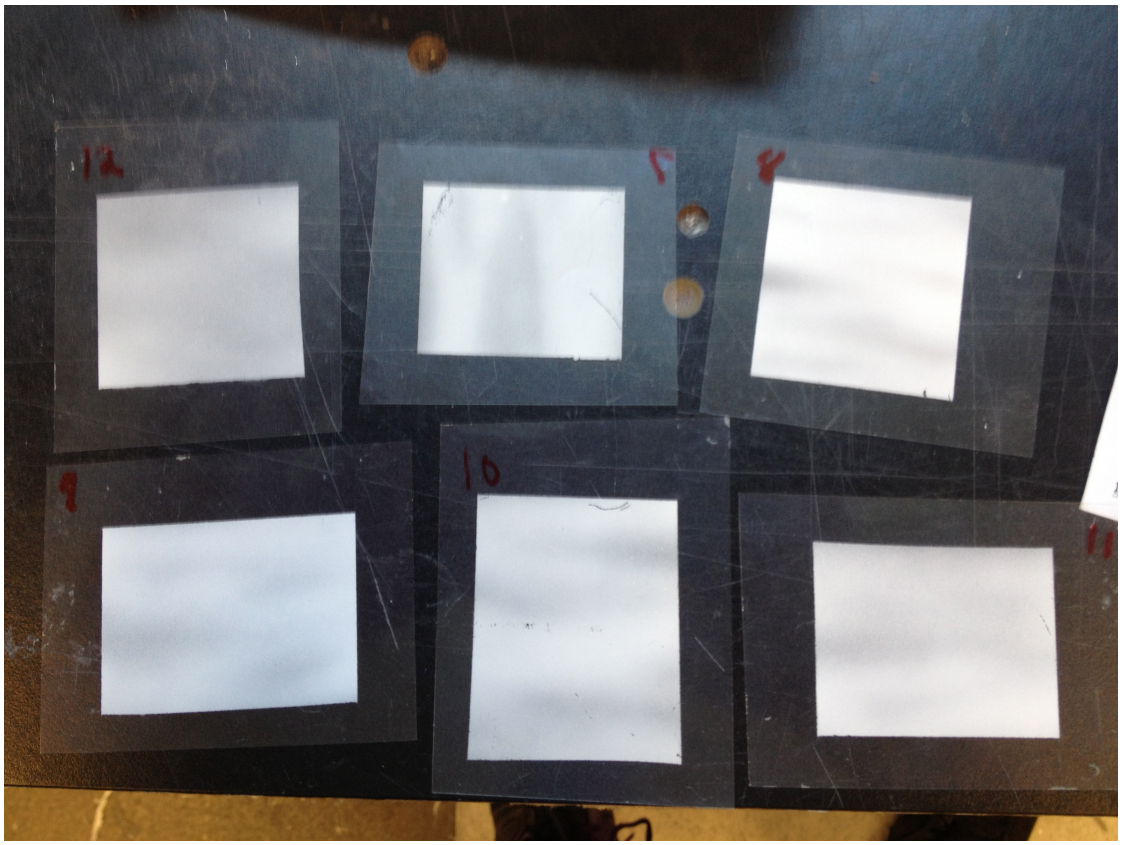

Figure 5.14: Painted BN squares on transparency sheets. Sheets were weighed before and after spraying to determine the approximate flow-rate of BN from the air gun.

	Average thickness (μm)			
Cast	Ribbon	BN Stripe	No. passes	Break
$CPSU13\_08$	120	6.67	10	yes
$CPSU13\_09$	160	5.33	8	yes
$CPSU13\_10$	110	4.67	7	yes
$CPSU13\_11$	100	2.67	4	no
$CPSU13\_12$	130	2.00	3	no

Table 5.2: Summary of BN cast data. The critical BN stripe thickness is estimated to be between 2.67 and 4.67 μm.

thickness is not consistent across casts. Local thickness variation of the ribbon could be a factor in whether or not the ribbon breaks. Another difficulty arises when the ribbon does break, and the disconnected pieces collect on the lab floor. Re-ordering these pieces is a challenge. It was successfully done by determining

the thickness of the segments and then piecing these thicknesses together. This works best when thickness decreased during a cast. When the cast thickness is relatively constant, it is not possible to do this with certainty. A plot of the successful re-construction of a BN segmented cast is given in Figure 5.15.

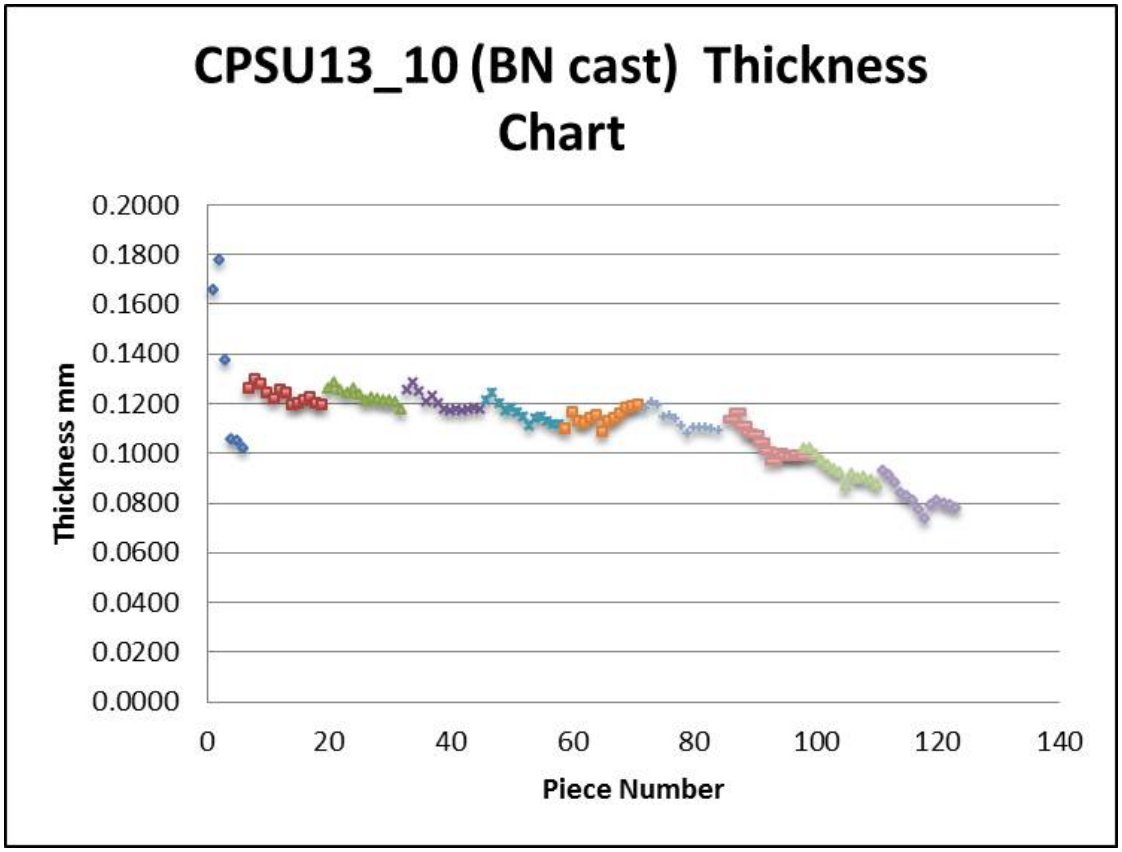

Figure 5.15: A cast where BN broke ribbon. Ribbon segments were re-ordered by stitching together thickness data across the BN-induced breaks.

CHAPTER 6

FUTURE WORK

Many aspects of planar-flow melt spinning would benefit from future studies. This chapter addresses these issues.

6.1 Ribbon adhesion

In chapter 2 the ribbon adhesion process was investigated using a ribbon cooling model coupled with a simple stress model. The model was used to quantitatively predict ribbon adhesion and the transition to catastrophic adhesion, which agreed with the qualitative observations reported by Liebermann [51]. In the model, the wheel surface temperature T_s, the ribbon adhesion energy γ, and the ribbon-wheel heat-transfer coefficient H were unknown quantities estimated by models or experiment.

T_s was estimated using a moving point-source model presented by Liebermann [51]. The limitations of this model are 1) the wheel is treated as a semi-infinite solid and 2) the point-source has infinitessimal size. The wheel heat-up model presented in Chapter 3 does not have either of these limitations. The model presented there might be incorporated into the sticking model to improve its accuracy. In particular, it might improve the prediction of catastrophic adhesion, which, at present is susceptible to even small errors in the estimate of wheel temperature which can accumulate over many revolutions.

Both γ and H depend on the nature of the ribbon-wheel contact. Changing wheel

materials, melt chemistry, or wheel surface preparation might affect this contact. H is easily found for new parameters via a one-parameter fit, discussed in Chapter 2. However, γ is more difficult to determine. In Chapter 2, γ was inferred from the detachment temperature T_d, which was measured by calorimetry. T_d might be more accurately determined using infrared measurements. In Summer 2013, an IR camera was lent to the Steen group by MetGlas. Preliminary experiments indicated that the IR camera could be positioned in front of the wheel to measure ribbon temperature as it detaches from the wheel. Precise positioning of the camera, reflectivity of the ribbon and wheel, and choosing an appropriate emissivity value present difficulties, which require further testing to address.

One final aspect of this project that could be explored involves determining the effect of T_d and γ on sticking. This could be investigated by altering the wheel and melt chemistry, or by adjusting the surface preperation via different sanding procedures or machining of the wheel. A new copper based wheel will be installed in Fall 2013. Additionally, an iron based alloy provided by MetGlas was successfully cast in the Spring of 2012. The sticking behavior of these materials could be examined using the framework presented in Chapter 2.

6.2 Defect Formation

As discussed in Chapter 4, two periodic defects related to capillary vibrations are present in the PFMS process. A meniscus vibration model presented in Chapter 4 indicated that the lower-frequency crosswave defect is similar to the vibrations of a cylindrical interface with constrained contact angle in a rectangular channel. A

stick-slip model brought in the wheel-speed dependence for the higher-frequency Herringbone defect.

A number of assumptions were made in the modelling: flow was considered irrotational, viscosity and gravity were neglected, the flow was considered 2-dimensional, solidification at the interface was modeled as constant flow, and the surrounding gas was considered passive. Some of these assumptions could be relaxed using the approach in Chapter 4 while others require computational methods that can readily include neglected effects.

The cross-stream direction was ignored in Chapter 4. For a flat interface, this direction was considered by Myshkis [58] and found to give stable vibrations. Cylinders however, can be subject to the Plateau-Rayleigh instability. It should be possible to include this 3-dimensionality into the Chapter 4 approach. Additionally, the dynamics of the surrounding gas could be considered and coupled to the liquid dynamics at the free interface, rather than assuming a constant gas pressure. This might provide some guidance for lab operating conditions. The surrounding gas properties will likely influence the USM vibrations, providing a way to control or suppress the vibrational frequency [80].

In Chapter 4, cylindrical interfaces are centered about the mid-plane of the rectangular channel (mirror symmetric). In this way, the base-state contact angle was the same at the top and bottom walls. The cylindrical base-state could be 'shifted' up or down to give different contact angles at the top and bottom walls. This might more closely agree with the observed USM, where a greater contact angle is observed at the wheel surface.

Two approaches were used to account for solidification in the puddle. In the first, an assumed base-flow was imposed, treating the solidification process simply as flow out of the bottom of the channel. In the second, the puddle dynamics were ignored and instead the contact line motion was examined assuming a stick-slip behavior, assuming that upon solidification, the lower contact line 'sticks' to the wheel and the USM is deformed. In actuality, stick-slip at the contact line likely affects the flow in the puddle. Additionally, flow into the solidification region should not be treated as constant; it is likely greatest at or near the USM when the ribbon is the thinnest and then decreases as the ribbon gets thicker.

When base-flow was included, it was assumed constant and irrotational. As pointed out in Cox and Steen (2013) [20], and by others [65], [3], there is evidence that vortices exist throughout the puddle. Using a volume of fluids approach, Bussmann (2002) predicted regions of recirculation near the USM [10]. It is expected that this secondary flow might influence the vibrational frequency of the USM.

Incorporating solidification and vorticity may not be possible with the methods outlined in Chapter 4. Instead, a computational approach would likely be most amenable to this problem. Bussman's (2002) volume of fluids approach was applied for problems without phase-change, such as in the formation of a metallic glass. This code could be modified to incorporate a phase change [10]. In either case, it may be possible to perturb the USM in this approach and examine the response. Viscous and gravitational effects, though small, can be incorporated into this method as well.

CHAPTER 7

SPRAY ATOMIZATION OF ONE AND TWO PHASE LIQUID SHEETS.*

7.1 Background

In the application of agricultural chemicals and pesticides, delivery to a target location is typically done by spraying through a nozzle. Agricultural nozzles vary in shape and size, but most discharge a continuous jet or sheet which disintegrates into droplets, called atomization. The size of the droplets produced affects how effectively they are delivered to the target. Small droplets may be carried from their target by air currents (called drift), while larger droplets may be unevently distributed on a target.

In this study, atomization of liquid sheets is examined. A liquid sheet is discharged through a nozzle and subsequently, through some mechanism, breaks apart into droplets, depicted in Figure 7.1. The study of liquid sheet stability dates back to Savart (1833), who examined impinging jets of liquid and the subsequent sheet that formed [67]. Nozzles which produce fan-like sheets were examined by Dorman (1952) who identified several important features of sheet breakup. At very low operating pressures, sheets were observed to form an oval shape and form large droplets upon breakup. At slightly higher pressure, the oval shape is mostly retained, but fluid fingers are observed at the sheet edges that break into large droplets. At higher pressures, the fan shape is fully developed. Smaller droplets

*This work was done at Dow AgroSciences during the Summer of 2012 under the supervision of Steve Cryer and Lipi Acharya. Accepted for publication in Atomization and sprays as 'Mechanisms, Experiment and Theory of Liquid Sheet Breakup and Drop Size from Agricultural Nozzles', coauthors SA Cryer and L Acharya.

are produced at the leading front of the fan, while larger droplets are produced at the edge. At these higher pressures, side photographs of the sheet reveal flapping type motions of the sheet before breakup [29].

Dombrowski and Fraser (1954) performed a thorough photographic investigation

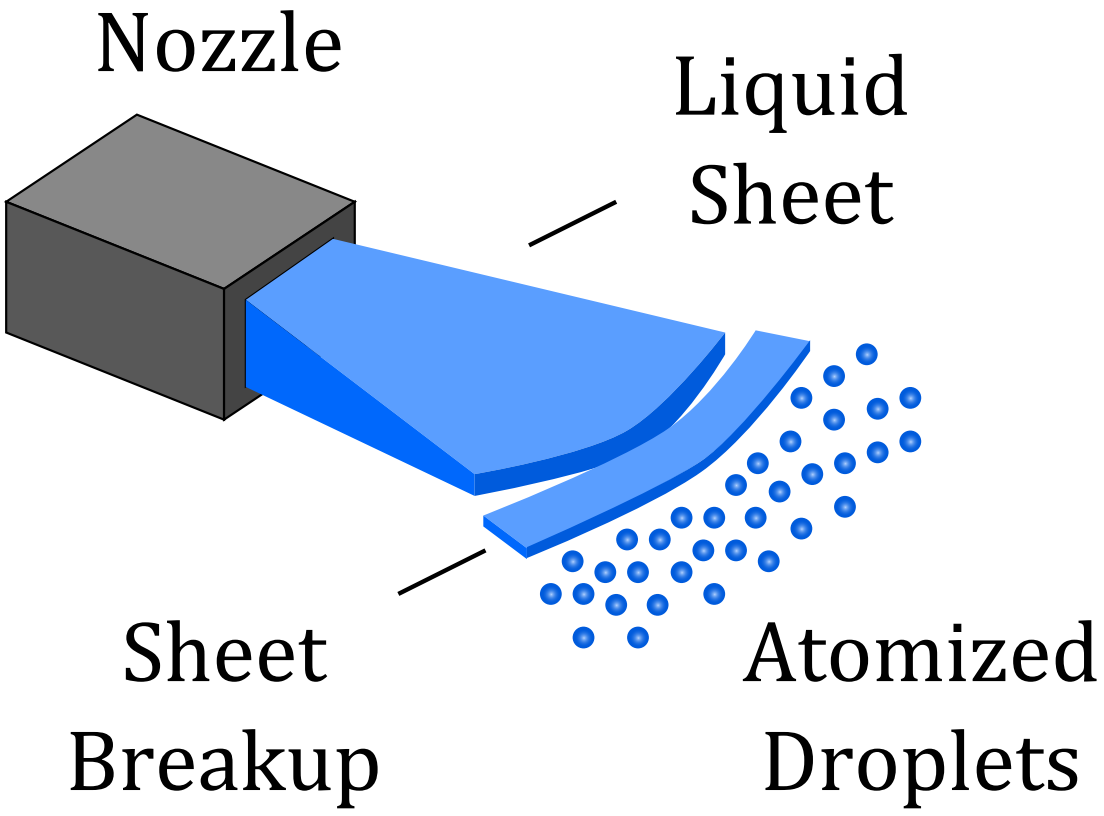

Figure 7.1: Schematic of a liquid sheet discharged through a nozzle. The sheet is subject to instabilities, which cause it to break into droplets.

of liquid sheet breakup, identifying several important features of sheet breakup. They observed rim and wave type breakup mechanisms described by Dorman (1952) [29], but also identified a third mechanism: hole formation and growth. They found that the presence of non-wettable oil or sulfur particles caused hole formation in water sheets, but solid particles such as glass, zircon, brick and copper did not, regardless of particle size. They found that larger suspended particles

which formed holes did so closer to the nozzle [28].

Fraser et al. (1962) present a model for the breakup of a flat, inviscid sheet when flapping motion is present. In this model, a sinusoidal disturbance to the sheet creates waves which grow in time. One the amplitude of the waves has become sufficiently large, a ribbon of liquid detaches from the sheet, retracts instantaneously into a cylindrical ligament, and then breaks apart due to the well known Plateau-Rayleigh instability, depicted in Figure 7.2. This model was shown to give good agreement with data by Fraser et al. (1962) [30], Dombrowski and Hopper (1963) [26] and recently by Negeed, et al. (2011) [60]. Despite the agreement with data, the model was subject to criticism in several later publications. In particular, the model for wave growth relied on *temporal* stability theory. Lin and Wang (2008) point out that in experiment, growing waves convect with the sheet, which cannot be captured by temporal stability analysis [53]. Villermaux and Clanet (2002) agree that wave growth leads to sheet breakup, but disagree about the mechanism through which droplets detach [81].

Most authors on the subject of sheet stability reference the work of Lord Rayleigh (1879) who identified two linearly independent mode shapes (Figure 7.3) for liquid sheets: a sinuous mode which has interfaces moving anti-symmetrically with respect to the mid-plane and constant sheet thickness, and a varicose or dilational mode which has interfaces moving symmetrically, creating locally thin and thick regions of fluid [64].

The work of Fraser, et al. (1962) [30] relies on the temporal stability of a liquid sheet presented by Squire (1953). Squire considered an inviscid, incompressible

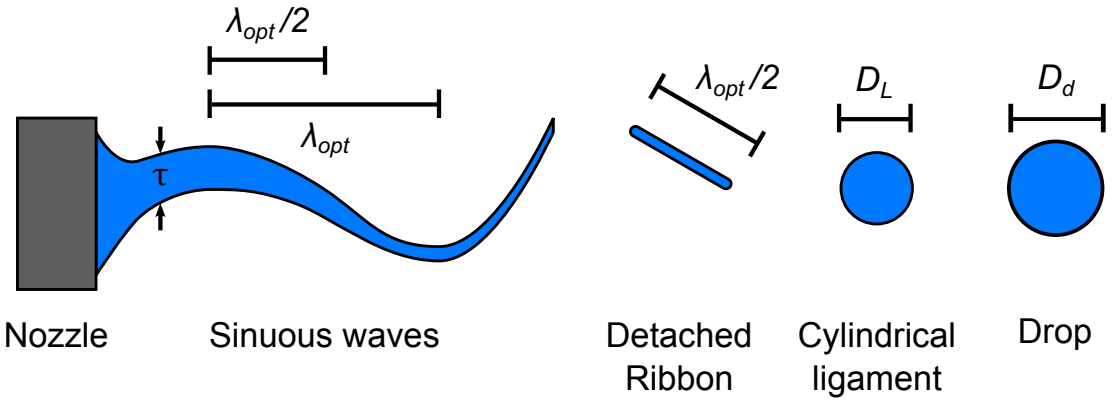

Figure 7.2: Sheet breakup mechanism proposed by Fraser, et al. Waves grow until a critical value, when a ligament detaches and contracts into a cylinder. The cylinder is subject to the well known Plateau-Rayleigh instability and breaks into droplets.

sheet, translating through air. Surface tension effects were assumed to dominate gravitational effects. Assuming potential flow, Squire considered the equations of motion in the sheet and gas layers above and below the sheet, subject to the usual kinematic/dynamic boundary conditions. Following classical, *temporal* stability procedure, sinusoidal disturbances were introduced to the sheet of the form $\exp[i\alpha x - i\omega t]$, where α is a *real* wavenumber, x is the direction of translation of the sheet, ω is the *complex* wave growth rate, and t is time. From the governing equations, a dispersion relation was derived to identify conditions under which disturbances were expected to grow. Squire characterized these conditions in terms of two dimensionless parameters: Weber number $We = \rho U^2 \tau / 2\sigma$ and gas/liquid density ratio $Q = \rho_g / \rho$, where ρ and ρ_g are the liquid and gas densities, U is the sheet translation speed, $\tau/2$ is the half-sheet thickness, and σ is the surface tension (note that Squire defined We as the inverse of how it is defined here). The results from the analysis were [68] [68]:

1. Sinuous waves are more unstable than dilational
2. Disturbances do not grow in time for $Q = 0$ (i.e. zero gas density)

3. For finite Q, sheets are unstable for $We > 1$

4. Surface tension stabilizes, shear at interface destabilizes

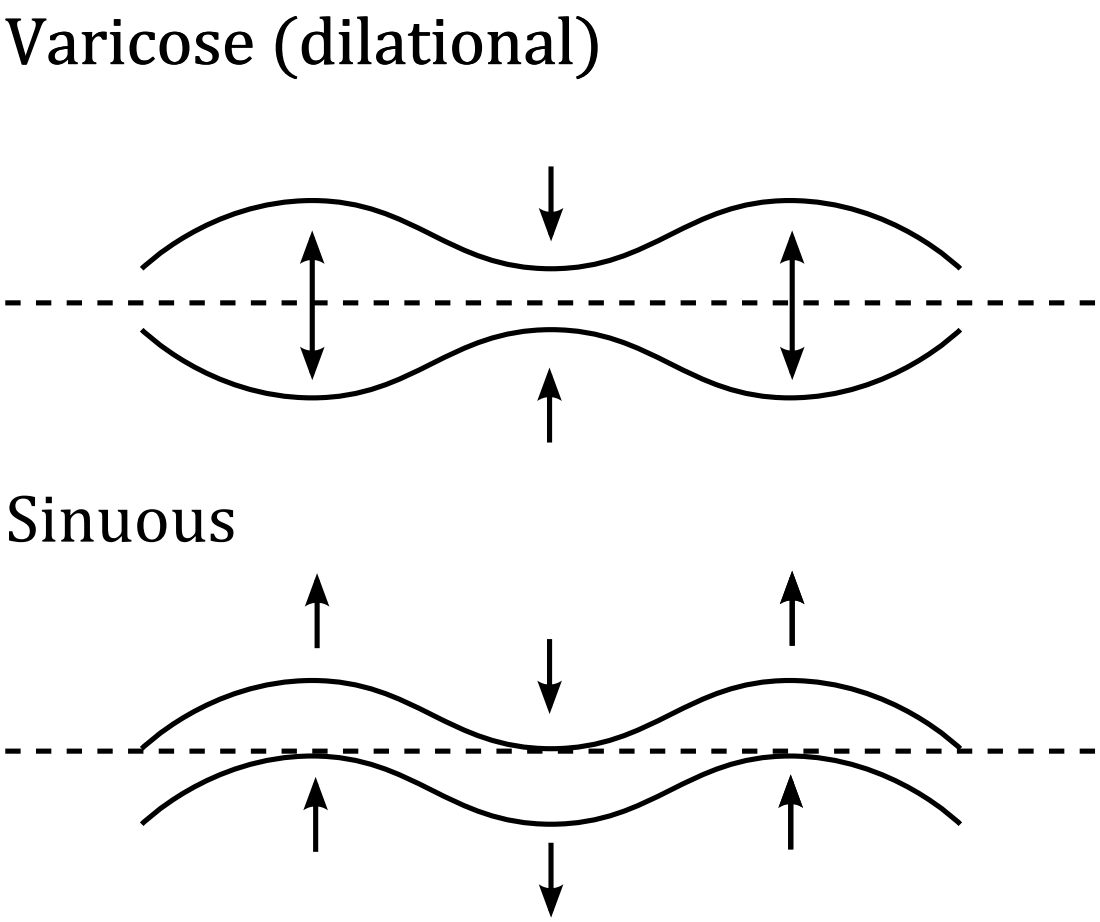

Figure 7.3: Schematic of two mode mode shapes of liquid sheet. Varicose or dilational modes have interfaces moving symmetrically with respect to the mid-plane, creating locally thick and thin regions on the sheet. Sinuous modes have interfaces moving anti-symmetrically w.r.t the mid-plane, having constant sheet thickness.

Squire's results were reproduced by Hagerty and Shea (1955) [34]. However, curtain coating experiments reported by Brown (1961) indicated that sheet instability was present for $We < 1$, contradicting theoretical results [9].

A more general stability theory, often called spatio-temporal stability, allows disturbances to grow in time and space. Sturrok (1958) distinguished convective

instabilities which grow spatially from non-convective instabilities for a general dynamical system[71]. These ideas were expanded by Briggs (1964), who derived criteria for the presence of absolute versus convective instabilities by converting the original differential equations for a problem in integral equations and looking at the long-time asymptotic behavior [8]. Gaster (1962) derived a relationship between the instability found from temporal stability analysis and a convective instabilty for special systems [31].

Using spatio-temporal stability, Lin, et al. (1990) found that for $We < 1$ and $Q = 0$, sinuous disturbances spread in space but remained neutrally stable [52]. De Luca and Costa (1997) found unstable sinuous disturbances for $We < 1$ [25], in agreement with Brown's experimental results [9]. However, Luchini's (2004) analysis indicated that sinuous disturbances were stable for $We < 1$ [55].

These discrepancies were sorted by Barlow, et al. (2010, 2011), who found that the nature of the initial disturbance changed the asymptotic behavior of the sheet. In particular, if an impulse disturbance to the sheets position is introduced for $We < 1$, the disturbance decays algebraically, agreeing with Luchini (2004). However, if the sheets position *and* velocity are impulsively disturbed for $We < 1$, the disturbance grows in all space, agreeing with the findings of De Luca and Costa (1997). Barlow, et al. (2011) also point out that the absence of a surrounding fluid creates a stable configuration. However, the author's found that impusively disturbing the position and velocity yields a convective instability of varicose mode shapes [1][2].

Barlow, et al. (2010, 2011) point out (as well as other authors) that for $We > 1$,

if one were to move with the sheet, sinuous waves would appear to grow like $\exp[\omega t]/t^{1/2}$, rather than being purely exponential. The difference lies in the nature of the initial disturbance: temporal stability traditionally considers the most unstable sinusoidal disturbance, while spatio-temporal theory typically considers impusles [1]. Fraser, et al. (1962) do not include the factor of $t^{1/2}$ in their analysis, yet their model of sheet breakup has shown good agreement with data. One possible explanation for this is that, for $We >> 1$ (typically the case for agricultural nozzles), the growth rate ω gets larger, eventually causing the exponent to dominate the growth of waves, even for small time. In any case, Barlow, et al. (2011) conclude by stating that the initial disturbance and subsequent sheet stability depends greatly on the experimental setup [1][2].

Villermaux and Clanet (2002) found acceleration-based breakup mechanisms of liquid sheets. Body forces acting on a fluid interface can lead to instability, and in the case of a sheet, manifests as detaching droplets. These authors advocate this mechanism of sheet atomization when flapping is present, contradicting the mechanism put forth by Fraser, et al. (1962). Which mechanism is correct has not been conclusively established in the literature, but the work from this study supports the Fraser mechanism. However, Villermaux and Clanet (2002) derive a threshold for when flapping is expected to dominate which seems to agree with the experimental observations discussed later [81][17].

Several authors have examined non-linear stability of liquid sheets. Clark and Dombrowski (1972) considered second order corrections to the linearized disturbance equations (i.e. the first set of terms considered negligible in standard linear stability analysis) [18], and later Jazayeri and Li (2000) looked at third order cor-

rections [42]. It was found that varicose modes contributed to linear stability at higher orders. Hadji and Schreiber (2007) numerically examined 2-dimensional sheet stability for various initial disturbances. Of particular interest to this study was the initial configuration of an array of peaks, which transitioned to ripple-like disturbances and higher energy states, indicating instability [33].

The presence of an oil phase in a liquid sheet was experimentally observed by Cloeter, et al. (2010) to cause breakup in a liquid sheet sooner than if the single phase liquid was sprayed. They also observed a reduction in the number of smaller droplets with only a slight increase in the overall atomization droplet size distribution. These authors speculate that deformation of oil particles while ejecting from the nozzle creates disturbances in the sheet which induce breakup [19]. Dombrowski and Fraser (1954) also found that the presence of deformable oil particles created holes in the sheet [28]. Fraser, et al. (1962) present a model for hole growth on a thinning sheet which agreed with photographs, however they don't predict droplet size from this breakup mechanism [30].

7.2 Models of sheet breakup

In this section, several existing models of sheet atomization and subsequent droplet size are presented. The three mechanisms of sheet breakup considered are: 1) flapping motion (wave growth), 2) rim breakup from acceleration of the sheet, 3) hole growth breakup. Models of hole growth on a sheet have been considered by several authors, but a novel model of sheet breakup due to hole growth is presented.

7.2.1 Wave growth

The model of wave growth and subsequent sheet breakup presented by Fraser, et al. (1962) has been used with good agreement with data by several authors, discussed above [30]. A sketch of the derivation and model is presented here. The model builds on Squire's temporal stability analysis of an inviscid, irrotational, incompressible sheet translating through air. Assuming sinuous mode shapes are more unstable for large We, the fastest growing unstable mode has wavelength λ_{opt} and growth rate ω_{max}

$$\lambda_{opt} = \frac{4\pi\sigma}{\rho_g U^2} \tag{7.1}$$

$$\omega_{max} = Q\left(\frac{\rho U \tau_b}{\sigma}\right)^{1/2} \tag{7.2}$$

where σ is the surface tension, ρ_g and ρ are the gas and sheet densities, U is the sheet translation speed, $Q = \rho_g/\rho$, τ_b is the sheet thickness at breakup. Under the assumption of classical stability, wave amplitude of the most unstable mode grows as

$$h = h_0 \exp[\omega_{max} t] \tag{7.3}$$

where h and h_0 are the amplitude of the wave at time t and t_0. Using an experimentally determined value of $\ln(h/h_0) = E$ and the relationship between sheet thickness τ and distance from the nozzle ξ

$$k = \xi\tau \tag{7.4}$$

Fraser, et al. (1962) derive an expression for the sheet thickness at breakup, τ_b

$$\tau_b = \left[\frac{1}{2E^2}\right]^{1/3}\left[\frac{k^2\rho_g^2 U^2}{\rho\sigma}\right]^{1/3} \tag{7.5}$$

corresponding to a breakup length ξ_b of

$$\xi_b = k \left[\frac{1}{2E^2}\right]^{-1/3} \left[\frac{k^2\rho_g^2 U^2}{\rho\sigma}\right]^{-1/3}. \tag{7.6}$$

Next, it is assumed that a ribbon detaches with thickness τ_b and half-wavelength, which then contracts into a cylindrical ligament with diameter D_c. The long cylinder then breaks into spheres with diameter D_s according to the classic Rayleigh-Plateau prediction, $D_s = 1.89 D_c$. Finally, the prediction for final droplet size is

$$D_d = 0.9614 \left[\frac{k^2\sigma^2}{\rho_g \rho U^4}\right]^{1/6} \tag{7.7}$$

or, in terms of dimensionless numbers

$$D_d = 0.9614 \left[\frac{1}{Q}\right]^{1/6} [k\tau_0]^{1/3} \left[\frac{1}{We}\right]^{1/3}. \tag{7.8}$$

It may seem counter-intuitive that the droplet size is inversely proportional to the Weber number. As pointed out by Squire (1953), surface tension *stabilizes* the sheet, yet here it appears to increase droplet size. One might think that, for larger surface tension the sheet would remain intact longer, thinning as it moved farther from the nozzle. When breakup finally occurs, it should produce smaller drops, according to this reasoning. However, the full mechanism must be considered before making this conclusion. A ribbon detaches from the sheet with half wavelength, where wavelength is directly proportional to surface tension, as given by Eq. (1.10). The thickness at breakup, given by Eq. (1.9), shows a surface tension power dependence of -1/3. Thus, even though the sheet would tend to be thinner farther from the nozzle, consistent with intuition, the wavelength will be much longer, and the net result is larger drops.

7.2.2 Viscous flapping sheet

Dombrowski and Johns (1963) derived a model for the thinning liquid sheet with viscosity included [27]. The derivation is lengthy and will not be reproduced here, however a brief description of their approach is as follows. A liquid sheet with variable thickness sits in a translating gas with speed U. Rather than use hydrodynamic stability results, they construct a force balance:

$$Pressure Force + Surface\, Tension\, Force + Inertial\, Force + Viscous\, Force = 0.$$

Then, imposing a sinusoidal disturbance to the system and assuming the sheet thickness varies according to $k = \xi\tau$ they arrive at the following expression for the ligament diameter breaking away from the sheet D_L and the resulting droplet size D_d

$$D_L = C\left(\frac{k^2\sigma}{\rho\rho_g U^4}\right)\left[1 + 2.6\mu^3\sqrt{\frac{k\rho^4U^7}{72\rho^2\sigma^5}}\right] \tag{7.9}$$

$$D_d = D_L\left[1 + \frac{3\mu}{\rho\sigma D_L}\right]^{1/6} \tag{7.10}$$

7.2.3 Single hole growth on a sheet

Culick (1960) [23] and Fraser, et al. (1962) [30] investigated the growth rate of a perforation forming on a liquid shieet, and an original extension of their work is derived in this section to predict droplet size for a two-phase spray system.

Fraser, et al. (1962) begin with a force balance about a circular perforation of radius r forming in a liquid sheet of thickness τ. It is assumed that the only force acting on the hole is due to surface tension. This unbalanced force results in ex-

pansion. Assuming that all the liquid which was originally contained in the hole accumulates in a rim at the perimeter, the mass contained in the rim m_r is

$$m_r = \rho\pi r^2\tau \tag{7.11}$$

Inherent in this assumption is that the volume of liquid that occupied the hole is cylindrical with constant height τ and radius r. In reality, τ (sheet thickness) is not constant, since the sheet thins as it moves away from the nozzle. τ is assumed to be an average thickness at some distance ξ from the nozzle.

The force of surface tension for a hole in a sheet of fluid is $4\pi r\sigma$, which is the circumference of a circle times the surface tension (multiplied by 2 to account for two interfaces). The momentum of the fluid in the rim around the circle is mass times velocity, or $\rho\pi r^2\tau v$, where v is the rate of growth of the hole. The force balance is m

$$\frac{d}{dt}\left[\rho\pi r^2\tau v\right] = 4\pi r\sigma \tag{7.12}$$

Using the relations

$$\frac{dr}{dt} \equiv v, \qquad \frac{dv}{dt} \equiv v\frac{dv}{dr}, \qquad G \equiv \frac{4\sigma}{\rho\tau}$$

the force balance is rewritten

$$2v^2 + vr\frac{dv}{dr} = G \tag{7.13}$$

where it has been assumed that $d\tau/dt \sim 0$. Using the initial condition that $v = v_0$ at $r = r_0$, where r_0 equals half the sheet thickness, the solution is

$$2v^2 - G = (2v_0 - G)\left(\frac{r_0}{r}\right)^4. \tag{7.14}$$

Holes are expected to grow several millimeters or more in size, and thus the ratio $(r_0/r)^4 << 1$, so

$$v = \sqrt{\frac{2\sigma\xi}{\rho k}} \tag{7.15}$$

Assuming a hole forms at a distance ξ_0 from the nozzle and making use of

$$v \equiv \frac{dr}{dt} = \frac{dr}{d\xi}\frac{d\xi}{dt} = U\frac{dr}{d\xi}$$

the hole radius can be solved for as a function of position from the nozzle

$$r = A\left[\xi^{3/2} - \xi_0^{3/2}\right] \tag{7.16}$$

$$A = \left(\frac{8}{9}\right)^{1/2}\left(\frac{1}{We}\right)^{1/2}\left(\frac{\tau_0}{k}\right)^{1/2} \tag{7.17}$$

This equation was given by Fraser, et al. (1962) and compared favorably with their photographic data of hole growth [30].

7.2.4 Hole breakup of a sheet

A new model is proposed to describe the breakup of emulsion sheets due to colliding holes. In single-phase sprays, a single liquid is forced through a nozzle. In emulsion-sprays, a two-phase emulsion of oil droplets in water is sprayed through a nozzle. For this approach, n_p oil particles are considered evenly spaced with spacing z. The control volume will be considered with thickness τ, width a, and the arc curved length $s = n_p z$. The leading edge of the sheet is considered to be a circular arc.

It is hypothesized that an oil particle acts as a nucleation site for a hole. A hole forms and begins to grow ($t = t0$). As it grows, liquid accumulates in a ring aruond the hole, and it is assumed that all the liquid that occupied that hole now resides in a torroidal ring at the circumference of the hole.

The proposed mechanism for sheet breakup due to hole formation is depicted

schematically in Figure 7.4. Rims surrounding two growing holes begin to approach eachother as their radii grow ($t_0 < t < t1$). Upon contact, the rims coalesce into a single cylindrical ligament ($t_1 < t < t_2$). Finally, long fluid cylinders break down according to the Plateau-Rayleigh instability into droplets ($t > t_2$).

For modeling purposes, suppose a hole within the liquid sheet forms at the

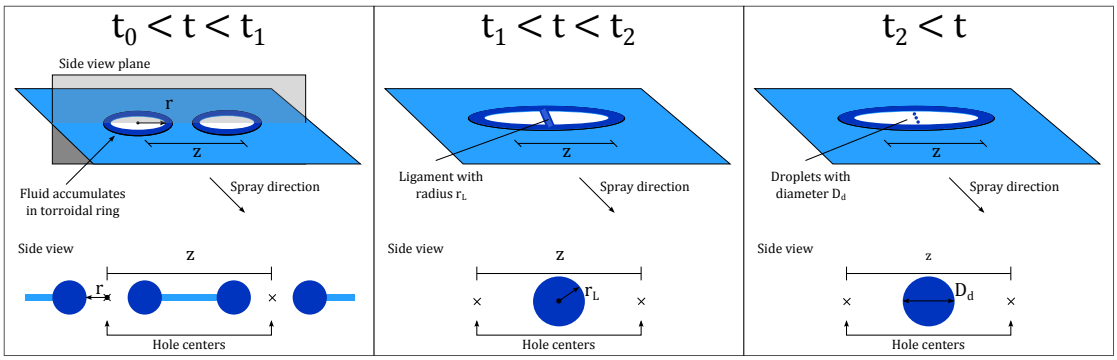

Figure 7.4: Proposed mechanism for hole breakup. Holes form at nucleation sites at $t = t_0$ with spacing z. They grow while $t_0 < t < t_1$. For $t_1 < t < t_2$, the holes collide and form a cylindrical ligament. Then, at $t = t_2$, the Plateau-Rayleigh instability causes the cylinder to break up into droplets.

location of each oil particle, uniformly spaced by a distance z. Assuming holes grow according to, the expanding holes will eventually colllide with each other once each hole has expanded to a radius $z/2$. This assumption ignores the radial expansion liquid sheet as it propogates away from the nozzle. Thus, the distance from the origin when holes collide is a function of the distance between the initial uniform hole placement.

$$z = 2A[\xi_b^{2/3} - \xi_0^{3/2}] \tag{7.18}$$

where x_0 and ξ_b are the distance from the origin where the hole first forms and the distance when the holes have collided, respectively. Solving for ξ_b

$$\xi_b = \left[\frac{z}{2A} + \xi_0^{3/2}\right]. \tag{7.19}$$

Assuming that all the liquid that occupied the hole now resides in a torroidal ring at the circumference of the hole, a mass balance demands that

$$\rho\pi r^2\tau_b = 2\rho\pi^2 r r_t^2 \tag{7.20}$$

or, using $\xi_b\tau_b = k$ and $r = z/2$

$$r_t = \left(\frac{zk}{4\pi\xi_b}\right)^{1/2} \tag{7.21}$$

$$= \left(\frac{zk}{4\pi\left[\frac{z}{2A} + \xi_0^{3/2}\right]^{2/3}}\right)^{1/2} \tag{7.22}$$

In an ideal case, two fluid tori with radius r_t and cross-sectional area $2\pi r_t^2$ would coalesce upon contact and form a cylindrical ligament with area $\pi r_L^2 = 2\pi r_t^2$. The ligament (liquid cylinder) formed by the coalescence of the rim of the liquid surrounding each hole would then decompose into droplets according to the Plateau-Rayleigh criterion, producing droplets with diameter $D_d = 3.78 r_L$ or

$$D_d = 5.34\left(\frac{zk}{4\pi\left[\frac{z}{2A} + \xi_0^{3/2}\right]^{2/3}}\right)^{1/2} \tag{7.23}$$

For fitting purposes, equation can be re-written as

$$D_d = (Ck^3A^2z + D)^{1/6} \tag{7.24}$$

where A, C, D are constants. For holes forming close to the nozzle, $\xi_0 \approx 0$, so the droplet size prediction is

$$D_d = C(z\tau_0 k^2)^{1/6}\left(\frac{1}{We}\right)^{1/6} \tag{7.25}$$

7.3 Experimental data analysis

7.3.1 Nozzle performance

A Teejet 8002 nozzle was used in the following data collection. The spray angle was found to vary as a function of applied pressure. Spray angle was measured manually from a series of DSLR images at various pressures. Applied pressure was related to velocity by conservation of mechanical energy, such that

$$v = 117.4\sqrt{\frac{\Delta P}{\rho}}$$

where the pressure is in $psig$, density in $kg/m3$, and velocity is in m/s. The spray parameter, k, depends on θ according to

$$k \equiv \frac{\tau_n W_n}{2\sin\theta/2}.$$

Parameters k and θ are both required for estimates of the resulting droplet size following sheet breakup and are estimated by fitting the power law function to experimental observations.

$$\theta = 19.7U^{0.44}, \qquad k = (2\times10^{-6})U^{-0.39}$$

and thus the spray parameter k scales as $We^{-0.2}$.

7.3.2 Qualitative spray features from images

Hundreds of DSLR images were taken of sprays using Teejet 8002, Teejet 110015, and Teejet air-induction nozzles. Pure water was sprayed as well as various con-

centrations of Interlock oil-in-water emulsions. Three modes of sheet disintegration were identified: wave, rim, and hole breakup, respectively, per Fraser and Eisenklam (1962). Despite discrepancies in theory about the exact mechanism of breakup when sheet flapping is occurring, the images captured in this work support in the mechanism set forth by Fraser et al. (1962), discussed previously.

Detached ligaments were frequently seen in images from water spraying experiments, as shown in Figures 7.5. This type of behavior was typically observed in the pressure range of 20-40 psig. Figure 7.5 (a) illustrates a breakup pattern having completely detached ligaments from the front of the sheet. More typical were images like 7.5 (b), where a ribbon of fluid detached for part of the sheet. Note that in many moderate-to-high pressure images, fluid 'fingers' at the sides of the sheet were present, consistent with a rim breakup type mechanism. However, due to the number of detaching ligaments captured, images suggest that rim breakup is subdominant to Fraser-type breakup at these pressures. There was evidence of waves in the images, as can be seen in Figure 7.5 (b), however these were difficult to distinguish from photographs in the moderate-to-high pressure images.

Below 20 psig, detached fluid ligaments were not observed. Instead, the sheets appeared to disintegrate from the outside inward. Rim breakup fluid fingers were always observed at these lower pressures. Figures 7.6 show typical sheets sprayed in the 5-20 psig range where rim breakup was the predominate mechanism for atomization.

Introduction of a second, immiscible phase to the spray dramatically altered the

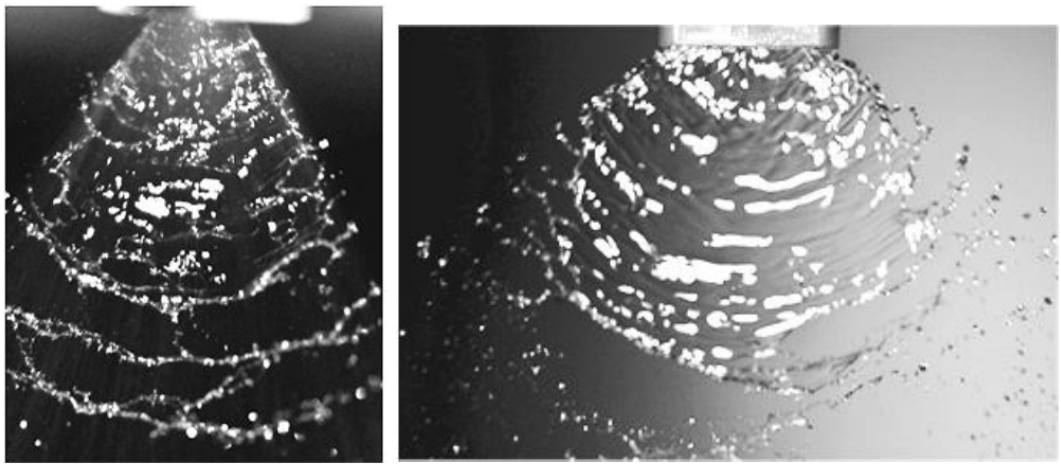

(a) (b)

Figure 7.5: Single phase, water spray showing Fraser-like breakup. Pure water sprayed at 40 *psig* through a Teejet a) 8002 and b) 110015 fan-type nozzle.

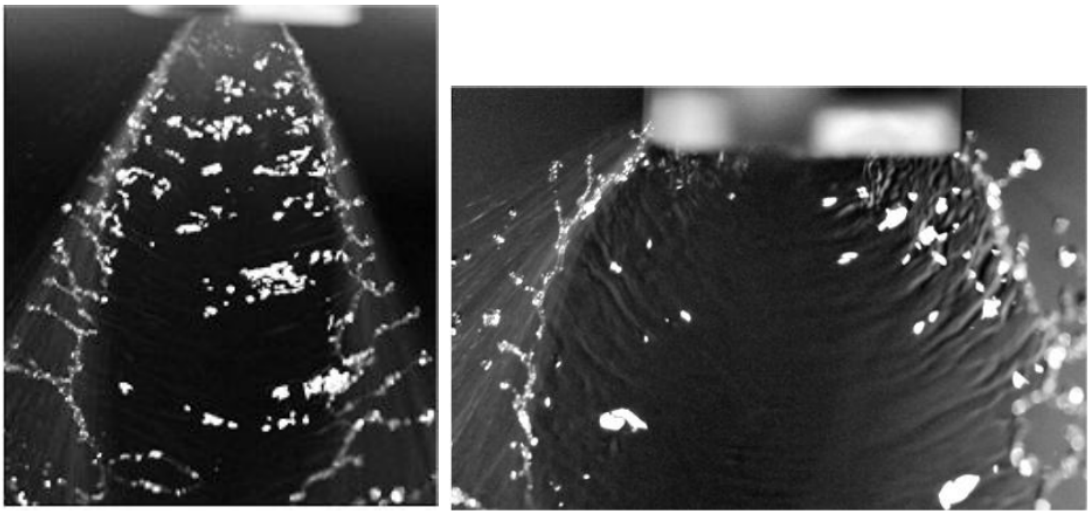

Figure 7.6: Single phase, water spray showing rim breakup. Pure water sprayed at 20 *psig* through a Teejet a) 8002 and b) 110015 fan-type nozzle.

behavior of the sheet. In particular, all images captured showed a liquid web at the sheet front, which then disintegrated into droplets, Figure 7.7. This occurred in all pressure ranges, indicating that a 3rd mechanism now dominated over the other two mechanisms (rim, flapping/ligament) observed in single phase spraying. Figure 7.7 (a) shows a liquid web from an Interlock-in-water experiment sprayed in

the 5-10 psig range, and Figure 7.7 (b) shows a similar web in the 20-40 psig range.

It is believed that the oil phase serves as a nucleus for the creation of a hole,

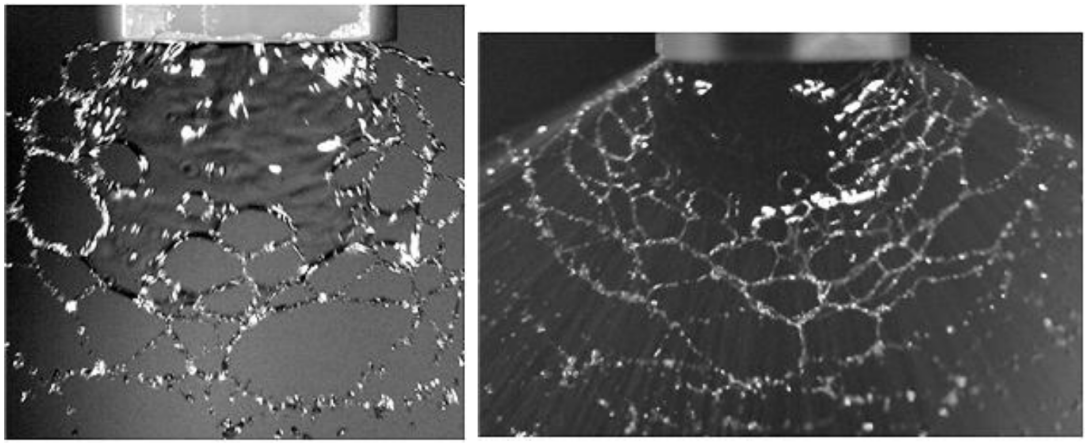

(a) (b)

Figure 7.7: Oil-in-water emulsion spray, displaying hole breakup mechanism. 0.5 – 5 % Interlock in water sprayed through a Teejet a) 8002 and b) 110015 fan-type nozzle.

which then expands due to a force imbalance. Upon collision with other holes, a liquid web is formed, which then breaks apart into droplets due to a Plateau-Rayleigh-type instability. Figure 7.8 shows each stage of this mechanism occurring. Again, a liquid web is apparent, as well as collided holes which have not yet fully formed into a web. Of particular interest are the ripples highlighted in Figure 7.8. These were almost always observed in close shots of emulsion sprays. It is not yet clear whether these ripples are the growth of a disturbance which becomes a hole, or if there is a dewetting phenomenon due to the immiscibility of the phases. An oil soluble red dye was added in one set of experiments in an attempt to highlight an oil drop in the center of these ripples without success in definitively quantifying this proposed mechanism.

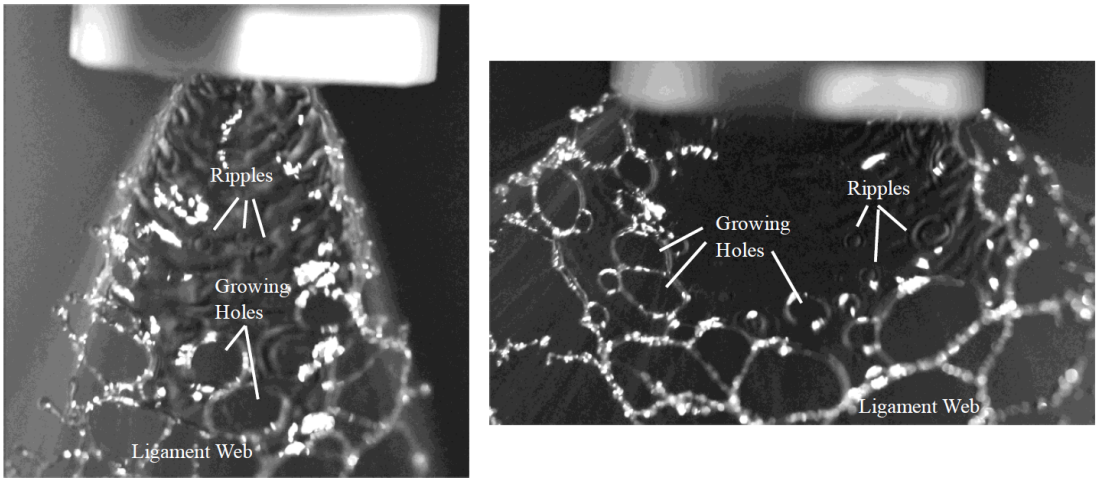

Figure 7.8: Oil-in-water emulsion spray, displaying hole breakup mechanism. 0.5 − 5 % Interlock in water sprayed through a Teejet a) 8002 and b) 110015 fan-type nozzle. Holes form and grow until they collide, forming ligaments which then breakup into droplets.

7.3.3 Data analysis and comparison with model

The data in this section were obtained using the Teejet 8002 nozzle. Figure 7.9 is a plot of pure water, sprayed at various pressures where the droplet volume-mean diameter (VMD) was measured via the light scattering Sympatec instrument. The x-axis is the Weber number. It should be noted that the only parameter in the Weber number that was varied was the spray speed.

An empirical power-law best-fit of the data to the right of the vertical, dashed line in Figure 7.9 indicates a Weber number dependence of mean droplet diameter of $We^{-0.34}$. Using all of the data for determining We dependence yielded a poor fit and therefore the data was empirically segregated into what appeared to be a natural break/transition. Referring to Fraser, et al.[30], the model predicts a We power dependence of $-1/3$. However, in the section on nozzle performance, k was

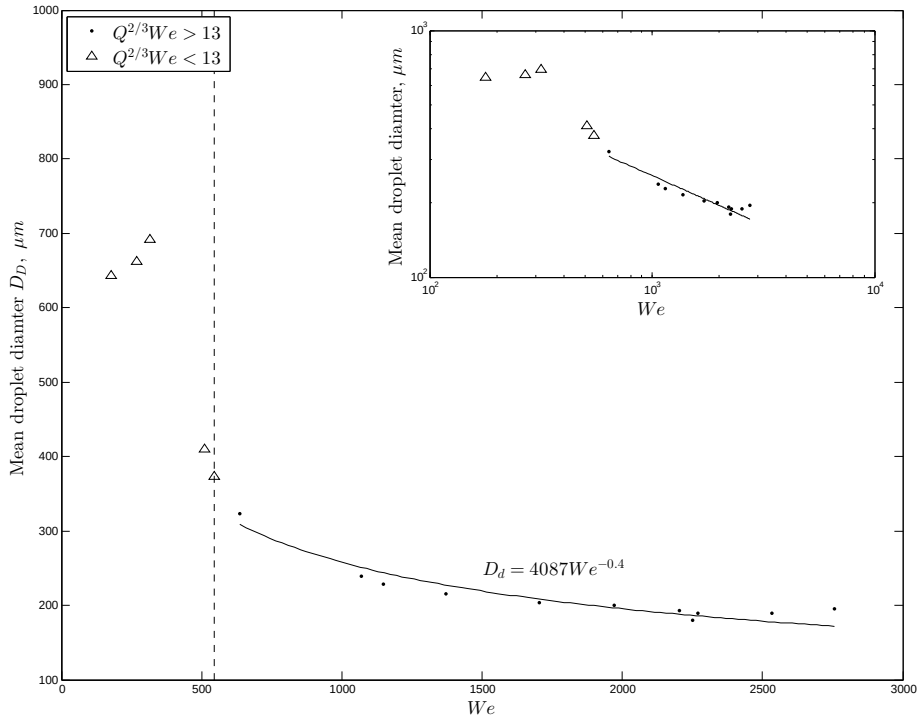

Figure 7.9: Average droplet size from single water sprays for various Weber number. Fraser power law agrees with high Weber number

found to be a function of $U^{-0.4}$, corresponding to a Weber number dependence of $\sim We^{-0.2}$. Inserting this dependence in the Fraser model yields a predicted power dependence of -0.4, which is in good agreement with the data as indicated by the solid line (power dependence of -0.34).

The vertical dashed line in Figure 7.9 is the theoretical threshold derived by Villermaux and Clanet (2002) for the transition between rim breakup (to the left of the line) or flapping motion (to the right of the line). It must be noted, however, that the experiments of Villermaux and Clanet were not on fan-type nozzles, but rather sheets generated by two impinging jets, but the theoretical line seems to be relevant to the fan-type data in Figure 7.9. Villermaux and Clanet clearly state that they

had no evidence of the Fraser model, and in fact, believed the actual mechanism to be a direct atomization of the sheet (without liquid ribbon detachment), owing to acceleration acting on the sheet front and the interfacial instability that results. In this work, the Fraser mechanism was primarily observed and experimental observations agree favorably with the Fraser model.

A power law fit to the data to the left of the theoretical line indicates a power dependence of $\sim We^{-0.54}$, notably different from the trend to the right of the line. However, this observation is dependent upon the five data points to the left of the dotted line. This transition line is thought to indicate the competition between two distinct mechanisms that is also supported by the image analysis, but there are too few data to reliably extract a power law for this regime. In addition, the power of -0.54 does not agree with the power predicted by Villermaux and Clanet for either the rim or flapping regime. This is not an indication that their analysis was incorrect, but rather that no definitive conclusions can be made about this regime other than it scales differently than the flapping mechanism.

Interlock-water emulsions were sprayed at concentrations ranging from $0.5\% - 5\%$ Interlock where the primary mechanism for breakup up is hole formation and web formation. The data are given in Figure 7.10. The hole-growth model proposed suggests an explicit Weber number power dependence of $-1/6$. Including the Weber number power dependence of -0.2 in k, the overall Weber dependence is expected to be $\sim$ 0.23. The simple proposed mode does a reasonable job for We of agricultural importance ($2000 < We < 4000$). This simple model fails at $We < 750$, indicating another stability mechanisms may be responsible for sheet breakup. The best-fit power law for We to the experimental data is 0.36.

One interesting, yet not fully understood feature of the data in Figure 7.10 is

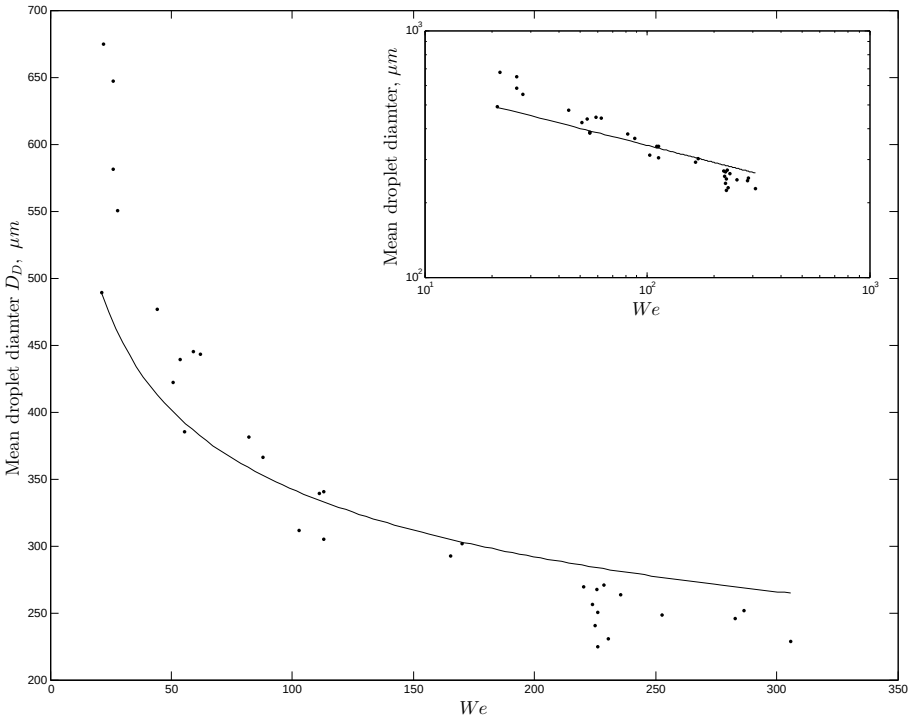

Figure 7.10: Average droplet size from two phase sprays for various Weber number. The power law from our proposed mechanism agrees with data.

that oil concentrations ranging from $0.5\% to 5\%$ in water all seem to fall nearly on the same curve. Though the model hasn't completely captured this, it does predict a weak dependence on the spacing of the holes of $z^{1/6}$. If every oil droplet contributed to a hole, increasing the concentration 20-fold is only expected to increase the droplet size by a factor of 1.64. While this is a small change in droplet size relative to concentration, it should still be detectable in the data. However, it is possible the spacing of the holes is not linearly related to the concentration of the oil, and the smaller size of the oil drops (in relation to the film thickness) may indicate that the starting 2-dimensional spatial location within the liquid sheet

needs to be addressed before any definitive impacts on number density of oil drops in the two phase system be addressed.

One other note is that the surface tension for the various concentrations was not measured. Instead, values from Qin et al. (2010) were used and assumed to be constant for all concentrations. This assumption may be justified, because it is believed that these concentrations are past the critical micelle concentration, thus the surface tension would remain relatively constant.

7.4 Discussion and conclusion

The stability and atomization of a liquid sheet is a subject that has been debated for decades and is still an active area of research. Of particular interest to the agricultural industry is the application of oil-in-water type emulsions, as many agricultural active chemicals are contained within an oil phase. It was known prior to this work that the presence of an oil phase caused earlier breakup of the sheet and produced larger droplets than the corresponding water spray at the same conditions. Three mechanisms of sheet breakup were observed in image analysis: one related to the flapping wave motion of the sheet, one related to disintegration at the rims of the sheet, and one related to hole growth and collision.

Flapping motion and wave growth has been discussed by many authors. The first complete model of sheet disintegration was constructed by Fraser et al. (1962), in which waves on the sheet grew until a liquid ligament detached and subsequently disintegrated into droplets. Though this model has received criticism by several

authors, it has been successfully applied by various researchers, and also in this study for single phase, water atomization. This mechanism was found to be dominant at pressures from 20-50 psig, corresponding to spray speeds of $17 - 26\ m/s$ and Weber numbers ranging from $1200 - 5500$.

Rim breakup is attributed to acceleration forces acting on the outer edges of the sheet. It is well known that acceleration can destabilize a fluid-fluid interface. The rim breakup mechanism was observed at pressures ranging from $5 - 20\ psig$, corresponding to spray speeds of $8 - 17\ m/s$ and Weber numbers ranging from $350 - 1200$. The droplet size data did not agree with literature predictions for this mechanism, but suggests a different Weber number dependence than in the higher pressure regime.

The appearance of holes has been observed previously, particularly in the presence of an oily phase, entrained air, and in the absence of a surrounding gas. In this study, holes were always observed when an emulsion was sprayed, indicating that this mechanism is dominant over the others. Disturbances were observed to manifest as ripples, which turn into rapidly expanding holes. Upon collision, holes form a network of cylinder-like ligaments, which then break down into droplets. A simple model which constructed, extending an existing, single hole growth model, which gave good agreement with the data.

The mechanism of hole formation is not yet fully understood. Cloeter, et al. (2010) speculated that deformation of the oil phase inside of the nozzle and the subsequent retraction of the particles upon leaving the nozzle disrupted the sheet. They support this hypothesis with experiments in which solid particles were sus-

pended in water and no change was observed from pure water [19]. Dombrowski and Fraser (1954) also observed similar behavior; however holes appeared when sulfur particles were suspended, indicating the hydrophobic nature of the solid particles may be the appropriate mechanism for hole formation.

Whether the kinematics of a deforming oil particle could create a sufficient disturbance to puncture the sheet is not established. It may be consistent with the ripples which were observed in images of emulsion spraying. Hadji and Schreiber (2007) performed a numerical simulation of 3-dimensional sheets. By introducing an array of peaks as a disturbance, they produced ripple like features which then transitioned to a higher energy state, indicating instability.

Another possible explanation of the origin of the holes is the transition of the emulsion to a more stable, phase-separated state. A slightly buoyant oil particle, as it penetrates the air/water interface, creates an initial force imbalance (at the contact line for an oil-water-air system) leading to the oil droplet spreading on the surface of the water. The spreading could displace water, creating the ripple like effect which seems to be a precursor to hole formation. This contact line behavior is consistent with Dombrowski and Fraser's (1954) observation of holes in the presence of hydrophobic, insoluble sulfur particles.

A simple test of whether contact line motion could be responsible for hole formation would be to suspend buoyant, hydrophobic solid particles to the suspension. Though this wouldnt mimic the case of the oil spreading, it would illustrate if contact line force imbalances have any effect on the sheet stability when the 2nd phase penetrates the interface with the bulk fluid (continuous phase) and air.

7.5 Acknowledgements

The authors thank Anup Sane for his expertise and aid in taking photographs of the spray. We are grateful to Kuide Qin and Steve Wilson for their advice and insight into the behavior of agricultural sprays, and to Morgan Rosemeyer and Brandon Downer for assisting in the use of the spray equipment. Dr. Kuide Qin and Zhexuan Zhang provided critical reviews of this manuscript.

CHAPTER 8

APPENDIX: SUMMARY OF CASTING DATA

Summary of abbreviations:

BN: boron nitride heat-transfer interruptions introduced

IR: infrared camera used

MG alloy: an alloy provided by Metglas

Insert: modified nozzle insert used

Low/High grit: wheel polished with sandpaper grit lower/higher than 150 grit

Air BL: attempted to disrupt air flow near the nozzle

Summary of Cast ID's

AKSU13: Alexander-Keim, Summer 2013

CPSU13: Cesaro-Pollack, Summer 2013

CASP12: Carroll-Altieri, Spring 2012

AASU12: Alexander-Altieri, Summer 2012

AKSU12: Alexander-Keim, Summer 2012

ACSP11: Altieri-Carroll, Spring 2011

CASP11: Carroll-Altieri, Spring 2011

AASU11: Alexander-Altieri, Summer 2011

AKSU11: Alexander-Krause, Summer 2011

KASU11: Krause-Altieri, Summer 2011

Table A1: Table of experimental data for PFMS
in Olin Hall 101 since Summer 2011

Cast ID	$Mass$ (kg)	G (mm)	U (m/s)	τ (mm)	PI	We	
$AKSU$13_01	355	0.04	300	0.102	4.39	125.9	
$CPSU$13_01	346	0.04	300	0.131	1.45	126.7	
$CPSU$13_02	399	0.04	300	0.133	1.42	125.7	
$CPSU$13_03	398	0.04	300	0.142	1.4	124.6	
$CPSU$13_04	400	0.04	300	0.097	1.47	127	
$CPSU$13_05	357	0.04	300	0.133	1.41	124.7	
$CPSU$13_06	432	0.04	300	0.088		126.8	BN
$CPSU$13_07	356	0.04	300	0.093		126.3	BN
$CPSU$13_08	377	0.04	300	0.117		125.5	BN
$CPSU$13_09	399	0.04	300	0.156	1.38	126.4	BN
$CPSU$13_10	398	0.04	300	0.111	1.42	127.2	BN
$CPSU$13_11	462	0.04	300	0.098	1.43	128.5	BN
$CPSU$13_12	395	0.04	300	0.117	1.35	127.3	Foil stripe
$CPSU$13_13	417	0.04	300	0.118	1.38	126.6	Foil stripe
$CPSU$13_14	452	0.075	250	0.175	2.67	163.3	Foil stripe
$CPSU$13_15	472	0.04	300	0.082			BN
$CPSU$13_16	472	0.04	300	0.129	1.37	127.1	Heater test
$CPSU$13_17	443	0.04	300	0.126	1.41	126	BN
$CPSU$13_18	380	0.04	300	0.121	1.31	128.6	
$CPSU$13_19	487		300	0.111			
$CPSU$13_20							
$CPSU$13_21	491	0.04	300	0.101	1.38	126.9	IR
$CPSU$13_22	385	0.04	300	0.094	1.34	127.4	IR
$CPSU$13_23	467	0.04	300	0.124	1.37	128.1	IR

Continued on next page.

Table A1: Table of experimental data for PFMS
in Olin Hall 101 since Summer 2011

Cast ID	$Mass$ (kg)	G (mm)	U (m/s)	τ (mm)	PI	We	
$CASP$12_01	501	0.04	300	0			
$AASU$12_01	812	0.04	300	0.091	1.72	126.3	
$AASU$12_02	500	0.04	350	0.165		172.7	MG Alloy
$AKSU$12_01	412	0.04	300	0.119		126.4	
$AKSU$12_02	376	0.04	300	0.074		126.9	
$AKSU$12_03	396	0.04	300	0.088			
$AKSU$12_04	398	0.04	300	0.076			
$AKSU$12_05	406	0.04	300	0.071	4.43	126.7	Wire
$AKSU$12_06	358	0.04	300	0.072		126.8	Wire
$AKSU$12_07	328	0.04	300	0.101	1.33	126.6	
$AKSU$12_08	352	0.04	300	0.121	1.34	126.6	
$AKSU$12_09	378	0.075	300	0.16	2.46	238	Wire
$AKSU$12_10	381	0.04	300	0.125	1.36	126.5	Wire
$AKSU$12_11	312	0.04	300	0.089	1.36	126.6	Wire
$AKSU$12_12	311	0.04	300	0.092	1.37	126.7	Wire
$AKSU$12_13	414	0.04	300	0.092	1.41	126.1	Wire
$AKSU$12_14	367	0.04	300	0.097	1.37	126.4	Wire
$AKSU$12_15	400	0.075	300	0.188	3.05	237.9	Wire
$AKSU$12_16	404	0.075	300	0.152	2.53	237	Wire
$AKSU$12_17	416	0.075	300	0.169	8.25	236.7	Wire
$AKSU$12_18	374	0.03	300	0.075	0.852	94.96	Small gap
$AKSU$12_19	313	0.01	250	0.054	0.285	22.12	
$AKSU$12_20	274	0.075	250	0.145	2.2	165	
$AKSU$12_21	455	0.04	250	0.115	1.31	87.89	Wire
$AKSU$12_22	335	0.04	220	0.189	1.38	66.17	Wire
$AKSU$12_23	327	0.025	250	0.107	1.2	54.83	CW cast
$AKSU$12_24	352	0.04	300	0.133	1.35	126.6	Wire
$AKSU$12_25	384	0.075	250	0.202	2.47	165.2	CW cast
$AKSU$12_26	409	0.075	250	0.154	2.32	162.2	Wire
$AKSU$12_27	381	0.075	250	0.158	2.34	164.7	
$AKSU$12_28	473	0.075	220	0.283			
$AKSU$12_29	396	0.075	220	0.197	2.34	127.6	Wire
$AKSU$12_30	353	0.075	250	0.18	2.31	164.1	Wire
$AKSU$12_32	414	0.075	200	0.193	2.39	105.2	Wire
$AKSU$12_33	334	0.04	200	0.154	1.25	55.95	Wire
$AKSU$12_34	448	0.075	250	0.234		165.5	CW cast
$AKSU$12_35	374	0.075	250	0.179	2.5	164.1	Wire
$AKSU$12_36	375	0.075	250	0.164	2.32	164.3	Insert
$AKSU$12_37	400	0.075	250	0.168	2.36	165	Wire

Continued on next page.

Table A1: Table of experimental data for PFMS
in Olin Hall 101 since Summer 2011

Cast ID	$Mass$ (kg)	G (mm)	U (m/s)	τ (mm)	PI	We	
$ACSP11\_01$	871	0.03	150	0.186	1.23	23.39	Sticking
$CASP11\_01$	948	0.03	150	0.21	1.16	23.65	Sticking
$CASP11\_02$	1033	0.03	150	0.171	1.26	23.66	Sticking
$CASP11\_03$	877	0.02	250	0			Sticking
$CASP11\_04$	888	0.1	250	0.139		218.4	Sticking
$CASP11\_05$	868	0.1	300	0.178	4.24	315.8	Sticking
$CASP11\_06$	1017	0.1	300	0.164		316.8	Sticking
$CASP11\_07$	964	0.1	325	0.18	4.39	371.2	Sticking
$CASP11\_08$	1593	0.1	325	0.155	5.84	368.3	Sticking
$CASP11\_09$	660	0.04	300	0.089	1.46	127.3	
$CASP11\_10$	728	0.04	300	0.123	1.61	127.6	
$AASU11\_01$	807	0.04	300	0.128	1.58	98.54	
$AASU11\_02$	415	0.04	250	0.131	1.26	87.56	
$AASU11\_03$	436	0.04	300	0.098	1.19	126.5	High grit
$AASU11\_04$	797	0.04	300	0			Low grit
$AASU11\_05$	797	0.04	300	0.111	1.49	127.2	High grit
$AASU11\_06$	479	0.04	300	0.077	1.1	126.4	
$AASU11\_07$	454	0.04	300	0.131	1.27	126.4	Axial sanding
$AASU11\_08$	830	0.04	300	0.134	1.4	126.2	Insert
$AASU11\_09$	846	0.04	300	0.137	1.35	126.2	Insert
$AASU11\_10$	735	0.04	300	0.131	1.29	125.5	Insert
$AASU11\_11$	844	0.04	300	0.116	1.37	126.6	Insert
$AASU11\_12$	872	0.075	300	0.123	2.37	236	Insert
$AASU11\_13$	424	0.04	300	0.054	1.19	127.1	Insert
$AASU11\_14$	436	0.04	300	0.076	1.15	126.5	Insert
$ACSU11\_01$	442	0.04	300	0.124	1.3	126.7	
$AKSU11\_02$	807	0.04	300	0.09	1.62	126.1	
$AKSU11\_03$	731	0.04	300	0.114	3.82	122.6	
$AKSU11\_04$	812	0.04	300	0.107			
$AKSU11\_05$	793	0.04	300	0.111	1.52	125.6	
$AKSU11\_06$	716	0.04	300	0.121	1.43	125.8	
$AKSU11\_07$	631	0.04	300	0.069	1.47	124.7	Low grit
$AKSU11\_08$	712	0.04	300	0.07	1.5	127.3	High grit
$AKSU11\_09$	893	0.04	300	0.059	1.61	126.2	Insert

Continued on next page.

Table A1: Table of experimental data for PFMS
in Olin Hall 101 since Summer 2011

Cast ID	$Mass$ (kg)	G (mm)	U (m/s)	τ (mm)	PI	We	
$AKSU11\_10$	369	0.075	300	0.118	2.07	236.7	Insert
$AKSU11\_11$	435	0.04	220	0.11	1.1	68.26	Insert
$AKSU11\_12$	414	0.04	300	0.076	1.38	126.9	Insert
$AKSU11\_13$	428	0.04	300	0.078	1.1	126.9	BN
$AKSU11\_14$	431	0.04	250	0.113	1.18	87.73	BN
$AKSU11\_15$	416	0.04	280	0.096	1.16	109.8	BN
$AKSU11\_16$	419	0.04	325	0.08	1.25	148.5	BN
$AKSU11\_17$	400	0.04	300	0.075		126.7	BN
$AKSU11\_18$	409	0.04	300	0.078		126.7	BN
$AKSU11\_19$	396	0.04	325	0.068		149.1	BN
$AKSU11\_20$	424	0.075	300	0.126		238.4	BN
$AKSU11\_21$	398	0.04	300	0.069		126.4	BN
$AKSU11\_22$	428	0.04	300	0.06		126.6	Air BL
$AKSU11\_23$	414	0.04	300	0.056	4.43	123.1	Air BL
$AKSU11\_24$	408	0.04	300	0.094	4.43	126.5	Air BL
$AKSU11\_25$	416	0.04	300	0.073	4.43	126.6	Air BL
$AKSU11\_26$	392	0.04	250	0.113	4.42	87.6	Air BL
$AKSU11\_27$	412	0.075	300	0.124	8.31		Air BL
$AKSU11\_28$	412	0.078	300	0.122		237.2	Air BL
$AKSU11\_29$	427	0.075	300	0.179		236.6	Large gap
$AKSU11\_30$	417	0.075	300	0.164		235.7	Large gap
$AKSU11\_31$	621	0.075	300	0.137		236.8	Air BL
$AKSU11\_32$	700	0.075	300	0.153		236.3	
$AKSU11\_33$	410	0.04	300	0.107		126.5	
$AKSU11\_34$	632	0.1	300	0.137		315.1	Air BL
$KASU11\_01$	757	0.04	300	0.063	1.6	127	
$KASU11\_02$	416	0.04	300	0.07		126.2	
$KASU11\_03$	413	0.04	300	0.104	4.41	128	Air BL
$KASU11\_04$	430	0.04	300	0.071		133.2	Air BL
$KASU11\_05$	392	0.04	300	0.09		126.6	Air BL
$KASU11\_06$	417	0.04	300	0.089	4.41	128.9	Air BL
$KASU11\_07$	702	0.04	350	0.117		171.5	High We

BIBLIOGRAPHY

[1] Nathaniel S Barlow, Brian T Helenbrook, SP Lin, and Steven J Weinstein. An interpretation of absolutely and convectively unstable waves using series solutions. *Wave Motion*, 47(8):564–582, 2010.

[2] NS Barlow, BT Helenbrook, and SP Lin. Transience to instability in a liquid sheet. *Journal of Fluid Mechanics*, 666:358–390, 2011.

[3] AB Bichi, WR Smith, and JG Wissink. Solidification and downstream meniscus prediction in the planar-flow spin casting process. *Chemical Engineering Science*, 63(3):685–695, 2008.

[4] JB Bostwick and PH Steen. Capillary oscillations of a constrained liquid drop. *Physics of Fluids*, 21:032108, 2009.

[5] Joshua Bostwick. *Stability of constrained capillary interfaces*. Ph.D Thesis Cornell University, 2011.

[6] D.J. Branagan, B.E. Meacham, and A.V. Sergueeva. US Patent 20120263621 A1: Ductile Metallic Glasses in Ribbon Form. *US Patent 20120263621 A1*, 2012.

[7] D.J. Branagan, B.E. Meacham, and A.V. Sergueeva. US Patent 8317949 B2: Ductile metallic glasses. *US Patent 8317949 B2*, 2012.

[8] Richard J Briggs. *Electron-stream interaction with plasmas*, volume 121. MIT press Cambridge, MA, 1964.

[9] DR Brown. A study of the behaviour of a thin sheet of moving liquid. *J. Fluid Mech*, 10:297, 1961.

[10] M. Bussmann, J. Mostaghimi, DW Kirk, and JW Graydon. A numerical study of steady flow and temperature fields within a melt spinning puddle. *International journal of heat and mass transfer*, 45(19):3997–4010, 2002.

[11] C.J. Byrne, A.M. Kueck, S.P. Baker, and P.H. Steen. In situ manipulation of cooling rates during planar-flow melt spinning processing. *Materials Science and Engineering: A*, 459(1):172–181, 2007.

[12] C.J. Byrne, E.A. Theisen, P.H. Steen, and B.L. Reed. Capillary puddle vibrations linked to casting-defect formation in planar-flow melt spinning. *Metallurgical and Materials Transactions B*, 37(3):445–456, 2006.

[13] C.J. Byrne, S.J. Weinstein, and P.H. Steen. Capillary stability limits for liquid metal in melt spinning. *Chemical engineering science*, 61(24):8004–8009, 2006.

[14] JK Carpenter and P.H. Steen. On the heat transfer to the wheel in planar-flow melt spinning. *Metallurgical and Materials Transactions B*, 21(2):279–283, 1990.

[15] J.K. Carpenter and P.H. Steen. Heat transfer and solidification in planar-flow melt-spinning: high wheelspeeds. *International Journal of Heat and Mass Transfer*, 40(9):1993 – 2007, 1997.

[16] Horatio Scott Carslaw and John Conrad Jaeger. Conduction of heat in solids. *Oxford: Clarendon Press, 1959, 2nd ed.*, 1:112, 132, 1959.

[17] Christophe Clanet and Emmanuel Villermaux. Life of a smooth liquid sheet. *Journal of fluid mechanics*, 462(1):307–340, 2002.

[18] CJ Clark and N Dombrowski. Aerodynamic instability and disintegration of inviscid liquid sheets. *Proceedings of the Royal Society of London. A. Mathematical and Physical Sciences*, 329(1579):467–478, 1972.

[19] Michael D Cloeter, Kuide Qin, Pramod Patil, Billy Smith, and LLC Dow AgroSciences. Planar laser induced fluorescence (plif) flow visualization applied to agricultural spray nozzles with sheet disintegration; influence of an oil-in-water emulsion. In *ILASS-Americas 22nd Annual Conf. on Liquid Atomization and Spray Systems. Cincinnati, USA*, 2010.

[20] BL Cox and PH Steen. herringbonedefect formation in planar-flow melt spinning. *Journal of Materials Processing Technology*, 2013.

[21] Brenton Cox. *Planar-flow melt spinning: process dynamics and defect formation.* Ph.D Thesis Cornell University, 2011.

[22] P. Cremer and J. Bigot. An infrared thermography study of the temperature variation of an amorphous ribbon during production by planar flow casting. *Materials Science and Engineering*, 98(0):95 – 97, 1988.

[23] FEC Culick. Comments on a ruptured soap film. *Journal of Applied Physics*, 31(6):1128–1129, 1960.

[24] S.H. Davis. Moving contact lines and rivulet instabilities. part 1. the static rivulet. *J. Fluid Mech*, 98(part 2):225–242, 1980.

[25] Luigi De Luca and Michela Costa. Instability of a spatially developing liquid sheet. *Journal of Fluid Mechanics*, 331:127–144, 1997.

[26] N Dombrowski and PC Hooper. A study of the sprays formed by impinging jets in laminar and turbulent flow. *J. Fluid Mech*, 18(3):392–400, 1963.

[27] N_ Dombrowski and WR Johns. The aerodynamic instability and disintegration of viscous liquid sheets. *Chemical Engineering Science*, 18(3):203–214, 1963.

[28] Norman Dombrowski and RP Fraser. A photographic investigation into the disintegration of liquid sheets. *Philosophical Transactions of the Royal Society of London. Series A, Mathematical and Physical Sciences*, pages 101–130, 1954.

[29] RG Dorman. The atomization of liquid in a flat spray. *British journal of applied physics*, 3(6):189, 1952.

[30] RP Fraser, Paul Eisenklam, Norman Dombrowski, and David Hasson. Drop formation from rapidly moving liquid sheets. *AIChE Journal*, 8(5):672–680, 1962.

[31] M Gaster. Growth of disturbances in both space and time. *Physics of Fluids*, 11:723, 1968.

[32] A.A. Griffith. The phenomena of rupture and flow in solids. *Philosophical transactions of the royal society of london. Series A, containing papers of a mathematical or physical character*, 221:163–198, 1921.

[33] Layachi Hadji and Willard C Schreiber. On the evolution of two-dimensional patterns in an inviscid liquid sheet. *Applied mathematical modelling*, 31(10):2266–2285, 2007.

[34] WW Hagerty and JF Shea. A study of the stability of plane fluid sheets. *J. Appl. Mech*, 22(4):509–514, 1955.

[35] G Hahn and A Schönecker. New crystalline silicon ribbon materials for photovoltaics. *Journal of Physics: Condensed Matter*, 16(50):R1615, 2004.

[36] R. Hasegawa. Present status of amorphous soft magnetic alloys. *Journal of magnetism and magnetic materials*, 215:240–245, 2000.

[37] R. Hasegawa and D. Azuma. Impacts of amorphous metal-based transformers on energy efficiency and environment. *Journal of Magnetism and Magnetic Materials*, 320(20):2451–2456, 2008.

[38] G. Herzer. Magnetic materials for electronic article surveillance. *Journal of magnetism and magnetic materials*, 254:598–602, 2003.

[39] $http://www.reynoldskitchens.com/media/171190/hd\_wrap\_faq.pdf$.

[40] Shyh-Chin Huang. The effect of melt delivery conditions on the casting of amorphous metal ribbons. pages 65–68, 1981.

[41] Tetsuharu Ibaraki. *Planar-flow melt spinning: experimental investigation on solidification, dynamics of the liquid puddle and process operability*. Cornell University, January, 1996.

[42] Seyed A Jazayeri and Xianguo Li. Nonlinear instability of plane liquid sheets. *Journal of Fluid Mechanics*, 406(1):281–308, 2000.

[43] C. Karcher and PH Steen. High-reynolds-number flow in a narrow gap driven by solidification. i. theory. *Physics of Fluids*, 13(4):826–833, 2001.

[44] C. Karcher and PH Steen. High-reynolds-number flow in a narrow gap driven by solidification. ii. planar-flow casting application. *Physics of Fluids*, 13(4):834–840, 2001.

[45] B Karpe, B Kosec, T Kolenko, and M Bizjak. Heat transfer analyses of continuous casting by free jet meltspinning device. *Metalurgija*, 50(1):13–16, 2011.

[46] S Kavesh. Principles of fabrication(of metallic glasses). *Metallic Glasses. ASM, Metals Park, Ohio. 1978, 36-73*, 1978.

[47] K. Kendall. Thin-film peeling-the elastic term. *Journal of Physics D: Applied Physics*, 8(13):1449, 1975.

[48] J. Kukura, K. Ford, A. Singh, P.H. Steen, and T. Ibaraki. Measurement of heat transfer coefficient in planar flow casting. *Simulations of Materials Processing: Theory, Methods and Applications*, pages 1153–1157, 1995.

[49] Adrienne S Lavine, FP Incropera, and DP DeWitt. Fundamentals of heat and mass transfer. pages 8,256–261, 2006.

[50] Deren Li, Jianhong Zhuang, Tiancheng Liu, Zhichao Lu, and Shaoxiong Zhou. The pressure loss and ribbon thickness prediction in gap controlled planar-flow casting process. *Journal of Materials Processing Technology*, 211(11):1764 – 1767, 2011.

[51] HH Liebermann. Ribbon-substrate adhesion dynamics in chill block melt-spinning processes. *Metall. Trans. B*, 15B:155–161, 1984.

[52] SP Lin, ZW Lian, and BJ Creighton. Absolute and convective instability of a liquid sheet. *J. Fluid Mech*, 220:673–689, 1990.

[53] Sung P Lin and ZL Wang. Three types of linear theories for atomizing liquids. *Atomization and Sprays*, 18(3), 2008.

[54] Heping Liu, Wenzhi Chen, Shengtao Qiu, and Guodong Liu. Numerical simulation of initial development of fluid flow and heat transfer in planar flow casting process. *Metallurgical and Materials Transactions B*, 40(3):411–429, 2009.

[55] Paolo Luchini. Is a plane liquid curtain algebraically absolutely unstable? *Physics of Fluids*, 16:2154, 2004.

[56] R.E. Maringer. Solidification on a substrate. *Mat. Sci. Eng.*, 98:13–20, 1988.

[57] Inc. Metglas. http://www.metglas.com. Accessed on 10/10/2013.

[58] A.D. Myshkis, V.G. Babskii, N.D. Kopachevskii, L.A. Slobozhanin, AD Tyuptsov, and RS Wadhwa. *Low-gravity fluid mechanics*. Chapters 5 and 6, 1987.

[59] M.C. Narasimhan. Continuous casting method for metallic strips. 1979. US Patent 4,142,571.

[60] El-Sayed R Negeed, S Hidaka, M Kohno, and Y Takata. Experimental and

analytical investigation of liquid sheet breakup characteristics. *International Journal of Heat and Fluid Flow*, 32(1):95–106, 2011.

[61] BNJ Persson and E Tosatti. The effect of surface roughness on the adhesion of elastic solids. *Journal of Chemical Physics*, 115:5597–5610, 2001.

[62] T.J. Praisner, J.S.J. Chen, and A.A. Tseng. An experimental study of process behavior in planar flow melt spinning. *Metallurgical and Materials Transactions B*, 26(1):1199–1208, 1995.

[63] Andrea Prosperetti. Linear oscillations of constrained drops, bubbles, and plane liquid surfaces. *Physics of fluids*, 24:032109, 2012.

[64] L. Rayleigh. On the capillary phenomena of jets. *Proceedings of the Royal Society of London*, 29(196-199):71–97, 1879.

[65] B.L. Reed, A.H. Hirsa, and P.H. Steen. Vorticity transport in solidification boundary layers. *Journal of Fluid Mechanics*, 426:397–406, 2001.

[66] H. Sakamoto, T. Yamada, N. Okumura, and T. Sato. Improvement in brittleness of amorphous Fe-Si-B-C alloy ribbons by controlling casting conditions. *Materials Science and Engineering: A*, 206(1):150 – 153, 1996.

[67] Félix Savart. Mémoire sur la constitution des veines liquides lancées par des orifices circulaires en mince paroi. *Ann. Chim. Phys*, 53(337):1833, 1833.

[68] HB Squire. Investigation of the instability of a moving liquid film. *British Journal of Applied Physics*, 4(6):167, 1953.

[69] P.H. Steen and C. Karcher. Fluid mechanics of spin casting of metals. *Annual review of fluid mechanics*, 29(1):373–397, 1997.

[70] M Strani and F Sabetta. Free vibrations of a drop in partial contact with a solid support. *Journal of Fluid Mechanics*, 141:233–247, 1984.

[71] Peter Andrew Sturrock. Kinematics of growing waves. *Physical Review*, 112(5):1488, 1958.

[72] B.G. Sundararajanand, A. Thomas. Heat transfer during melt spinning of al-7% si alloy on a cu-be wheel. *Light Metals*, pages 793–810, 2008.

[73] K. Takeshita and P.H. Shingu. An analysis of the heat transfer problem with phase transformation during rapid quenching. *Trans. Jap. Inst. Met*, 24:293–296, 1983.

[74] K. Takeshita and P.H. Shingu. An analysis of the ribbon formation process by the single roller rapid solidification technique. *Trans. Jpn. Inst. Met.*, 24(7):529–536, 1983.

[75] K. Takeshita and P.H. Shingu. Thermal contact during the cooling by the single roller chill block casting. *Japan Institute of Metals, Transactions*, 27:454–462, 1986.

[76] E.A. Theisen, M.J. Davis, S.J. Weinstein, and P.H. Steen. Transient behavior of the planar-flow melt spinning process. *Chemical Engineering Science*, 65(10):3249 – 3259, 2010.

[77] VI Tkatch, SN Denisenko, and ON Beloshov. Direct measurements of the cooling rates in the single roller rapid solidification technique. *Acta Materialia*, 45(7):2821–2826, 1997.

[78] VI Tkatch, AM Grishin, and VV Maksimov. Estimation of the heat transfer coefficient in melt spinning process. In *Journal of Physics: Conference Series*, volume 144, page 012104. IOP Publishing, 2009.

[79] V.I. Tkatch, A.I. Limanovskii, S.N. Denisenko, and S.G. Rassolov. The effect of the melt-spinning processing parameters on the rate of cooling. *Materials Science and Engineering: A*, 323(1):91–96, 2002.

[80] Eric Vandre. *Onset of Dynamic Wetting Failure: The Mechanics of High-speed Fluid Displacement*. Ph.D Thesis University of Minnesota, 2013.

[81] Emmanuel Villermaux and Christophe Clanet. Life of a flapping liquid sheet. *Journal of fluid mechanics*, 462:341–363, 2002.

[82] G.X. Wang and EF Matthys. Modelling of rapid solidification by melt spinning: effect of heat transfer in the cooling substrate. *Materials Science and Engineering: A*, 136:85–97, 1991.